ACTA UNIVERSITATIS CAROLINAE

European Journal of Environmental Sciences

VOLUME 15 / NUMBER 1
2025

CHARLES UNIVERSITY
KAROLINUM PRESS

ISSN 1805-0174 (Print)
ISSN 2336-1964 (Online)

CONTENTS

Jan Frouz, and Jakub Borovec: Physical and chemical properties of the sediment in natural and artificial river bars in the Elbe 5

Iva Hůnová, and Suruchi: Potential of satellite imagery for studying the spatial distribution of fog and its role in atmospheric deposition 12

Liudmyla Yashchenko, Oleksandr Androshchuk, Liudmyla Vasylenko, and Yuliya Chornoivan: Environmental risks of heavy metal pollution in war-affected soils in Ukraine 18

Peter Chanas, and Jan Frouz: Sunning clusters of ants contribute significantly, but weakly to spring heating in the nests of the red wood ants, *Formica polyctena* 28

Karolina Walzelova, Simon Walzel, and Jan Hovorka: Simultaneous mobile PM_{10} monitoring provides high definition spatial and time localization of hotspots of poor air quality in an urban environment 34

Kristýna Hebenstreitová, Lenka Vaňková, and Daniel Vaněk: Determination of the suitability of agilent bioanalyzer 2100 for investigations into wildlife crimes: case studies 43

PHYSICAL AND CHEMICAL PROPERTIES OF THE SEDIMENT IN NATURAL AND ARTIFICIAL RIVER BARS IN THE ELBE

JAN FROUZ[1,*] AND JAKUB BOROVEC[1]

[1] Biology Centre of the Czech Academy of Sciences, Institute of Soil Biology and Biogeochemistry, Na Sádkách 7, 370 05 Ceske Budejovice, Czech Republic
* Corresponding author: frouz@natur.cuni.cz

ABSTRACT

Physical and chemical properties of natural river bars in the lower reaches of Elbe in the Czech Republic were studied and compared with those of artificial river bars. Most of the chemical properties of the sediment are not correlated with the texture of the sediment but are affected by the organic matter content. The highest content and most of the chemicals were recorded in the central parts of a bar and close to the shore and terrestrial habitats. Artificial bars significantly differ from natural ones in their chemical properties. There were higher levels of phosphorus and other nutrients in artificial bars.

Keywords: Elbe; chemistry; habitat; river bars; texture

Introduction

River bars are habitats formed by the accumulation of sediments in a part of a river when the sediment supply exceeds the transport capacity. River bars are shaped by a continuous deposition and erosion of sediments. This results in a very dynamic environment with frequent disturbances, which harbours a very specific biota (Bendix and Stella 2013). This is particularly true of river bars in the lower reaches of the Elbe in the Czech Republic (Juřiček 2013; Bejček and Volfová 2019; Havlíček et al. 2023). Although the flora and fauna on these bars has been intensively studied, especially in terms of indicative umbrella species, such as *Corrigiola litoralis* (Juřiček 2013; Bejček and Volfová 2019; Havlíček et al. 2023), little is known about the nutrient distribution in these habitats and whether it is major driving factor. Understanding these patterns is essential for more effective protection of river bars or even for targeted intervention aimed at restoring bar habitats. Bar restoration is a complex process that must consider many hydrological and ecological aspects (Eekhout et al. 2013; González et al. 2015; Li et al. 2023), of which differences in the nutrient dynamics of natural and artificial river bars are among the least studied.

In this study, the nutrient distribution in relation to the distribution of organic matter and sediment texture in natural river bars is compared with that in artificial bars mainly in terms of the level of nutrients and other key elements.

Material and Methods

Study sites and sampling design

This study was carried out on periodically flooded gravel river bars in the Elbe River between Ústí nad Labem and the Czech-German border (Fig. 1). The appearance of gravel bars above water depends on the flow of water, with the largest area exposed occurring in summer. However, in wet years gravel bars can remain underwater all year round. In addition, fluctuations in river level during a year are significantly influenced by the dams

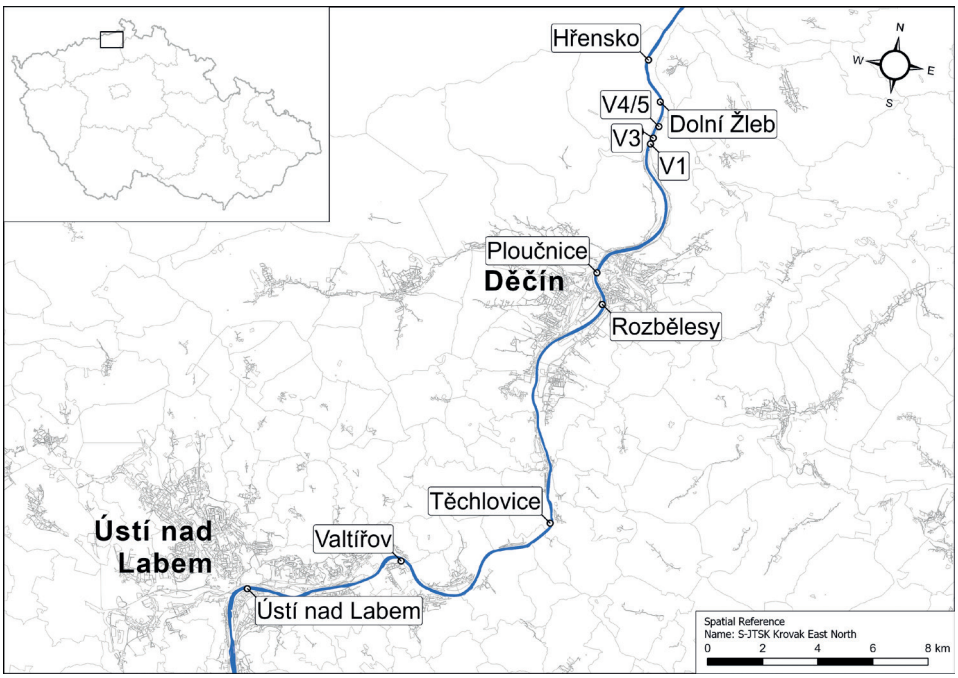

Fig. 1 Maps showing the locations of the sites studied on the Elbe between Ústí nad Labem and the Czech-Germany border. Artificial bars are indicated by the letter V. Map based on orthophoto ČÚZK 2019.

Frouz, J., Borovec, J.: Physical and chemical properties of the sediment in natural and artificial river bars in the Elbe
European Journal of Environmental Sciences, Vol. 15, No. 1, pp. 5–11
https://doi.org/10.14712/23361964.2025.1

Table 1 Location and details of the sites studied, with those selected for more detailed study marked with an asterix *.

Site	Type	Width (m)	Length (m)	Slope	Latitude (N)	Longitude (E)
Valtířov*	natural – ruderal plants	22	280	steep	50.676	14.127
Ploučnice	natural – ruderal plants	10	40	moderate	50.778	14.206
Hřensko*	natural – typical	19	400	moderate	50.849	14.217
Dolní Žleb*	natural – typical	16	450	moderate	50.836	14.226
Rozběsy	natural	17	220	moderate	50.768	14.211
Těchlovice*	natural	8	200	moderate	50.695	14.200
Ústí nad Labem	natural – ruderal plants	12	50	moderate	50.660	14.051
V4/5	artificial	24	240	moderate	50.828	14.227
V3	artificial	28	100	uneven	50.824	14.225
V1	artificial	6	60	uneven	50.822	14.224

on the Vltava River and the Střekov weir. It follows a natural seasonal pattern, but the maximum discharge during floods used to be higher and summer minimums during dry periods were lower, when there were no dams. Also, the river ceased to freeze over in winter and early spring after the reservoirs were built.

To characterize the differences in grain size and distribution, and chemical composition of the deposited material, seven sites with the largest and best developed gravel bars and three artificial sites designed to provide an alternative habitat for riparian vegetation were selected (Table 1).

Sediments were sampled next to the 60 permanent 1 × 1 m plots that were arranged in transects across and parallel to the river; the five largest localities had nine plots (i.e. three parallel and three across) and five smaller localities had three plots (i.e. one across in the central part of the locality). Parallel transects were used to determine differences in the composition of deposited material at the front, middle and rear of gravel bars that reflect the typical decrease in flow velocity of the river (Fig. 2). Each transect across a bar started at the point determined by when the water recorded at the water level gauge in Děčín was 150 cm and ended in front of where the terrestrial vegetation started (Fig. 2).

Texture and chemistry of the sediment in the river bars

Texture of the top 5 cm of the substrate collected from a 20 × 20 cm area near the 1 × 1 m permanent plots was measured. The weight of the fresh sample and the sample after drying at 60 °C were used to calculate the water content. Texture was analysed using the whole dry sample, when fractions >200 mm, 200–50 mm, and 50–20 mm were separated manually; fractions 20–5 mm, 5–2 mm, 2–0.5 mm by dry sieving and the particles below 0.5 mm were analysed in the suspension using MasterSizer 2000 MU (Malvern Instruments, England). The finest fraction of particles below 0.5 mm was used for loss on ignition (550 °C for 2 hrs.) and all other chemical analyses.

For the determination of plant-accessible nutrients and selected metals (P, K, Ca, Mg, Fe, Mn, Al, Cr, As), Mehlich III extraction solution (Mehlich 1984) was used, where 1 g of sample was extracted using 10 ml of solution for 5 min. The samples were centrifuged and filtered (0.4 µm GF filters) before analyses using an ICP-QQQ (Agilent, Japan). A semi-micro modification of perchloric acid digestion method for the determination of total P in soils, sediments and organic materials (Kopáček et al. 2001) was used to analyse the composition of the particles smaller than 0.5 mm. Samples were digested for 30 minutes in nitric acid at 115 °C and then for 2 hours with

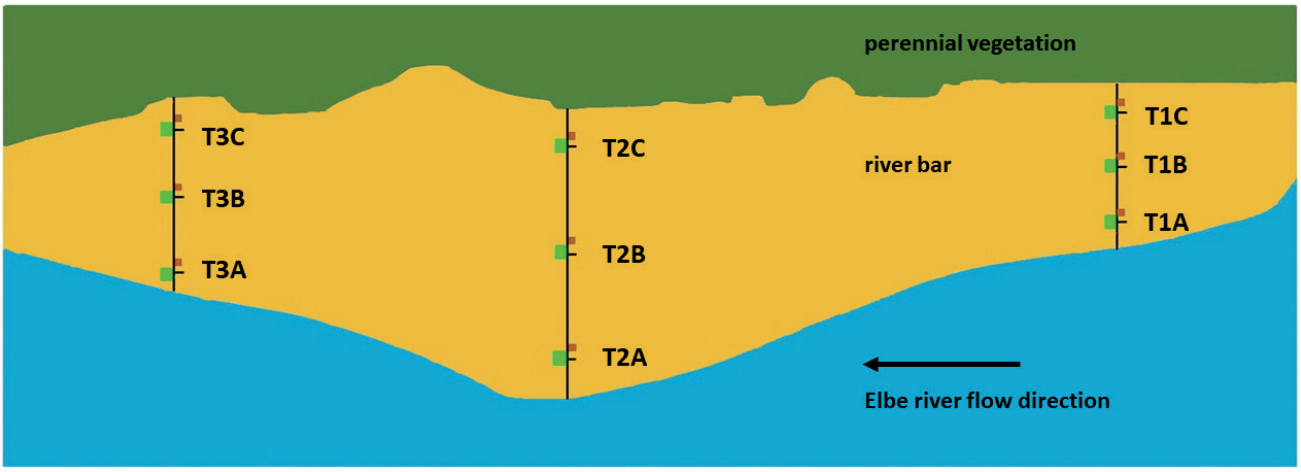

Fig. 2 Positions along and across the plots sampled (green dots) at each site.

perchloric acid at 170 °C in an aluminum heating block before analyses using an ICP-QQQ (Agilent, Japan).

Data processing

Linear regression coefficients and Pearson's correlation coefficients were used to describe the relationships between the physical and chemical properties of the substrate and their position on the gravel bar (the position on the bars was entered categorically). Due to the large number of variables studied, only those coefficients that were significant at $p < 0.05$, when the Bonferroni correction was applied, were used. To test whether the chemical properties of the natural gravel bars are similar to those of artificial bars, only samples from the leading edge of the bars were collected as bars were relatively short in the downstream direction no comparable samples were available downstream. Natural and artificial gravel bars were compared using a two-way ANOVA done in Statistica 13.0, in which habitat, i.e., natural or artificial, and the distance of the source of the sample from the shore were explanatory variables.

Results and Discussion

Natural river bars

The distribution of grain size is associated with position on the bar, with the proportion of fine grains, i.e. those 63–250 μm and below 0.5 mm, is correlated significantly with downstream locations ($r = 0.407$ and 0.435). The ANOVA also indicates significantly higher proportions of fine grains (<125 μm and >63 μm) in the most downstream location on the bars (Fig. 3A, Table 2; data shown only for one grain size, but all fractions vary significantly along the bars and have the same pattern). This distribution is consistent with the grain size distribution observed in river bars in other river systems (Rice and Church 1998; Purkait 2006), which is due to the decreasing velocity of water flowing over the bar, which results in sedimentation of coarser particles mainly upstream and finer particles downstream. In contrast to the findings of Sin et al. (2015), no significant correlations were recorded with the location of the site or the content of individual nutrients, in the current study. In addition, significant

Table 2 Mean values (±SD) of individual parameters recorded on natural river bars and effect of upstream and downstream and flow across bars (from river to adjacent land) on the parameters evaluated by two-way ANOVA, p values for effect of across and position along a bar are shown, ns = not significant.

	Parameter	Along bar	Across bar	Mean value ± SD
Total content	K	0.0069	ns	10.28 ± 3.43
mg g^{-1}	Al	0.0228	ns	0.74 ± 0.25
	P	ns	ns	4.30 ± 1.52
	Ca	0.0173	ns	0.03 ± 0.01
	Cr	0.0113	ns	0.92 ± 0.45
	Mn	0.0046	ns	15.35 ± 4.54
	Fe	0.0008	0.0363	0.01 ± 0.01
	As	ns	ns	2.58 ± 0.80
	Mg	0.0178	ns	0.11 ± 0.04
Available	K	0.0227	ns	379.85 ± 108.20
mg kg^{-1}	Al	ns	ns	74.10 ± 16.90
	P	ns	ns	1,922.92 ± 646.17
	Ca	ns	ns	0.30 ± 0.05
	Cr	ns	ns	151.53 ± 46.03
	Mn	0.0157	ns	305.32 ± 75.61
	Fe	ns	0.0025	0.69 ± 0.11
	As	ns	0.0331	187.16 ± 72.02
	Mg	ns	ns	32,621.09 ± 20,954.28
Texture	>50 mm	ns	ns	32.06 ± 11.76
%	20–50mm	ns	ns	14.87 ± 8.42
	5–20 mm	ns	ns	5.22 ± 3.55
	2–5 mm	ns	ns	10.27 ± 5.34
	0.5–2 mm	ns	ns	1.63 ± 1.10
	250–500 μm	ns	ns	0.90 ± 0.55
	125–250 μm	0.0069	ns	0.72 ± 0.45
	63–125 μm	0.0331	ns	0.75 ± 0.50
	<63 μm	0.0154	ns	4.03 ± 1.55
Organic matter %		ns	ns	4.79 ± 2.93

correlations between nutrient contents and the proportion of individual grain sizes in sediments are rare (Table 3), although other authors (Steiger and Gurnell 2003; Turner et al. 2007) report an increase in nutrients with increase in the proportion of fine sediment. There is no correlation between individual elements and position on the bar. However, the ANOVAs of the positions of elements along and across bars (depicted in Fig. 2) revealed significant effect of position along bars for total K, Al, Ca, Cr, Mn, Fe, Mg and available K and Mg, and significant effect across bars on total Fe and available Fa and As (Table 2, Figs 3B–C). For all elements with significant associations with position along bars the values in the central part of the bars were significantly higher than those for the most downstream and upstream locations (Fig. 3B). For elements with significant associations with positions across bars the highest values were for the positions closest to the land (Fig. 3C). Interestingly, the distribution of total phosphorus, which is an important plant nutrient is not affected by the position on the natural bars. In contrast to grain size, most elements, including the key nutrients, are barely significantly correlated with the organic content in the sediment (Table 3).

This indicates that the nutrient status of river bars is not primarily determined by the granular properties of the sediments, but with complex interactions with river flow and erosion of material from the adjacent land possibly supplying the nutrients. Similar complex nutrient dynamics are also reported by Claret et al. (1997) and Maazouzi et al. (2013).

Table 3 Correlation between the content of nutrients, grain size of the substrate and the content of organic matter: A available nutrients, T total nutrient content, data presented in units of length refer to grain sizes. Only correlation coefficients that are statistically significant at $p<0.05$ when applying the Bonferroni correction are listed.

	Na – T	K – T	Al – T	P – T	Ca – T	Cr – T	Mn – T	Fe – T	As – T	Mg – T	K – A	Al – A	P – A	Ca – A	Cr – A	Mn – A	Fe – A	As – A	Mg – A
Na – T	1.00																		
K – T	0.42	1.00																	
Al – T	0.45	0.96	1.00																
P – T	0.43	0.86	0.94	1.00															
Ca – T	0.47	0.89	0.86	0.76	1.00														
Cr – T		0.84	0.85	0.75	0.77	1.00													
Mn – T	0.41	0.88	0.85	0.78	0.83	0.79	1.00												
Fe – T	0.54	0.88	0.89	0.76	0.83	0.88	0.82	1.00											
As – T		0.00	0.41	0.00				0.52	1.00										
Mg – T	0.53	0.89	0.93	0.85	0.83	0.79	0.80	0.84		1.00									
K – A		0.77	0.79	0.72	0.69	0.62	0.72	0.67		0.79	1.00								
Al – A		0.68	0.79	0.73	0.63	0.73	0.69	0.77		0.75	0.77	1.00							
P -A		0.68	0.62	0.53	0.65	0.53	0.67	0.61		0.61	0.67	0.52	1.00						
Ca – A		0.74	0.74	0.65	0.81	0.61	0.70	0.64		0.71	0.81	0.73	0.71	1.00					
Cr – A															1.00				
Mn – A		0.58	0.48		0.59	0.45	0.78	0.56		0.50	0.54	0.40	0.66	0.48		1.00			
Fe – A		0.49	0.40		0.47	0.45	0.59	0.58		0.43		0.46	0.69			0.73	1.00		
As – A		0.49	0.43		0.49	0.50	0.49	0.64		0.44		0.50	0.67	0.45	0.44	0.55	0.85	1.00	
Mg – A		0.65	0.76	0.78	0.63	0.55	0.59	0.59		0.75	0.78	0.78	0.48	0.80					1.00
>50 mm																			
20–50 mm																0.42			
5–20 mm																			−0.47
25 mm																			
0.5–2 mm													−0.42						−0.56
250–500 µm										−0.46	−0.44			−0.49					−0.51
125–250 µm																			−0.44
63–125 µm																			−0.46
<63 µm																			−0.45
Org. matter.		0.68	0.72	0.70	0.54	0.54	0.55	0.57	0.00	0.65	0.63	0.59	0.56	0.61					0.64
<0.5mm																			

Significant correlations were recorded between nutrients, indicating that they are all associated with the same environmental gradient (Table 3). This indicates that nutrient content is not associated with the sorption properties of the sediment but is most likely determined by the flux of nutrients from the riparian ecosystem into the river. This flux can be further influenced by biotic interactions at upwellings and on the surfaces of the sediment, which can influence both the total supply and the availability of nutrients determined by mobilization and immobilization, both of which are influenced by redox conditions.

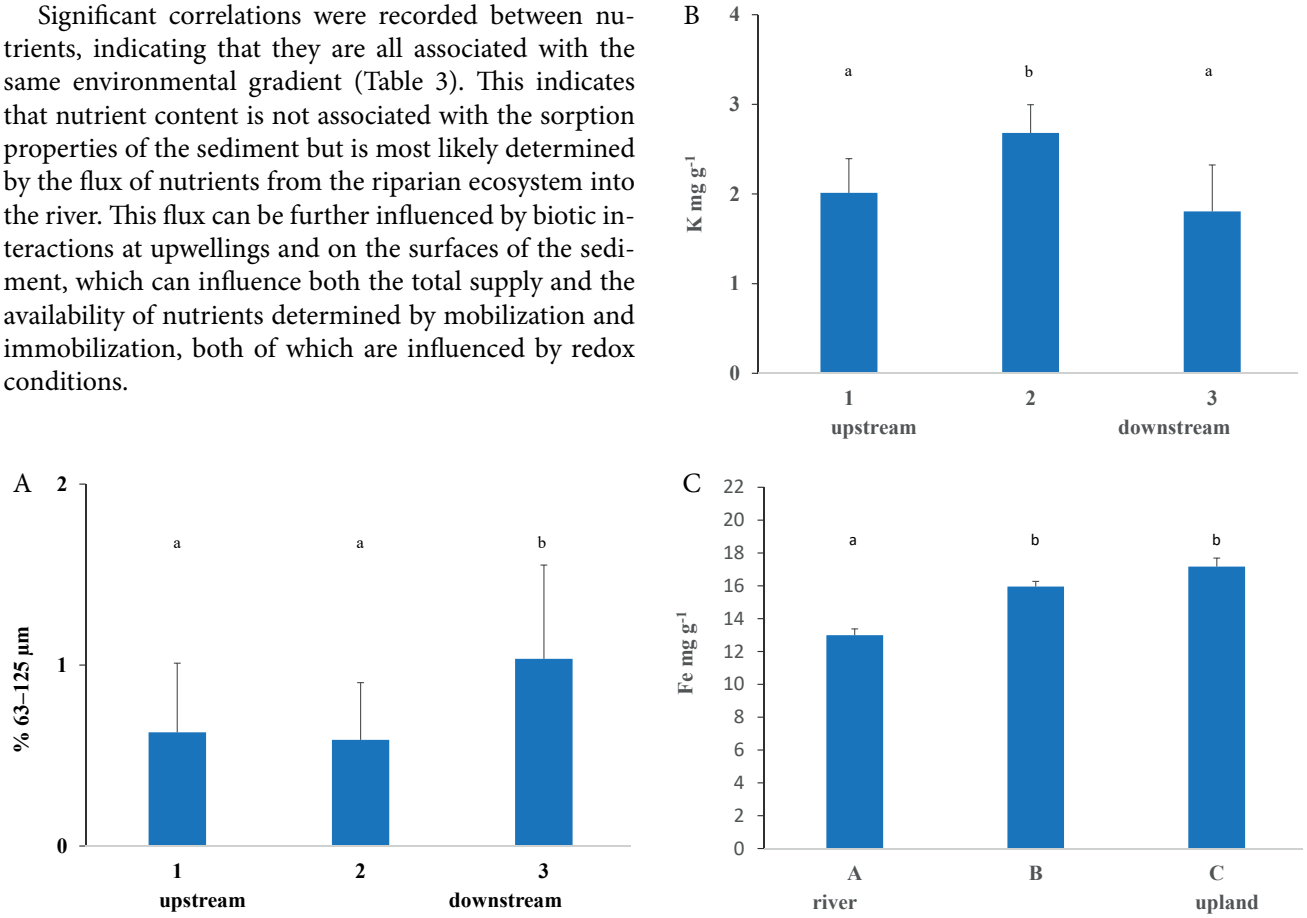

Fig. 3 Examples of the distribution of material of different grain sizes and selected elements along and across natural river bars A) fraction 125–63µm B) K content along profile and C) Fe content across profile.

Comparison of natural and artificial river bars

Comparison of artificially created and natural river bars revealed statistically significant differences in the content of total nutrients (K, Al, P, Ca, Cr, Mn, Fe, Mg) and available nutrients (K, Al, Ca, Mg) as well as organic matter. In addition, there are significant differences in the granular composition of the sediment (Table 4 and Fig. 4).

As described above and reported by other authors (Claret et al. 1997; Maazouzi et al. 2013), the factors that determine the spatial distribution of nutrients and other elements on a bar are complex. This can be further affected by the development of vegetation, which can affect sedimentation (Steiger et al. 2003) and trigger additional effects (Frouz 2024), such as the formation of microbial growth, which in turn can influence the mobilization and immobilization of nutrients. These complex interactions may be one of the reasons why it is technically difficult to imitate natural river bars and why technically restored river bars differ in nutrient status from naturally formed bars (Table 4). In particular, artificial river bars have significantly higher P and organic matter content and a strong gradient across the bar, with it being much higher near the adjacent land and decreases towards the river. Thus, artificial bars retain organic matter and associated nutrients brought in either by the river or from the surrounding land. Although this has not been studied, it is likely that higher nutrient status promotes fast-growing vegetation that recycles nutrients faster and triggers a number of other processes that increase the nutrient differences between natural and artificial bars (Frouz 2024).

Conclusion

The results show that naturally formed river bars differ from artificial ones in their nutrient status. Detailed records of the nutrient distribution in natural river bars indicate that it is associated with the distribution of organic matter, but the final pattern is a consequence of a complex interplay of several factors. The complexity of these factors is the most likely reason why the nutrient distribution in natural river bars hosting *Corrigiola litoralis* is difficult to mimic technically.

Acknowledgements

This study was funded by the Technology Agency of the Czech Republic, grant number SS03010279 (Management optimization of the Elbe lower reach with respect

Table 4 The effect of natural or artificial origin of gravel bars and distance from shoreline determined using two-way ANOVA, numbers are p values for individual factors and their interactions with only p values <0.05 presented. Only the upstream part of natural bars was considered for comparison.

		Natural bars mean value ± SD	Artificial bars mean value ± SD	Position (distance from shoreline)	Natural vs. artificial bars	Interactions
Tolal content	K	2.02 ± 0.58	2.50 ± 0.83	0.0048	0.0421	ns
mg g^{-1}	Al	9.87 ± 2.81	14.01 ± 4.45	0.0069	0.0014	ns
	P	0.72 ± 0.20	1.03 ± 0.30	ns	0.0021	ns
	Ca	4.09 ± 1.47	5.53 ± 1.60	ns	0.0219	ns
	Cr	0.02 ± 0.01	0.03 ± 0.01	0.0115	0.0174	ns
	Mn	0.88 ± 0.40	1.26 ± 0.48	ns	0.0338	ns
	Fe	14.94 ± 3.95	20.66 ± 7.58	0.0032	0.0029	ns
	As	0.01 ± 0.01	0.01 ± 0.01	0.018	0.0641	ns
	Mg	2.52 ± 0.72	3.46 ± 0.82	ns	0.0035	ns
Available content	K	110.69 ± 37.44	145.60 ± 44.54	ns	0.0359	ns
mg kg^{-1}	Al	382.03 ± 111.90	610.11 ± 243.75	0.0379	0.0004	ns
	P	74.31 ± 16.47	80.582 ± 10.03	ns	ns	ns
	Ca	1 891.21 ± 570.46	2,481.97 ± 867.92	ns	0.0285	ns
	Cr	0.30 ± 0.10	0.30 ± 0.10	ns	ns	ns
	Mn	144.95 ± 43.55	159.66 ± 309.88	ns	ns	ns
	Fe	303.51 ± 70.34	353.63 ± 108.48	0.0061	0.0881	ns
	As	0.70 ± 0.10	77.10 ± 20.80	0.0006	ns	ns
	Mg	187.20 ± 51.17	299.42 ± 104.56	ns	0.0002	ns
Texture %	>50 mm	37.54 ± 20.08	40.38 ± 17.62	ns	ns	ns
	20–50mm	31.67 ± 11.10	32.71 ± 12.75	ns	ns	ns
	5–20 mm	12.76 ± 6.06	11.24 ± 4.92	ns	ns	ns
	2–5 mm	4.56 ± 2.60	5.83 ± 2.96	ns	ns	ns
	0.5–2 mm	9.04 ± 3.53	6.37 ± 2.63	ns	ns	ns
	250–500 µm	1.51 ± 0.97	1.03 ± 0.48	ns	ns	ns
	125–250 µm	0.83 ± 0.52	0.74 ± 0.46	ns	ns	ns
	63–125 µm	0.62 ± 0.38	0.55 ± 0.32	ns	ns	ns
	<63 µm	0.67 ± 0.45	0.64 ± 0.35	ns	ns	ns
Organic matter %		4.01 ± 1.47	5.32 ± 2.18	0.0028	0.0296	0.0367

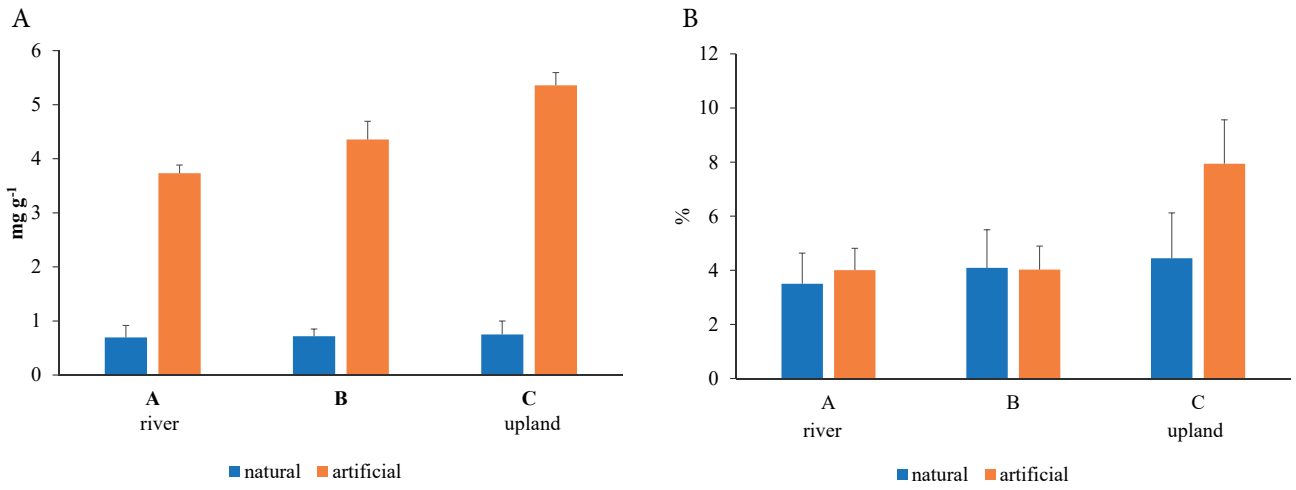

Fig. 4 Distribution of phosphorus A) and organic matter B) along the gradient depicted in Fig. 2 from river to adjacent terrestrial habitat compared on the upstream part of natural bars with that on artificial bars.

to the presence of 3270 biotope and improvement of the hydro morphological state as based on an interdisciplinary study).

REFERENCES

Bejček V, Volfová E (2019) Bahnité náplavy v ČR a na Labi (Muddy alluvia in the Czech Republic and on the Elbe River). Ochrana Přírody 2: 24–27, (in Czech).

Bendix J, Stella JC (2013) Riparian vegetation and the fluvial environment: A biogeographic perspective. In: Shroder JF, Butler DR, Hupp CR (eds) Treatise on Geomorphology. Ecogeomorphology, Vol 12, Academic Press, San Diego, pp 53–74.

Claret C, Marmonier P, Boissier J-M, Fontvieille D, Blanc P (1997) Nutrient transfer between parafluvial interstitial water and river water: influence of gravel bar heterogeneity. Freshwater Biol 37: 657–670.

Eekhout JPC, Hoitink AJF, Mosselman E (2013) Field experiment on alternate bar development in a straight sand-bed stream. Water Resour Res 49: 8357–8369.

Frouz J (2024) Plant-soil feedback across spatiotemporal scales from immediate effects to legacy, Soil Biol Biochem 189: 109289, doi: 10.1016/j.soilbio.2023.109289.

González E, Sher AA, Tabacchi E, Masip A, Poulin M (2015) Restoration of riparian vegetation: A global review of implementation and evaluation approaches in the international, peer-reviewed literature. J Environ Manage 158: 85–94.

Havlíček V, Heřmanovský M, Bureš L, Martínková M, Čuda J, Hanel M (2023) The site dynamics of *Corrigiola litoralis* (Strapwort) on the Elbe River in Czechia: A combined hydrological and hydrodynamic approach. Ecohydrology, e2586.

Juříček M (2013) Zajímavé floristické nálezy z dolního Labe (Interesting floristic findings from the lower part of Elbe River). Severočes Přír 44: 59–72, (in Czech).

Kopáček J, Borovec J, Hejzlar J, Porcal P (2001) Spectrophotometric determination of iron, aluminum, and phosphorus in soil and sediment extracts after their nitric and perchloric acid digestion. Commun. Soil Sci Plant Anal 32: 1431–1443.

Li J, Claude N, Tassi P, Cordier F, Crosato A, Rodrigues S (2023) River restoration works design based on the study of early-stage vegetation development and alternate bar dynamics. River Res Appl 39: 1682–1695.

Maazouzi C, Claret C, Dole-Olivier MJ, Marmonier P (2013) Nutrient dynamics in river bed sediments: effects of hydrological disturbances using experimental flow manipulations. J Soils Sediments 13: 207–219.

Mehlich A (1984) Mehlich 3 Soil Test Extractant. A Modification of the Mehlich 2 Extractant. Commun Soil Sci Plant Anal 15: 1409–1416.

Purkait B (2006) Grain-size distribution patterns of a point bar system in the Usri River, India. Earth Surf Process Landforms 31: 682–702.

Rice S, Church M (1998) Grain size along two gravel-bed rivers: statistical variation, spatial pattern and sedimentary links. Earth Surf Process Landforms 23: 345–363.

Sin Y, Lee E, Lee Y, Shin K-H (2015) The river-estuarine continuum of nutrients and phytoplankton communities in an estuary physically divided by a sea dike. Estuar Coast Shelf Sci 163: 279–289.

Steiger J, Gurnell AM (2003) Spatial hydrogeomorphological influences on sediment and nutrient deposition in riparian zones: observations from the Garonne River, France. Geomorphology 49: 1–23.

Turner RE, Rabalais NN, Alexander RB, McIsaac G, Howarth RW (2007) Characterization of Nutrient, Organic Carbon, and Sediment Loads and Concentrations from the Mississippi River into the Northern Gulf of Mexico. Estuaries Coasts 30: 773–90.

POTENTIAL OF SATELLITE IMAGERY FOR STUDYING THE SPATIAL DISTRIBUTION OF FOG AND ITS ROLE IN ATMOSPHERIC DEPOSITION

IVA HŮNOVÁ[1,2,*] AND SURUCHI[1]

[1] Charles University, Faculty of Science, Institute for Environmental Studies, Benátská 2, 128 00 Prague 2, Czech Republic
[2] Czech Hydrometeorological Institute, Na Šabatce 17, 143 06 Prague 4 – Komořany, Czech Republic
* Corresponding author: iva.hunova@chmi.cz

ABSTRACT

Fog is important in that it contributes significantly to atmospheric deposition, especially in mountainous areas. The aim of this paper is to provide information on the possible use of satellite imagery for the analysis of spatiotemporal changes in the occurrence of fog and for determining the areas prone to fog in the Czech Republic. Satellite imagery is used to identify fog and determine its limitations. Both the advantages and limitations of this approach in determining patterns in the spatial distribution of fog are discussed. Finally, the improvements that can be expected in the understanding of the role of fog in atmospheric deposition processes are discussed. In this context, the identification of fog-prone areas and the estimation of their spatial extent, where the fog pathway can contribute substantially to total deposition fluxes, is of utmost importance.

Keywords: atmosphere; ground-based observations; hydrometeor; satellite data analysis; spatial coverage

Introduction

Fog is important in that it has significant effects on both human society and the environment (Croft 2003; Seinfeld and Pandis 2006; Weathers et al. 2020). Fog is a hydrometeor, which consists of a suspension of tiny water droplets that reduce horizontal visibility to less than 1 km (WMO 2017). Fog droplets are very small, typically less than 100 μm in size, which is much smaller than raindrops, which can be up to 6 mm in diameter (Pérez-Diaz et al. 2017). Fog is formed when moist air cools down and its temperature reaches or approaches the so-called dew-point temperature in the presence of a sufficient number of condensation nuclei. In terms of its formation, fog is further classified into radiation (Fig. 1), orographic (Fig. 2), advection and steam (Khoury et al. 2023). As it has adverse effects on all types of transport, fog is recorded worldwide by national weather services and much effort is invested in its forecast, which is still a challenge (Steeneveld et al. 2015). Long-term temporal trends in the incidence of fog are sometimes increasing and sometimes declining, although in general they are decreasing in most places due to rising temperatures associated with climate change and decreasing ambient air pollution caused by the introduction of more stringent air quality legislation and advanced technical countermeasures (Vautard et al. 2009; van Oldenborgh et al. 2010; Klemm and Lin 2016; Hůnová et al. 2020).

Fog formation is a very complex atmospheric process depending on numerous factors, such as synoptic situation, ambient air pollution, altitude, geomorphology and water availability in the landscape (Bruijnzeel et al. 2006; Gultepe et al. 2007; Hůnová et al. 2018, 2021a, b, 2022; Pauli et al. 2022, Walzelova et al. 2025). Both the physics and chemistry of fog are still not fully understood, and the contribution of fog to the water cycle and its effects on the environment are largely overlooked (Křeček et al. 2017; Palán and Křeček 2018; Hůnová et al. 2020). However, there is a general consensus that the role of fog in atmospheric deposition is very important for ecosystems, both in terms of water, nutrient and pollutant inputs

Fig. 1 Dense radiation fog persisting over several consecutive days in Czech lowlands, end of December 2024. This dense fog event was caused by a strong thermal inversion, trapping cold air under a "lid" of warmer air. Kokořínsko Protected Landscape Area, December 28, 2024 (photographer Iva Hůnová).

Fig. 2 Fog drip can substantially enhance the deposition fluxes of both nutrients and atmospheric pollutants, especially in mountain forests, where fog occurs frequently. Fog drip wetting ecosystems in the Jizerské hory Mts., autumn 2017 (photographer Iva Hůnová).

Hůnová, I., Suruchi: Potential of satellite imagery for studying the spatial distribution of fog and its role in atmospheric deposition
European Journal of Environmental Sciences, Vol. 15, No. 1, pp. 12–17
https://doi.org/10.14712/23361964.2025.2

(Weathers et al. 2020; Chang and Schemenauer 2021). This is particularly true in mountain regions, where fog (or clouds at ground level) occurs frequently throughout the year (Fig. 2). Furthermore, it is reported that fog is more polluted than rain in the same region, which results in a significantly higher input of air pollutants (or nutrients) into fragile mountain ecosystems (Thalmann et al. 2002; Zimmermann and Zimmermann 2002; Lange et al. 2003; Blas et al. 2010).

The occurrence of fog is regularly reported by weather services around the world (Gultepe et al. 2007), either by professional observers or by PWD sensors (Present Weather Detectors). In addition to the reporting of the frequency of fog the density, physics and chemistry of fog have been studied both experimentally and in the field. However, these studies are for particular localities or small geographical areas. In order to estimate the contribution of fog to atmospheric deposition, there is an urgent need to know not only point-wise data on fog occurrence, but also how fog occurrence changes in time and space, which areas are prone to fog formation, and generally, to understand the spatial occurrence of fog. Exploring the spatial behavioral patterns of fog is challenging for many reasons (Hůnová 2024), but recently remote sensing has emerged as a promising tool for determining changes in the occurrence of fog in time and space using satellite images (Bendix 2002; Cermak 2018; Egli et al. 2019; Pauli et al. 2024). The aim of this paper is to summarise how satellite imagery can improve our knowledge of fog behaviour and its role in atmospheric deposition.

Satellite imagery

Satellite imagery has proven to be a very efficient tool for studying our environment and greatly improving our understanding of many phenomena previously based exclusively on ground measurements and observations (Burke et al. 2021). When using satellite imagery for exploring the Earth surface properties (such as in ecosystem studies, environmental conservation, urban planning, forestry, agriculture, etc.), the presence of atmospheric phenomena (such as clouds, atmospheric aerosols, etc.) often negatively affect satellite images, so efforts are needed and numerous corrections made to eliminate their effect (Stamnes et al. 2005; Li et al. 2022). However, here the challenge is different. Unlike studies of relatively stable objects on the Earth's surface, where the removal of "atmospheric contamination" is of the utmost importance, the study of fog involves observing a rapidly changing situation in time and space that needs to be recorded in detail. Satellite imagery is already used for weather analysis and forecasting, frequently in combination with other advanced approaches, such as machine learning and deep learning methods, a part of artificial intelligence, consisting mostly of artificial neural networks inspired by the functions of neurons in the human brain (Moskolai et al. 2021; Lara-Alvarez et al. 2024; Upadhyay et al. 2024). Although conventional methods for observing fog provide high-precision records of their occurrence, deficiencies in their spatial occurrence has led to research since the 1970s into the possibility of identifying fog using satellite imagery (Yao et al. 2025). So far, satellite imagery has resulted in a better identification of the fog life cycle, especially the spatio-temporal patterns of fog, although there are still issues to be addressed to refine this approach. Among the most important are: (i) the difficulty of distinguishing fog touching the ground from low stratus clouds which can be located even several hundred meters above the ground, (ii) the reduced accuracy in detection of fog and low stratus clouds (FLS) at night, and (iii) the need for ground-based validation and advanced classification methods to improve detection reliability (Bendix 2002; Bendix et al. 2005; Bendix et al. 2006; Cermak et al. 2008; Andersen and Cermak 2018; Egli et al. 2019; Pauli et al. 2022; Pauli et al. 2024).

Satellite products suitable for studying fog

A number of satellite products (processed and derived information extracted from satellite imagery) are available for the identification and analysis of fog, each with different advantages and limitations. One of the key instruments for detecting fog over Europe is the Spinning Enhanced Visible and Infrared Imager (SEVIRI), on board the Meteosat Second Generation (MSG) satellites.

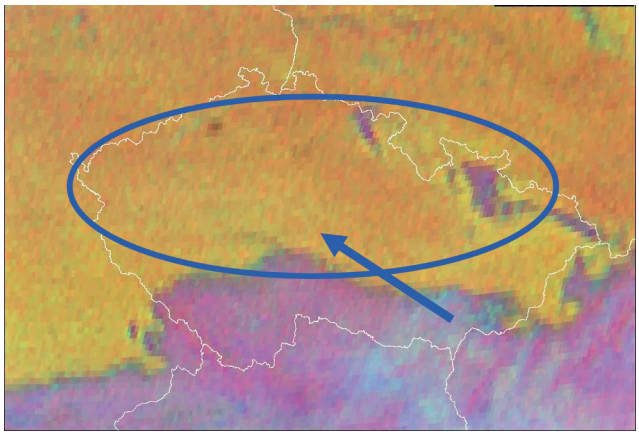

Fig. 3 Fog and low stratus clouds appear in yellowish hues, highlighting areas where these atmospheric conditions are present in the SEVIRI 24-hour Microphysics RGB imagery.

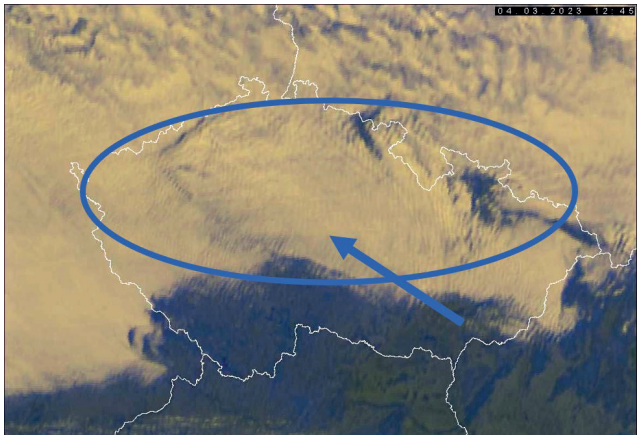

Fig. 4 Olive green areas represent fog or low cloud in the VIS-IR imagery during daytime.

One of the most widely used products for monitoring FLS is 24-hour Microphysics Red, Green, Blue (RGB). In this imagery, FLS appear in yellowish hues (Fig. 3) and therefore are easily tracked continuously during the day and night. Another useful SEVIRI product is High-Resolution Visible (HRV) Fog RGB imagery, which depicts FLS in shades of pink, which enhances the clarity of daytime assessments. In addition, the Visible-Infrared (VIS-IR) RGB combination for FLS detection is available and the HRV SEVIRI channel has a higher spatial resolution, FLS are depicted as olive green (Fig. 4), which is very different from the pinkish colours used in HRV fog-detection system.

This sensor offers a very high temporal resolution with one scan every 15 minutes and a nadir spatial resolution of 3 km (HRV channel 1 km), which makes it ideal for recording the spatiotemporal variability of fog. The nadir spatial resolution is an important term in satellite imagery, which refers to the point on the Earth's surface located vertically below the centre of the system, where the finest resolution of satellite imagery occurs. The FLS detection technique proposed by Andersen and Cermak (2018) uses the satellite-based thermal infrared data from the SEVIRI satellite, which enables the continuous and diurnal identification of FLS (Cermak and Bendix 2008; Egli et al. 2019).

VIS-IR imagery is more effective at detecting fog than 24-hour Microphysics RGB imagery. This is mainly because VIS-IR provides better resolution and contrast and can better distinguish fog from other types of cloud. The combination of visible and infrared channels in VIS-IR improves the ability to identify fog based on its specific thermal and reflective characteristics (Ellrod 2002; Cermak and Bendix 2008). In contrast, 24-hour microphysical RGB imagery uses a broader spectral range, which can sometimes mask the subtle differences between fog and other low-level clouds (Cermak and Bendix 2008).

Other satellite sensors suitable for detecting fog are the Moderate Resolution Imaging Spectroradiometer (MODIS) on the National Aeronautics and Space Administration's (NASA) Terra and Aqua satellites. This sensor returns visible and infrared data with an up to 1 km spatial resolution. The MODIS products are widely used for daytime identification of fog, since they can distinguish fog from other cloud types based on their optical characteristics (Cermak and Bendix 2008). Similar to other sensors, the Visible Infrared Imaging Radiometer Suite (VIIRS) onboard NOAA's polar-orbiting satellites is limited in its ability to track fog dynamics, as its data are available only for long periods of time. In addition to the straightforward use of SEVIRI imagery, a Self-Organizing Map, SOMs (Egli et al. 2019) has been used for the thorough analysis and classification of fog patterns derived from satellite data. SOMs belong to a category of artificial neural networks developed for reducing the dimensional complexity of complex datasets, such as the satellite-derived fog frequency maps (Hewitson and Crane 2002; Liu and Weisberg 2011). Every neuron in the SOM represents a particular pattern related to fog, while the neighbouring neurons in the SOM grid reflect similar situations regarding fog, which helps in finding transitions between different states of fog. The additional value of this approach is the classification of fog into different classes; it allows identification of persistent patterns of fog and their linkage to meteorological conditions (Egli et al. 2019). Furthermore, unlike traditional clustering methods, SOMs allow for variations in cluster sizes, making them particularly suitable for meteorological applications in which fog occurrence is highly spatially heterogeneous (Tambouratzis and Tamboutratzis 2008).

In addition, satellite fog detection is very often complemented by ground-based validation networks that provide ground-level observations of fog patterns. These ground-based measurements are used to validate and refine the accuracy of satellite-derived products of fog. For example, the FLS detection method based on SEVIRI was compared to surface net radiation measurements, which is another demonstration of its accuracy and suitability for studying fog (Egli et al. 2019).

What improvements can be expected from using the satellite approach?

The occurrence of fog is regularly observed at the professional weather stations. However, these regular observations of fog occurrence carried out at professional weather stations provide an information of a strictly point-wise character (Tolasz et al. 2007), representing only a close (and not clearly defined) area around the observer standpoint. Large areas between the weather stations are not observed at all. Although fog can be easily detected using ground-based observations, observing sites are sparse and therefore fog is missed in unobserved areas or in vertical profile (Izett et al. 2019). By contrast, the use of satellite retrievals allows us to obtain information even for these unobserved areas, and we are able to get a clear picture of the real spatial pattern of fog formation.

An example for all: in the Czech Republic we have a professional weather station Churáňov assumed to observe the whole of the Šumava mountain range, which covers about 1600 km^2, including the largest national park in the CR, which extends over 680 km^2. When we observe fog formation in Churáňov, we do not know exactly how far the fog (when observed) extends, and how large area it covers. However, from the satellite images we can see the larger area where fog is present, which is exactly what we need to know in terms of atmospheric deposition fluxes in order to understand in what areas the fog deposition pathway can contribute significantly to total deposition with potential harm effects to sensitive mountain ecosystems.

It is known that fog formation can be a very local phenomenon, showing a distinct and steep horizontal gradient (Hůnová 2024). In contrast to point-wise observa-

tions, satellite imagery provides valuable information of a spatial character, allowing us to study fog patterns over the whole regions (Pauli et al. 2024). In addition, satellite images provide more frequent temporal information, with retrievals every 15 minutes of the day, allowing us to observe fog virtually live: we can closely follow each fog event formation, its evolution, its movements and, finally, its dissipation (Andersen and Cermak 2018).

Thus, development of satellite sensors, such as SEVIRI and MODIS, which provide finer spatial resolution (3 km) and high temporal resolution (15 minutes scans) offering continuous area coverage, get around the drawbacks of point-wise ground fog observations. Furthermore, more precise identification and classification of fog patterns and their dynamics in connection to meteorological conditions are made possible by enhanced detection algorithms and machine learning techniques, such as SOMs. The development and spatial diversity of fog events may now be captured in far more detail thanks to technological advancements.

What improvements can be expected in the understanding of the role of fog in atmospheric deposition?

The use of satellite imagery can greatly improve the understanding of fog formation and could become the main way of identifying fog-prone areas where increased deposition fluxes via fog can be expected. Pauli et al. (2022) have recently identified patterns in fog formation and dissipation in Central Europe, based on a ten-year dataset. These spatial patterns reveal the important influence of the underlying topography. In addition, knowledge of the topography of a specific region can be used to identify the type of fog, radiation (in lowlands) or orographic (a cloud "sitting" on the top of a mountain), which are the most frequent types of fog occurring in Central Europe (Pauli et al. 2022). We are not able to distinguish between these different types directly from photographs (Figs 1 and 2) or satellite images. However, in combination with knowledge of the underlying terrain, this differentiation is possible.

These fogs differ in their chemistry (Hůnová 2024). Radiation fogs forming in lowlands are less frequent than orographic fogs forming in the mountains but are more contaminated as they originate in more polluted parts of the atmosphere, directly influenced by the Earth's surface (Burkard et al. 2003; Blas et al. 2010; Michna et al. 2015). For example, in Poland, Blas et al. (2010) report 3–4 times higher total inorganic ion content and even 3–6 greater total dissolved pollutant load in radiation fog than in orographic fog in the Polish part of the Giant Mts.

Although this difference in the chemical composition of radiation and orographic fog may be smaller in countries with less polluted air than Poland, it is reasonable to assume that this is a general relationship. However, in spite of their cleaner character, orographic fogs in mountains are assumed to contribute significantly more to deposition fluxes of environmentally relevant substances

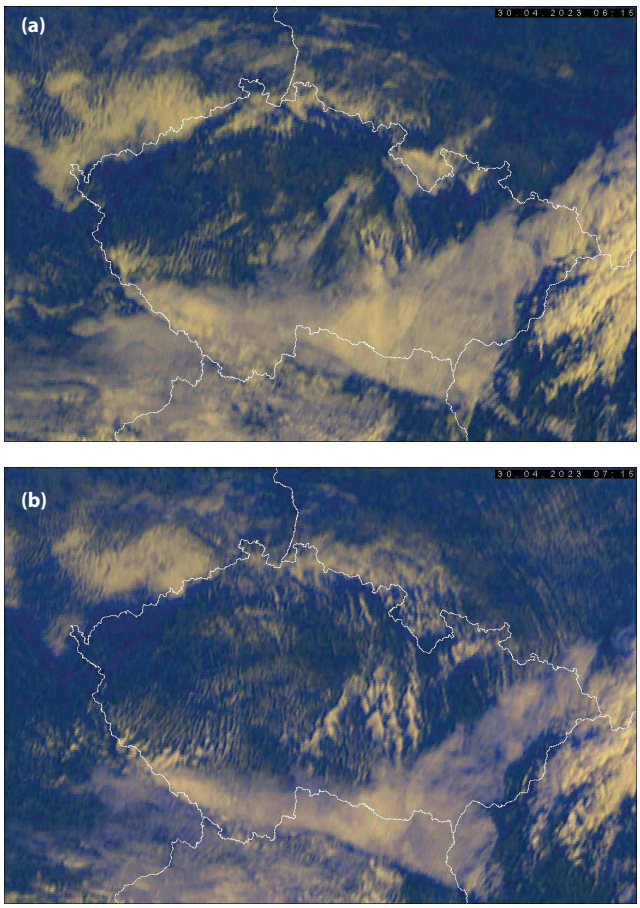

Fig. 5 VIS-IR satellite imagery showing the development of fog (olive green colour) over the Czech Republic, April 30, 2023, 6.15 a.m. (a), and 7.15 a.m. (b).

due to their higher frequency and presumably much larger water volume. The use of satellite imagery to observe the spatial patterns of fog in much greater detail (Fig. 5) than has been possible up to now, can reduce the underestimation of deposition fluxes in mountain regions and make them more suitable for ecological and environmental studies.

Limitations that must be accounted for

Satellite fog detection also has some limitations and drawbacks, such as the problem of distinguishing fog from low stratus clouds using thermal infrared imagery. The thermal properties of FLS are very similar, making it rather complicated for satellite sensors, such as SEVIRI and MODIS to distinguish between them (Bendix et al. 2005). Both fog and low stratus clouds have similar radiative properties in the thermal infrared spectrum, which is a common reason for misclassifying low stratus as fog and vice versa (Egli et al. 2019). When low stratus layers are directly over the surface, they tend to resemble closely the radiative characteristics of fog. Many methods have been proposed for addressing this limitation, including combining satellite data with ancillary information, such as surface observations, knowledge on underlying terrain, or using sophisticated machine learning techniques. However, distinguishing between

the two still remains a significant task, especially when the auxiliary data are not available and we have to rely solely on satellite imagery (Cermak and Bendix 2011).

Another notable constraint of satellite-based fog detection is its reduced accuracy at night. In daytime, the detection of fog is enhanced by the use of data from the visible spectrum, which helps in the differentiation between fog and other hydrometeors. Conversely, at night, the absence of visible channels necessitates reliance exclusively on thermal infrared data (Bendix et al. 2006; Andersen and Cermak 2018). Night time detection is generally less accurate than that recorded during the day, because fog and surrounding surfaces, which also include low-lying clouds, often have similar thermal signatures, which make distinguishing between them even more difficult (Ellrod 1995). It follows that satellite sensors cannot rely on the unusual optical properties of fog in the visible spectrum that are particularly helpful during daytime.

In addition, nocturnal cooling of the surface may facilitate the development of fog; however, identifying this is often more difficult when relying solely on thermal infrared channels (Bendix et al. 2006). In various studies (Bendix et al. 2006; Egli et al. 2019) fog detection at night is reported to be very uncertain and requires additional information to improve the accuracy, such as temperature inversions and humidity profiles. SEVIRI's thermal infrared channels, while helpful in monitoring fog, are less effective at detecting fine-scale fog features at night, compared to when the combined use of visible and infrared data is used during the day (Cermak and Bendix 2011). Consequently, the reliance on thermal imagery alone leads to a higher likelihood of misclassification or under-detection of fog during night-time (Ellrod 1995).

Conclusions and future outlook

Satellite imagery has several advantages over the point-wise observations of fog currently routinely carried out at professional weather stations. These include continuous regional coverage, the capacity to record spatial variability, higher temporal resolution with frequent (15 min) retrievals and an enhanced ability to track the entire fog life cycle. The use of satellite images allows the study of spatial changes in fog formation at much finer temporal resolutions, which can significantly improve the understanding of fog formation and related atmospheric processes. The identification of fog-prone areas can help identify the areas where deposition fluxes of environmentally important substances have so far been underestimated or even neglected. The subsequent potential multi-step approach for fog deposition estimation in future should be based on the combination of measured and observed results from satellite imagery, ceilometers, LiDAR sensors, ground-based measurements of meteorology and air pollution, including the chemistry of fog droplets, allowing inference of both fog water volume and its chemical load, which in combination should result in fog deposition fluxes of individual chemical species. Combining knowledge of all the deposition pathways, i.e. dry, wet vertical and occult (including fog), will result in the more reliable input information needed for a better technique for accurately quantifying atmospheric deposition, which is necessary for both ecological and environmental studies.

Acknowledgements

The study was supported by the Charles University, project GA UK No. 146724 "New insights into fog role in atmospheric deposition using satellite images". The satellite images were kindly provided by the Satellite Department of the Czech Hydrometeorological Institute (CHMI). The authors are indebted for the invaluable consultations of Jindřich Šťástka from the CHMI.

REFERENCES

Andersen H, Cermak J (2018) First fully diurnal fog and low cloud satellite detection reveals life cycle in the Namib. Atmos Meas Tech 11: 5461–5470.

Bendix J (2002) A satellite-based climatology of fog and low-level stratus in Germany and adjacent areas. Atmos Res 64: 3–18.

Bendix J, Thies B, Cermak J, Naub T (2005) Ground Fog Detection from Space Based on MODIS Daytime Data – A Feasibility Study. AMS 20: 989–1005.

Bendix J, Thies B, Nauß T, Cermak J (2006) A feasibility study of daytime fog and low stratus detection with TERRA/AQUA-MODIS over land. Meteorol Appl 13: 111–125.

Blas M, Polkowska Z, Sobik M, Klimaszewska K, Nowinski K, Namiesnik J (2010) Fog water chemical composition in different geographic regions of Poland. Atmos Res 95: 455–469.

Bruijnzeel LAS, Eugster W, Burkard R (2006) Fog as a hydrologic input. Part 4. Hydrometeorology. Encycl Hydrol Sci. doi: 10.1002/0470848944.hsa041.

Burkard R, Butzberge RP, Euster W (2003) Vertical fogwater flux measurements above an elevated forest canopy at the Lägeren research site, Switzerland. Atmos Environ 37: 2979–2990.

Burke M, Driscoll A, Lobell DB, Ermon S (2021) Using satellite imagery to understand and promote sustainable development. Science 371. doi: 10.1126/science.abe8628.

Cermak J (2018) Fog and Low Cloud Frequency and Properties from Active-Sensor Satellite Data. Remote Sens 10: 1209.

Cermak J, Bendix J (2008) A novel approach to fog/low stratus detection using Meteosat 8 data. Atmos Res 87: 279–292.

Cermak J, Bendix J (2011) Detecting ground fog from space–a microphysics-based approach. Remote Sens 32: 3345–3371.

Chang SC, Schemenauer RS (2021) Fog Deposition. In: Foken T (eds) Springer Handbook of Atmospheric Measurements. Springer Handbooks. Springer, Cham.

Croft PJ (2003) Fog. In: Holton JR, Pyle JA, Curry JA (eds) Encyclopedia of Atmospheric Sciences. Academic Press, London, pp 777–792.

Egli S, Thies B, Bendix J (2019) A spatially explicit and temporally highly resolved analysis of variations in fog occurrence over Europe. Q J R Meteorol Soc 145: 1721–1740.

Ellrod GP (1995) Advances in the detection and analysis of fog at night using GOES multispectral infrared imagery. Weather Forecast 10: 606–619.

Ellrod GP (2002) Estimation of low cloud base heights at night from satellite infrared and surface temperature data. Natl Weather Dig 26: 39–44.

Gultepe I, Tardif R, Michaelidis SC, Cermak J, Bott A et al (2007) Fog research: a review of past achievements and future perspectives. Pure Appl Geophys 164: 1121–1159.

Hewitson BC, Crane RG (2002) Self-organizing maps: applications to synoptic climatology. Climate Res 22: 13–26.

Hůnová I (2024) Challenges in moving towards fog's contribution to spatial patterns of atmospheric deposition fluxes on a national scale. Sci Total Environ 946: 174208.

Hůnová I, Brabec M, Geletič J, Malý M, Dumitrescu A (2021a) Statistical analysis of the effects of forests on fog. Sci Total Environ 781: 146675.

Hůnová I, Brabec M, Geletič J, Malý M, Dumitrescu A (2022) Local fresh-and sea-water effects on fog occurrence. Sci Total Environ 807: 150799.

Hůnová I, Brabec M, Malý M, Dumitrescu A, Geletič J (2021b) Terrain and its effects on fog occurrence. Sci Total Environ 768: 144359.

Hůnová I, Brabec M, Malý M, Valeriánová A (2018) Revisiting fog as an important constituent of the atmosphere. Sci Total Environ 636: 1490–1499.

Hůnová I, Brabec M, Malý M, Valeriánová A (2020) Long-term trends in fog occurrence in the Czech Republic, Central Europe. Sci Total Environ 711: 135018.

Hůnová I, Hanusková D, Jandová K, Tesař M, Květoň J, Kukla J (2020) Estimate of the contribution of fog to wet atmospheric deposition in Czech mountain forests based on its stable hydrogen and oxygen isotope composition: preliminary results. Eur J Environ Sci 10: 89–97.

Izett JG, Schilperoort B, Coenders-Gerrits M et al. (2019) Missed Fog? Boundary-Layer Meteorol 173: 289–309.

Khoury D, Millet M, Jabali Y, Delhomme O (2023) Fog Water: A General Review of Its Physical and Chemical Aspects. Environments 10: 224.

Klemm O, Lin N-H (2016) What Causes Observed Fog Trends: Air Quality or Climate Change? Aerosol Air Qual Res 16: 1131–1142.

Křeček J, Palán L, Stuchlík E (2017) Acid atmospheric deposition in a forested mountain catchment. IFOREST 10: 680–686.

Lange CA, Matschullat J, Zimmermann F, Sterzik G, Wienhaus O (2003) Fog frequency and chemical composition of fog water – a relevant contribution to atmospheric deposition in the eastern Erzgebirge, Germany. Atmos Environ 37: 3731–3739.

Lara-Alvarez C, Flores JJ, Rodriguez-Rangel H, Lopez-Farias R (2024) A literature review on satellite image time series forecasting: Methods and applications for remote sensing. WIREs Data Min Knowl 14: e1528.

Li Z, Shen H, Weng Q, Zhang Y, Dou P, Zhang L (2022) Cloud and cloud shadow detection for optical satellite imagery: Features, algorithms, validation, and prospects. ISPRS J Photogramm Remote Sens 188: 89–108.

Liu Y, Weisberg RH (2011) A review of self-organizing map applications in meteorology and oceanography. In: Villmann T (ed) Self-organizing maps: applications and novel algorithm design. IntechOpen, pp 253–272.

Michna P, Werner RA, Eugster W (2015) Does fog chemistry in Switzerland change with altitude? Atmos Res 151: 31–44.

Moskolaï WR, Abdou W, Dipanda A, Kolyang (2021) Application of Deep Learning Architectures for Satellite Image Time Series Prediction: A Review. Remote Sens 13: 4822.

Palán L, Křeček J (2018) Interception and Fog Drip Estimates in Fragmented Mountain Forests. Environ Process 5: 727–742.

Pauli E, Cermak J, Andersen H (2022) Satellite-based climatology of fog and low stratus formation and dissipation times in central Europe. Q J R Meteorol Soc 148: 1439–1454.

Pauli E, Cermak J, Andersen H, Fuchs J (2024) An analysis of fog and low stratus life-cycle regimes over central Europe. Q J R Meteorol Soc 150B: 2382–2396.

Pérez-Díaz JL, Ivanov O, Peshev Z, Álvarez-Valenzuela MA, Valiente-Blanco I, Evgenieva T, Dreischuh T, Gueorguiev O, Todorov PV, Vaseashta A (2017) Fogs: Physical Basis, Characteristic Properties, and Impacts on the Environment and Human Health. Water 9: 807.

Seinfeld JH, Pandis SN (2006) Atmospheric Chemistry and Physics. John Wiley, New York.

Stamnes KH, Li H, Eide HA, Stamnes JJ (2005) Challenges in atmospheric correction of satellite imagery. Opt Eng 44: 041003.

Steeneveld GJ, Ronda RJ, Holtslag AAM (2015) The Challenge of Forecasting the Onset and Development of Radiation Fog Using Mesoscale Atmospheric Models. Bound-Lay Meteorol 154: 265–289.

Tambouratzis T, Tambouratzis G (2008) Meteorological data analysis using self-organizing maps. Int J Intell Syst 23: 735–759.

Thalmann E, Burkhard R, Wrzesinsky T, Eugster W, Klemm O (2002) Ion flux from fog and rain to an agricultural and a forest ecosystem in Europe. Atmos Res 64: 147–158.

Tolasz R, Miková T, Valeriánová A, Voženílek V (2007) Climate Atlas of Czechia. ČHMÚ, Praha.

Upadhyay AB, Shah SR, Thakkar RA (2024) Theoretical Assessment for Weather Nowcasting Using Deep Learning Methods. Arch Computat Methods Eng 31: 3891–3900.

van Oldenborgh GJ, Yiou P, Vautard R (2010) On the roles of circulation and aerosols in the decline of mist and dense fog in Europe over the last 30 years. Atmos Chem Phys 10: 4597–4609.

Vautard R, Yiou P, van Oldenbourgh GJ (2009) Decline of fog, mist and haze in Europe over the past 30 years. Nat Geosci 2: 115–119.

Walzelova K, Walzel S, Hovorka J (2025) Simultaneous multiple mobile PM_{10} monitoring enables high spatial and time localization of hot-spots in urban environment. Eur J Environ Sci 15:

Weathers KC, Ponette-Gonzáles AG, Dawson TE (2020) Medium, Vector, and Connector: Fog and the Maintenance of Ecosystems. Ecosystems 23: 217–229.

WMO ICA (International Cloud Atlas) (2017) https://cloudatlas.wmo.int/en/home.html. (Accessed on September 15, 2021).

Yao Z, Wang C, Jiang C (2025) Research on the fusion of FY4A satellite data and station observation data for heavy fog recognition. Theor Appl Climatol 156: 59.

Zimmermann L, Zimmermann F (2002) Fog deposition to Norway spruce stands at high-elevation sites in the Eastern Erzgebirge (Germany). J Hydrol 256: 166–175.

ENVIRONMENTAL RISKS OF HEAVY METAL POLLUTION IN WAR-AFFECTED SOILS IN UKRAINE

LIUDMYLA YASHCHENKO[1], OLEKSANDR ANDROSHCHUK[2], LIUDMYLA VASYLENKO[3] AND YULIYA CHORNOIVAN[4,*]

[1] National University of Water and Environmental Engineering, Soborna St. 11, Rivne, Ukraine
[2] Institute of Agriculture of Western Polissia of the National Academy of Agrarian Sciences of Ukraine, Rivne St. 5, Shubkiv vill., Rivne dist., Rivne region, Ukraine
[3] Head of the Association of innovative laboratories, Office 1, Building 4-M, Lukasha M. str., Lviv, Lviv region, Ukraine
[4] Deputy General Director of Prime Lab Tech LLC, 115-V, Kyivskyi Shliakh str., Velyka Oleksandrivka vill., Boryspil District, Kyiv Region, Ukraine
* Corresponding author: office@plt.land

ABSTRACT

This study examines soil contamination by heavy metals in Ukraine resulting from military activities, focusing on three regions: Chernihiv (ChD), Sumy (SmD) and Dnipropetrovsk (DnD). These regions have varying technogenic backgrounds, affecting contamination levels. The aim was to assess concentrations of heavy metals (Cd, Cr, Pb, Cu, Ni, Mn, Zn) in soils affected by military actions and evaluate the associated environmental risks. Soil samples were collected from areas directly affected by explosions and from locations 500 meters away. Concentrations of heavy metals were compared with maximum permissible concentrations (MPC) and local geochemical background levels. The Environmental Risk Index (RI) was used to assess the risk of heavy metal accumulation. Results showed significant increases in metal concentrations in war-affected areas, with several metals exceeding MPC. The highest concentrations were recorded at DnD, where lead reached 3.9 MPC, nickel 1.8 MPC, and manganese 1.4 MPC. High levels of Pb and Ni were recorded at SmD, whereas at ChD high levels were only recorded for Pb and Ni. The RI for DnD and SmD was high (RI 391-324), indicating higher contamination and medium risk at ChD(RI 222). The environmemental risks in regions with high technogenic backgrounds, such as DnD, are more severe. This study underscores the importance of a technogenic background in contamination risks and the need for continuous monitoring and risk management strategies to protect ecosystems and human health.

Keywords: anthropogenic load; bombardment; environmental risk; heavy metals; military activities; pollution

Introduction

The war in Ukraine has attracted considerable attention from the scientific community due to its profound implications for environmental security, stemming from the widespread destruction of natural resources, ecosystems and infrastructure (Duiunova et al. 2024; Kharytonov et al. 2024; Wirtu et al. 2025). Armed conflict has large-scale effects on the natural environment, with soils being one of the most vulnerable components of the ecosystem. The use of modern military equipment, explosives, and ammunition, alongside large-scale air strikes have resulted in significant destruction and long-term environmental pollution. Consequently, it has become necessary to identify a distinct category of soil degradation caused by armed aggression, among which chemical pollution stands out as the most prolonged and hazardous effect, which poses a severe threat to human life (Baliuk et al. 2022).

In addition to natural sources, scientists and researchers have identified industrialization and urbanization, as well as the intensification of agricultural production through the widespread use of pesticides and fertilizers, as major contributors to heavy-metal contamination (Abdullahi et al. 2021; Rashid et al. 2023; Xu et al. 2023). However, in the context of military aggression and intensive use of weapons, the problem of additional soil contamination with heavy metals in Ukraine has become particularly acute. War affects every natural object, and the resultant pollution has long-lasting negative transboundary effects. Violations caused by war indicate that crimes against the environment, humanity, and war crimes disrupt the international balance, leading to dissonance in global international environmental security, thereby jeopardizing the right to a safe environment for future generations (Kharytonov et al. 2024).

Military activities during warfare alter soil properties, including pH, cation composition and humus content, which results in elevated heavy metal concentrations. These metals, such as Pb, Cu, Zn, Cd, and Ni are toxic, bioaccumulative and persistent, and pose significant risks to ecosystems and human health. For instance, Pb contamination can poison plants, animals and humans through the food chain. Similarly, metals in explosives or ammunition can disrupt soil processes, reduce fertility, and cause long-term degradation. As a result, war-affected soils may become unsuitable for agriculture, worsening environmental and economic effects. Understanding the toxic elements in the soil and assessing their distribution is crucial for both environmental protection and restoring agricultural productivity in post-war recovery (Dehtiarev et al. 2023).

Military operations involve the extensive use of various types of ammunition, which are significant sources

Yashchenko, L., Androshchuk, O., Vasylenko, L., Chornoivan, Y.: Environmental risks of heavy metal pollution in war-affected soils in Ukraine
European Journal of Environmental Sciences, Vol. 15, No. 1, pp. 18–27
https://doi.org/10.14712/23361964.2025.3

of environmental pollution, particularly soil contamination. Modern ammunition comprises explosives, metal alloys and auxiliary materials that release a wide range of toxic substances during detonation. Most of these compounds are resistant to biodegradation or natural processing and thus persist in the biosphere and become long-term sources of pollution. These pollutants pose potential risks to human health and ecosystems because of their toxicity (Chaika and Korotkova 2023).

Gunpowder and explosives used in ammunition release chemical compounds that transform into gaseous and solid combustion products during detonation. While gases like nitrogen, carbon monoxide, and sulfur dioxide disperse into the atmosphere, most heavy particles settle on the soil. For example, detonating a 115 mm high-explosive projectile with hexogen produces up to 4,000 liters of gas, plus heavy metals. About 30% of these pollutants are released into the air, while the remainder accumulate in the soil and alter its chemical composition (Golubtsov et al. 2023). Greenhouse gas emissions are exacerbated by these activities (Pereira et al. 2022).

Metal compounds, such as lead (Pb), copper (Cu), cadmium (Cd), zinc (Zn) and manganese dioxide (MnO_2), are present in ammunition casings and are formed as by-products of explosive combustion (Makhovsky and Kriukovska 2015). Explosions also produce shrapnel, which scatters over hundreds of meters and gradually releases heavy metals as it decomposes in the soil. Lead and copper are among the primary compounds in ammunition (Greičiūtė et al. 2007), while zinc, often used to coat ammunition casings to prevent corrosion, and cadmium, chromium, and nickel, components of various alloys commonly occur in bombs (Yakymchuk et al. 2024).

The accumulation of these elements in the soil can exceed the natural background levels by tens or even hundreds of times, and the natural soil self-cleaning processes are extremely slow. These substances may decompose in the soil and migrate into groundwater, eventually entering food chains and affecting both humans and animals (Zaitsev et al. 2022).

Aerial bombs containing TNT, RDX, or other explosives release toxic metals like Ni and Cd, which are emitted during explosions. Fine particles containing these metals settle quickly on the ground, contributing to soil pollution. Once in the soil, these metals oxidize and enter environmental cycles, eventually reaching trophic chains. Contamination is further complicated by horizontal movement (via air transport) and vertical migration, influenced by ion diffusion, water flow, plant roots, soil fauna and human activity (Solokha et al. 2024).

This study aimed to evaluate the soil contamination caused by military operations in Ukraine, focusing on regions with varying industrial backgrounds. It specifically examines the concentrations of heavy metals in soils and compares them with maximum permissibles and geochemical background levels. Furthermore, this study assesses the potential environmental risks associated with heavy metal accumulation associated with the Russian military aggression in Ukraine. The findings will support the development of effective strategies to mitigate pollution and improve environmental conditions in affected regions.

Materials and Methods

For soil testing, sites were selected in areas directly affected by hostility, specifically where ammunition of various calibres had caused damage. Samples were collected from the impact zone and surrounding area in regions with varying initial anthropogenic loads: Chernihiv (51°59422″N 33°09458″E), location ChD, Sumy (50.86180″N 33.219175″E), location SmD, and Dnipropetrovsk (48°451465′N 35°176866′E), location DnD (Fig. 1). These locations were selected based on similar times for the bombardments (March–April 2023).

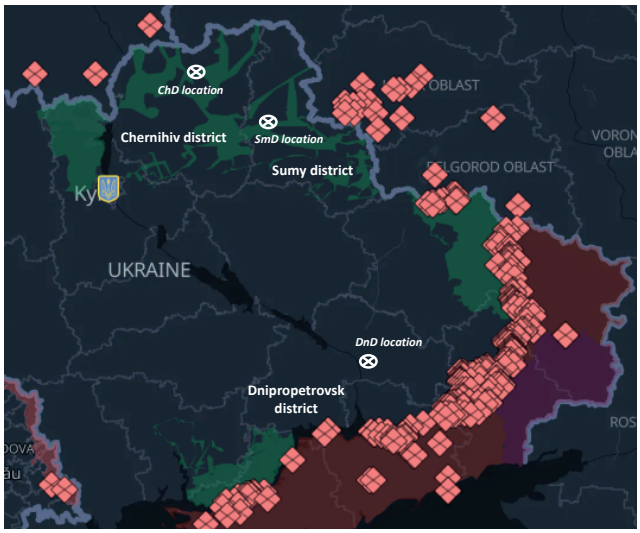

Fig. 1 Map of a Ukrainian conflict zone showing the locations of the sites where soil was sampled for analysis: Chernihiv (ChD), Sumy (SmD) and Dnipropetrovsk (DnD).

Soil sampling and analysis was carried out by the PRIME Lab Tech, LLC agrochemical laboratory (https://plt.land/uk), a facility specializing in high-precision soil analysis and expert recommendations for efficient land resource management. PRIME Lab Tech, LLC, is accredited under the DSTU EN ISO/IEC 17025:2019 standards (equivalent to EN ISO/IEC 17025:2017 and ISO/IEC 17025:2017, IDT) and holds the Accreditation Certificate No. 201741.

Two zones were identified around craters in order to characterize the effects of munitions on the soil.

1. Bombardment zone: the area directly affected by the explosion.
2. Contamination zone: the broader region influenced by weapon fragments and secondary pollutants (Bonchkovskyi et al. 2023).

In this study, soil samples collected from bombardment zones, that is, areas directly impacted by explosions, were designated as Ca (Fig. 2). For the contamination zone, the relationships between the aea of the bombard-

ment zone, crater diameter and weapon fragment range followed that described by Sydorenko and Azarov (2007) – Table 1. Based on this framework, the soil samples collected 500 m from the epicenter of the damage were classified as not directly affected by bombardment. These samples were presumed to contain heavy metals originating primarily from other sources, such as the anthropogenic background (Cf).

Table 1 Average diameter of the contamination zone of various explosive weapons.

Weapon calibre, mm	Average diameter of the contamination zone, m
82, 76, 85, 100	20
120, 122	30
152, 140, 160	50
203, 220, 240	70
Aerial bombs	100

Sampling involved averaging the soil from Ca and along the perimeter of a concentric circle at a radius of 500 m from Cf collected from the 0–10 cm soil layer (Fig. 2), in accordance with DSTU ISO 10381-2:2004 Soil Quality sampling. Part 2. Guidelines for Sampling Methods (ISO 10381-2:2002, IDT) (Splodytel, 2023). Pretreatment of the samples for physicochemical analysis followed the ISO 11464:2007 standard. Prior to analysis, the composite samples were air-dried and sieved through a 0.25 mm mesh.

The total heavy metal content (Cd, Mn, Cu, Ni, Pb, and Zn) was determined after soil digestion using a mixture of acids (aqua regia) and dissolution of the residue in nitric acid, according to DSTU ISO 11466-2001 (equivalent to ISO 11466:1995 Soil Quality; Extraction of Trace Elements Soluble in Aqua Regia). The heavy metal concentrations were measured using inductively coupled plasma atomic emission spectrophotometry (ICPAES).

To evaluate the soil conditions, including the technogenic background and heavy metal content, in samples taken 500 m from Cf, the results were compared with the geochemical background values (Cgf) from the statistical parameters of heavy metal content in agricultural soils (Klos et al. 2012). The coefficient of the technogenic load (Kt), which is the heavy metal excess over the geochemical background, was calculated as follows (Equation 1):

$$Kt = \frac{Cf}{Cgf}, \quad (1)$$

where: Kt – the coefficient of the technogenic load, which is the extent of the excess of heavy metals over the geochemical background.
Cf – the technogenic background, which is the heavy metal content in soil samples 500 from the epicenter of an impact.
Cgf – the geochemical background value, which is the heavy metal content in agricultural soils.

To determine the accumulation of heavy metals resulting from military operations (Cw), the concentration

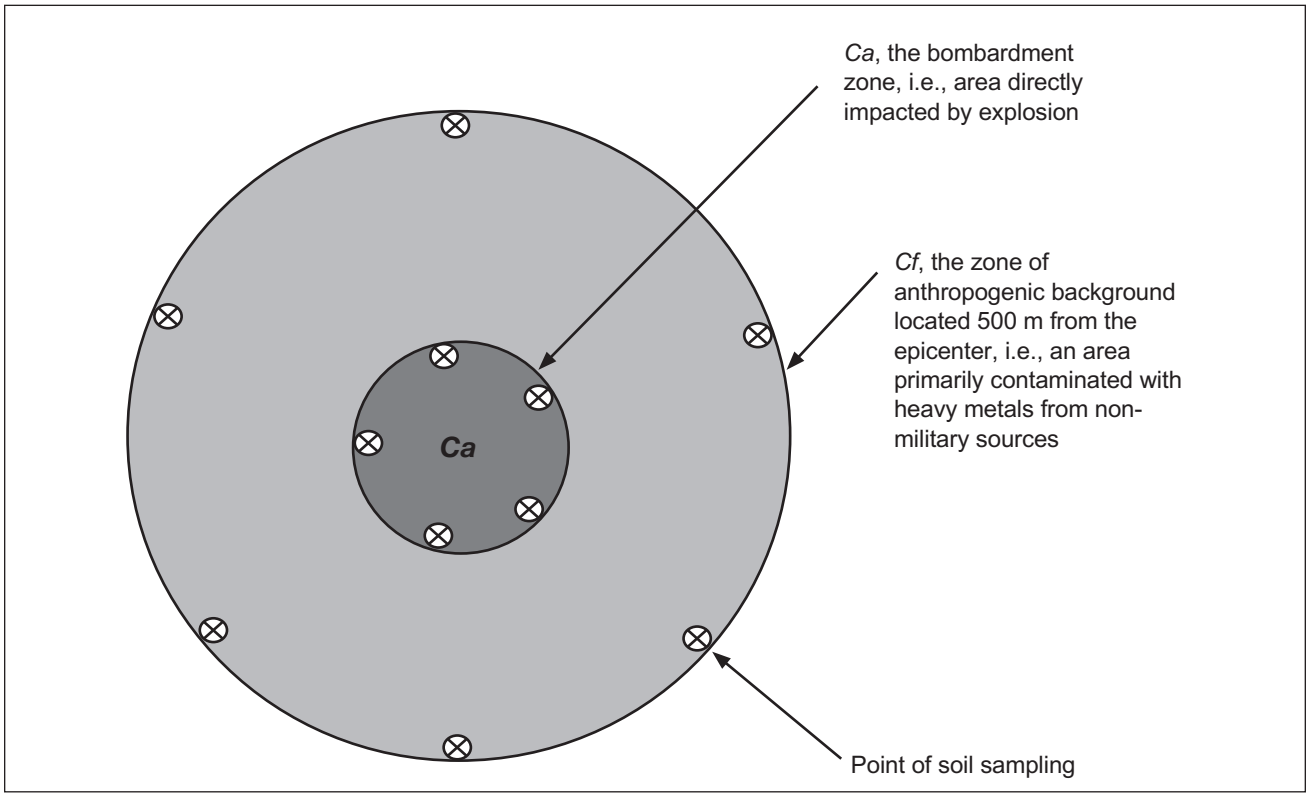

Fig. 2 Diagram of soil sampling design in a bombardment zone, which illustrates the spatial distribution of where soil was sampled within a contaminated area. The bombardment zone (Ca) is the area directly affected by the explosion, whereas the anthropogenic background zone (Cf) is the area 500 m from the epicenter, primarily containing heavy metals from nonmilitary sources. Soil samples were collected at the locations indicated for analysis.

at the impact point (Ca) was compared with the technogenic background (Cf) using Equation (2):

$$Cw = Ca - Cf, \quad (2)$$

where: Cw – the elemental content attributable to bombardment, mg/kg of soil.
Ca – the element concentration at the impact point, mg/kg of soil.
Cf – the technogenic background concentration, mg/kg of soil.

To assess the degree of soil enrichment with heavy metals due to bombardment, the concentration coefficient (Kc) was calculated, which is the ratio of the heavy metal content introduced during bombardment (Cw) to the technogenic background (Cf), as follows (Equation 3):

$$Kc = Cw - Cf, \quad (3)$$

where: Kc – the coefficient of soil enrichment with heavy metals.

The degree of soil enrichment with heavy metals (Kc) was assigned to one of four levels (Hakanson 1980; Malovanyy et al. 2024):

Kc < 1, no enrichment.
1 ≤ Kc ≤ 3: Moderate pollution.
3 ≤ Kc ≤ 6: Significant contamination.
Kc > 6: Very high pollution.

Calculations of the technogenic load (Kt), heavy metal accumulation due to bombardment (Cw) and the degree of soil enrichment (Kc) are critical for identifying the extent of environmental degradation in war-affected regions. These metrics provide essential data for prioritizing areas that require immediate remediation and support for informed decision making in environmental recovery efforts. Moreover, understanding heavy metal contamination levels helps assess the feasibility of restoring agricultural productivity in affected soils, ensuring food safety, and sustainable land use in the post-war period.

The potential risk index for each heavy metal was calculated, as follows (Equation 4).

$$E_r^i = T_r^i \times K_c^i, \quad (4)$$

where: K_c^i – the degree of metal enrichment as a result of bombardment.
T_r^i – the toxic reaction coefficient assigned to each heavy metal: Cd = 30, Pb = Ni = Cu = 5, Cr = 2, Zn, and Mn = 1 (Xu et al. 2008).

The integral value of the potential environmental risk (RI) was calculated as the sum of the potential risk indices for all heavy metals, as follows (Equation 5):

$$RI = \sum_{i=1}^{n} E_r^i \quad (5)$$

here E_r^i – is the potential risk index for each heavy metal.

The indices of potential risk for each element and integral potential risk for the environment are listed in Table 2 (Ma et al. 2024).

Table 2 Classification of criteria for the potential environmental risk of heavy metals in soil.

E_r^i	Potential environmental risk index of the elements	RI	Integral potential environmental risk
$E_r^i < 40$	Low	RI < 150	Low
$40 \le E_r^i < 80$	Average	< 300	Average
$80 \le E_r^i < 160$	High	< 600	High
$160 \le E_r^i < 320$	Very high	< 1200	Very high
$E_r^i < 320$	Extra high	RI > 1200	Extra high

Results

Background indicators of heavy metal content in soils

Heavy metal sources are classified as natural or anthropogenic. Geogenic sources include sedimentary rocks, volcanic eruptions, soil formations and rock weathering. Anthropogenic sources, which can cause local and global heavy metal anomalies, include industrial production, agriculture, wastewater and vehicle exhaust. These sources significantly elevate heavy metal concentrations and contribute to ecosystem pollution (Alengebawy et al. 2021).

Therefore, depending on the location of an area studied and its industrial and economic loads, the indicators of heavy metal content outside the immediate impact zone (i.e., at distances greater than 500 m from the bombardment epicenter) differ significantly (Table 3).

Table 3 Total heavy metal content in soil samples taken 500 m from the point of impact (technogenic background, Cf).

Location	Heavy metals, mg/kg of soil						
	Cd	Cr	Pb	Cu	Ni	Mn	Zn
ChD	0.25	16.4	16.5	13.2	8.2	161	38.6
DnD	0.58	45.6	22.4	24.9	29.5	1398	102.5
SmD	0.31	29.6	17.4	16.3	10.3	324.1	51.3
Clarke, Ukraine average (Cgf) [15]	0.17	74.7	17.3	14.5	26.1	628.3	53.0

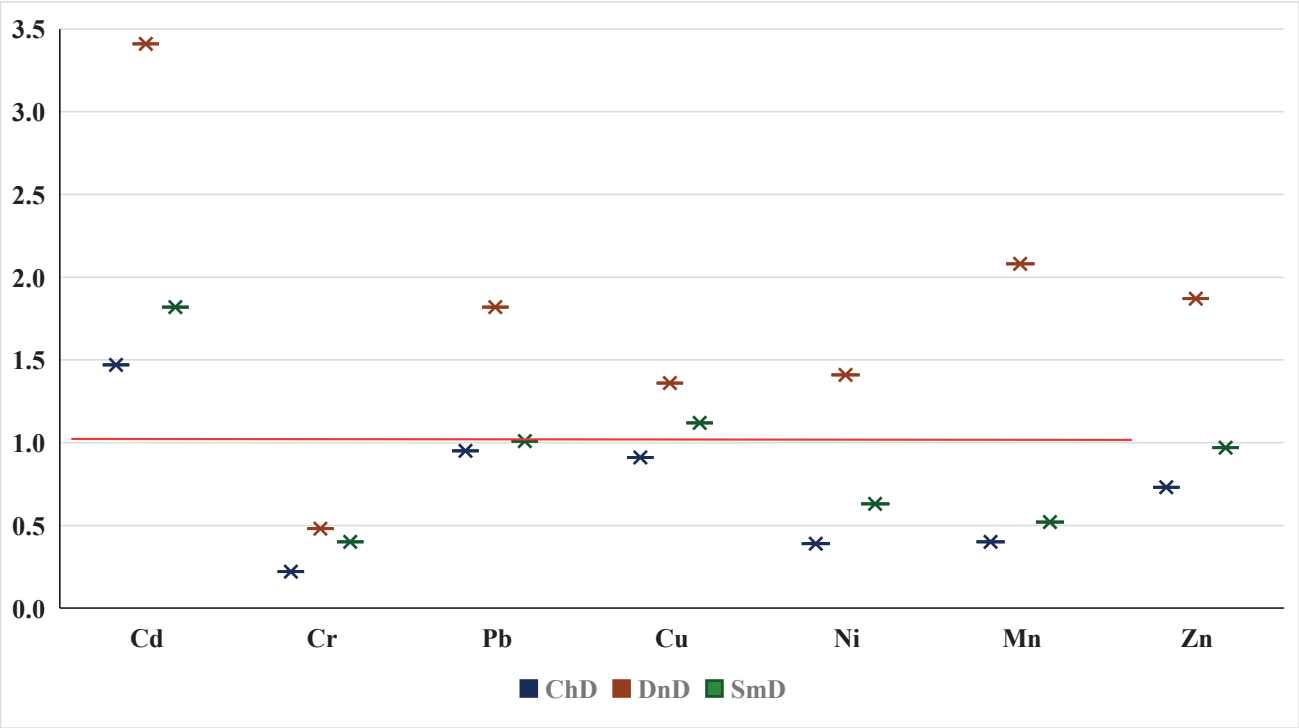

Fig. 3 Extent of the excess (Kt) of heavy metal in soil samples collected 500 m from the point of impact (Cf) relative to the average geochemical background in Ukraine (Cgf). The red line indicates the threshold corresponding to the geological background value (Clarke's average for Ukraine) and marks the limit beyond which the heavy metal concentrations exceeded natural background levels (Cgf).

The lowest accumulation of heavy metals was recorded in soil samples collected from areas furthest from large industrial cities (ChD). In contrast, the highest levels, compared to the average geochemical background in Ukraine, were recorded in soil samples from DnD (Fig. 3).

The technogenic load coefficient (Kt) is an important indicator that reflects the leaching (Kt < 1) or accumulation (Kt > 1) of chemical elements in soil. The heavy metal content in the soil samples from various locations relative to the geochemical background (Cgf) was categorised by their Kt values. At DnD the Kt values for heavy metals exceeded the geochemical background (Clarke's average for Ukraine) for nearly all elements, except chromium, indicating a significant anthropogenic influence in this area. The values for cadmium were 3.4 times higher than the geochemical background, for manganese 2.2 times higher, for copper 1.7 times higher, for nickel 1.1 times higher, for lead 1.3 times higher and for zinc 1.9 times higher than the average geochemical levels. This pattern suggests that heavy metal contamination at DnD is largely due to industrial activities, which are more extensive in this region than in other areas.

Elevated heavy metal concentrations at DnD are largely due to industrialization, with emissions, wastewater discharge and other anthropogenic activities contributing to soil contamination. These processes result in metal concentrations exceeding natural geochemical backgrounds, which indicate the significant effect of human activity. In contrast, at ChD and SmD, cadmium accumulation (Kt 1.5–1.8) and near-threshold levels of copper (Kt 0.91–1.1) and lead (Kt 0.9–1.0) are primarily linked to agriculture, where intensive use of pesticides and fertilizers has led to contamination of both soil and water, potentially exceeding acceptable limits (Defarge et al. 2018; Suciu et al. 2022).

Heavy metal content in soils in the bombardment zone

As noted by Certini et al. (2013), areas of intense military conflict, particularly those marked by the deployment of explosives and munitions, are recognized as significant sources of terrestrial ecosystem contamination during periods of armed conflict. The physical, chemical, and biological properties of soil are compromised by gunfire and explosion. This phenomenon is especially detrimental in agricultural regions, as it negatively affects soil productivity and leads to contamination of the soil-plant-human chain (Lima et al. 2011).

Changes in the chemical composition and content of total heavy metal compounds (Cd, Cr, Pb, Cu, Ni, Mn, Zn) were monitored during military intervention (Ca) in different regions of Ukraine, as summarized in Table 4.

In absolute terms, the soil in the crater at DnD contained higher concentrations of all the monitored elements than that recorded in other regions. However, it should be emphasized that not all exceed the maximum allowable concentration based on background levels (Clarke's average). According to DSTU 4362:2004, Soil Quality. Soil Fertility Indicators," the content of heavy metals should not exceed Clarke's average or 0.5 MPC (maximum permissible concentration).

Table 4 Total content of heavy metal compounds in soil samples from different impact points (Ca).

Location	Heavy metals, mg/kg of soil						
	Cd	Cr	Pb	Cu	Ni	Mn	Zn
ChD	0.98	34.6	64.1	51.9	38.4	887	154.9
DnD	1.68	84.2	123.5	92.5	91.8	2108	226.3
SmD	1.42	59.2	101.6	74.2	59.6	1254	182.3

An analysis of the heavy metals at impacts revealed that the contents of cadmium and chromium at ChD were approximately 0.3 MPC, whereas copper and zinc concentrations were close to background levels, with both at 0.5 MPC. Manganese concentrations were 0.6 MPC, nickel 0.8 MPC, and lead 2.0 MPC (Fig. 4). Cu and Zn are trace elements that do not exceed maximum allowable concentrations. Given the low soil supply of these compounds in the region, no significant exceeding of the acceptable concentrations were detected.

The soil samples from SmD had intermediate levels of contamination in terms of exceeding MPC. The highest excess values were recorded for Pb (3.2 MPC) and Ni (1.2 MPC). The excess of other elements ranges from 0.5 to 0.8 MPC, indicating soil contamination.

The most environmentally concerning situation, in terms of heavy metal content, was recorded at DnD. Here, the excess for lead is 3.2 MPC, nickel 1.8 MPC, manganese 1.4 MPC, with other elements exceeding the background levels by 0.6 to 0.9 MPC. Such high contamination with specific elements is attributed to their accumulation from the explosions of munitions (Zaitsev et al. 2022; Solokha et al. 2023) and the initial technogenic load in the region.

Accumulation of heavy metals as a result of bombardment

Consideration of the aforementioned levels of the technogenic background of heavy metal content (Cf), indicates that military operations and bombardments resulted in a more intense accumulation of certain elements (Table 4). The use of explosive weapons during combat leads to the accumulation of hazardous amounts of lead (1.5–2.9 MPC) and nickel (0.6–1.1 MPC) in the soil (Cw), regardless of the region (Fig. 5). In addition, at SmD and DnD, the excess is 0.6–0.7 MPC for copper, 0.5–0.6 MPC for manganese and 0.5 MPC for chromium at DnD. No exceeding of the maximum permissible concentrations (MPC) was detected at ChD, except for Pb and Ni. The amounts of Cd and Zn in the soils at all the sites did not exceed the MPC values.

The varying degrees of accumulation of these elements may be attributed to both the characteristics of the soil and the processes by which they interact with heavy metals as well as the different sources of their introduction into the soil from military equipment. War-related chemical contamination depends on the intensity and duration of hostilities, the types of weapons used, and the extent of bombardment. The accumulation coefficient of each element relative to the natural or anthropogenic

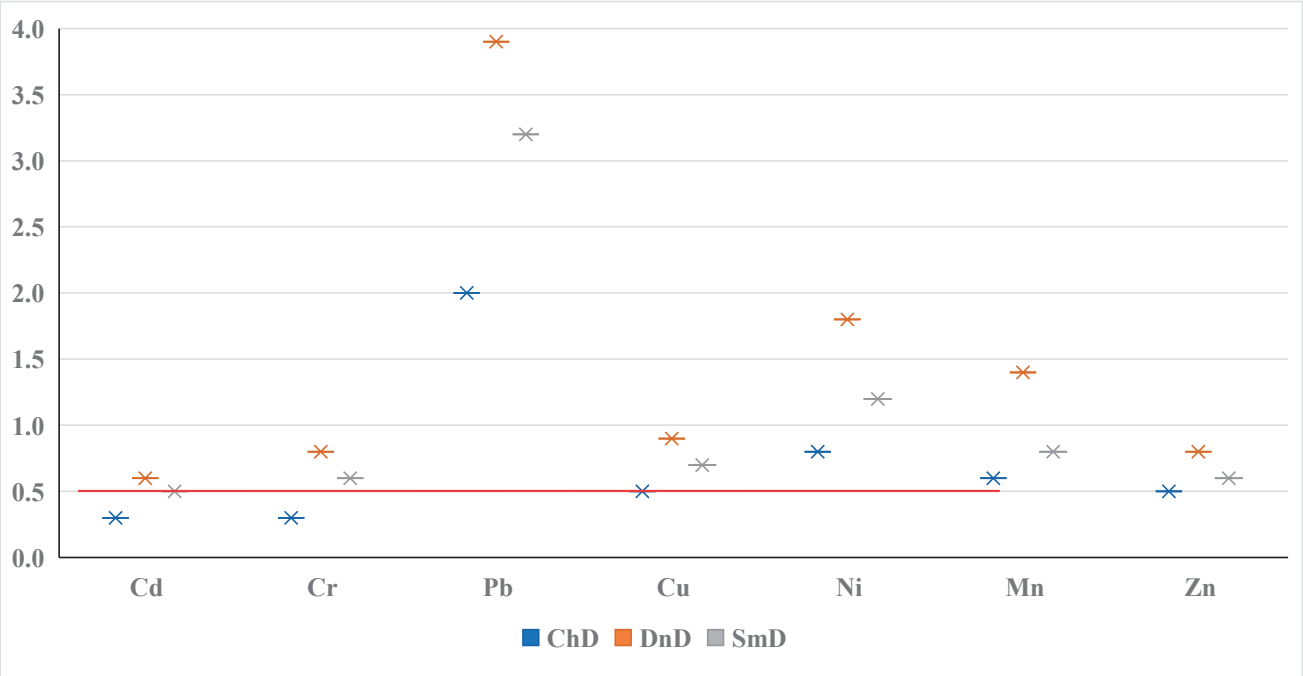

Fig. 4 Extent of the excess of heavy metals in soil samples collected from points of impact (Ca) relative to the corresponding maximum permissible concentrations (MPC). The red line is the threshold of the maximum permissible concentration (MPC).

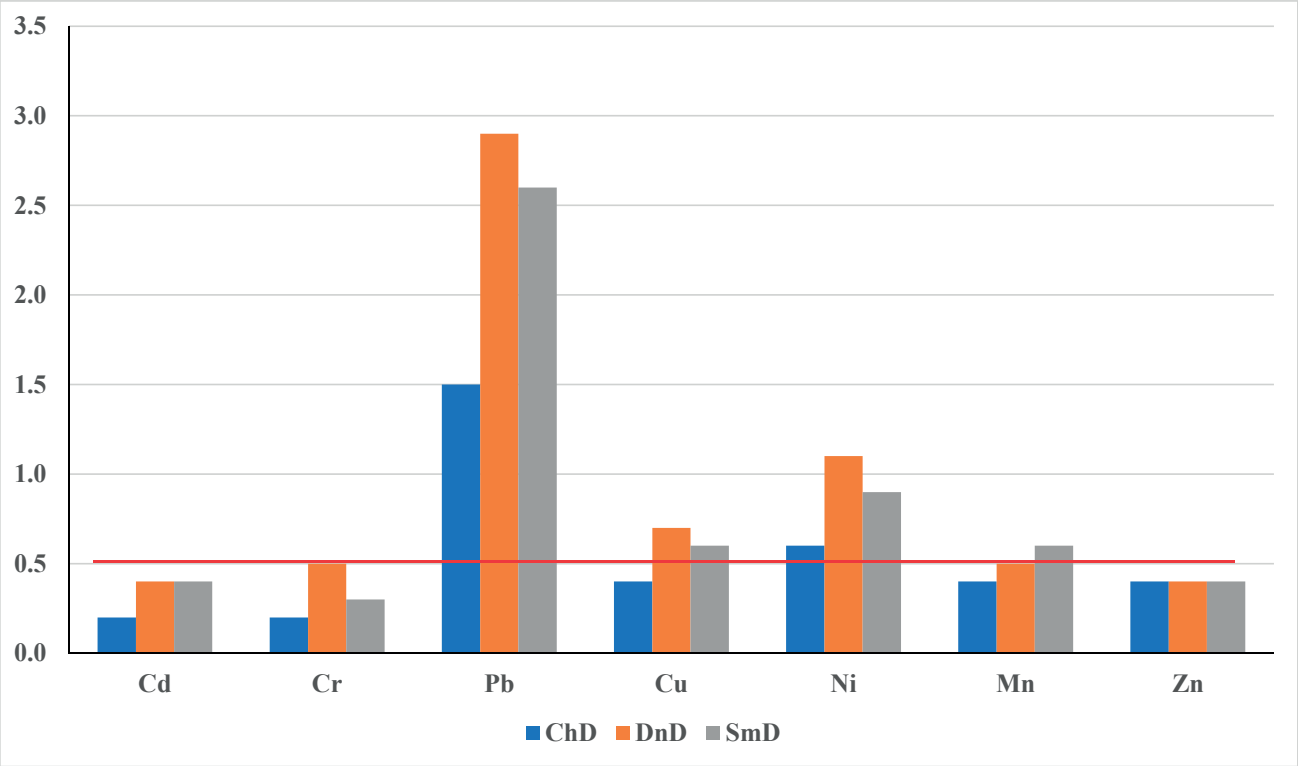

Fig. 5 Extent of the excess of heavy metals in samples collected at points of impact (Ca) relative to the corresponding maximum permissible concentration (MPC) indicators. The red line is the threshold of the acceptable maximum permissible concentration (MPC).

background (Clarke's average) provides a clearer understanding of levels of contamination and shifts in ecological balance (Fig. 6).

The amount of lead resulting from the bombardment was determined to between 2.9–4.8 (Clarke's average). The largest accumulation was recorded at SmD, where the predominant accumulation was for Cd (3.6 Clarke's average) and Mn (2.9 Clarke's average). The accumulation of Cu at SmD and DnD was almost equal (3.6–3.7 Clarke's average, respectively).

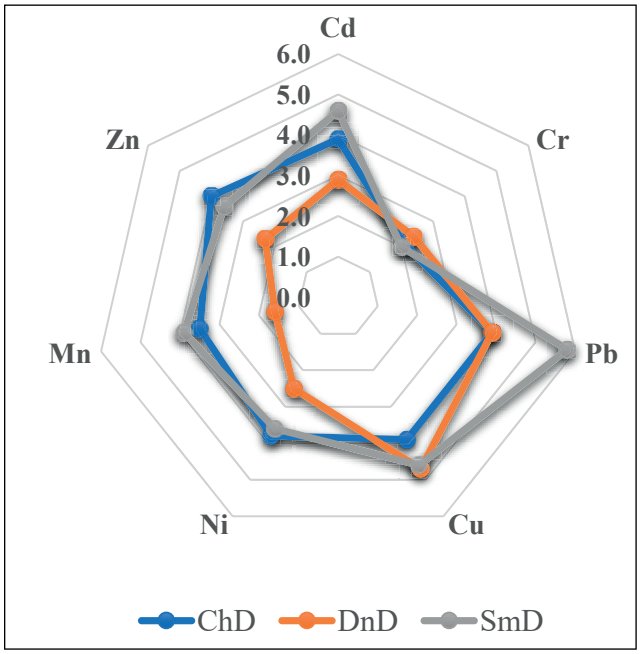

Fig. 6 Coefficient of heavy metal accumulation in soils (Kc) collected from points of impact (Ca) due to bombardment, relative to the anthropogenic background (Cf).

Discussion

Human activity and urbanization have introduced many foreign substances into ecosystems, particularly heavy metals. These elements are strongly absorbed by soil, forming insoluble compounds with phosphates and hydroxides, resulting in their gradual accumulation (Kozlyk et al. 2023). In industrial areas, heavy metals such as Cd, Pb, Cu, Cr, Zn, and Ni often exceed background concentrations. These metals are highly toxic, pose risks for soil, groundwater, and plants, and affect the ecological state of these areas (Kroik 2011; Tarasenko 2013; Chorna et al. 2018).

In the present study, the soil at DnD was distinct from that at the other sites because of its elevated anthropogenic background (Cf). The anthropogenic load coefficient (Kt) for various elements ranged from 0.48 to 3.41, when compared to the average background indicators in Ukraine (Klos et al. 2012). These data indicate that industrial centers are significant sources of heavy metal pollution. Studies by Sutkowska et al. (2020) and others similarly report that heavy metal concentrations in soils in mining areas significantly exceed the geochemical background levels.

Military actions during the full-scale invasion of Ukraine have caused not only the physical degradation of soil but also its chemical contamination. Impacts of

shells, burning of military equipment and release of oil destroy ecosystems and contribute to soil and water pollution by heavy metals and toxic elements.

The soil from DnD, which is from outside impact zones, was the most heavily contaminated (Table 3). Relative to the established anthropogenic background (Cf), explosions of shells of various calibres result in the accumulation of heavy metals in soil (Cw), including Pb (2.9 Clarke), Cd (1.9 Clarke), Cr (1.3–1.5 Clarke), Ni (1.3–1.5 Clarke), Zn (1.3–1.5 Clarke), and Mn (0.6 Clarke) – Fig. 5. At locations with the lowest anthropogenic backgrounds, heavy metal accumulation due to bombardment significantly exceeded established background levels (Clarke). For example, the accumulation coefficient for zinc is 3.0 Clarke, for manganese 2.5 Clarke, and for nickel, cadmium, lead 2.8–2.9 Clarke, indicating a deterioration in the environmental as a result of surface craters caused by explosions. Other sources note that the concentrations of metals in the soils of different regions in Ukraine have far exceeded the permissible limits and pose a significant threat to the ecological stability of these ecosystems (Drobitko and Alakbarov 2023). They also report that heavy metals and toxins that accumulate during crop production contribute to contamination (Gamajunova et al. 2021; Sytar and Taran 2022). Large-scale remote sensing data from 2021 and 2022 (Eastern and Southeastern Ukraine) revealed a significant decrease in cultivation in regions with intense fighting (Luhansk and Donetsk) (Solokha et al. 2023). Therefore, the environmental consequences of the war were compounded by an economic crisis. Since the Russian invasion of Ukraine, the price of agricultural products has surpassed that of the food crisis a decade ago (Glauben et al. 2022).

Human exposure to pollutants including heavy metals can have irreversible consequences. The majority of these compounds are resistant to biodegradation or treatment and thus remain in the biosphere for extended periods. They are potentially harmful for both human health and the environment due to their toxicity (Broomandi et al. 2020).

The assessment of heavy metal accumulation resulting solely from bombardment revealed that, based on the degree of heavy metal accumulation (Hakanson 1980; Malovanyy et al. 2024) contamination at ChD can be classified as moderate by all criteria ($1 \leq Kc \leq 3$) whereas at DnD it was moderate for all elements except Cu, for which contamination was considered significant ($3 \leq Kc \leq 6$). At SmD contamination was moderate for Cr, Ni, Mn, and Zn ($1 \leq Kc \leq 3$), and significant for Cd, Pb, and Cu ($3 \leq Kc \leq 6$). Based on Equation 4, the potential environmental risk index of heavy metal accumulation due to bombardment is medium to high (56.9-107.4) for cadmium, and for the other elements it is low (<40).

Because the integral potential environmental risk of heavy metal accumulation does not only consider the heavy metal content in the soil but also the environmental and ecological effects of heavy metals on toxicology, it is important to calculate the RI value (Equation 5) for the total heavy metal content in the soil at the point of impact (Ca) taking into consideration the geochemical background level (Cgf).

Calculations revealed that depending on the general anthropogenic background in the area and the effect of contamination due to bombardment, the degree of potential environmental risk is medium for ChD and high for DnD and SmD (Table 5).

Table 5 The environmental risk index (RI) for heavy metal accumulation in soils at the locations studied.

Location	RI	Level limits	Degree of Integral potential environmental risk
ChD	222	150 ≤ RI < 300	average
DnD	391	300 ≤ RI < 600	high
SmD	324		

Conclusions

This study reveals the environmental and health risks of heavy metal contamination in Ukrainian soils due to military activity. Industrial regions like Dnipropetrovsk, are highly contaminated with mainly Pb, Ni and Mn. The environmental risk index (RI) for Dnipropetrovsk and Sumy regions was high (RI 391-324), indicating significant contamination levels, whereas for Chernihiv it was medium (RI 222). This indictes that industrial areas, particularly Dnipropetrovsk, face great risks of heavy metal accumulation being increased by conflict. This research highlights the long-term ecological and health threats posed by metals like Pb, Cd, Ni and Mn, and need for urgent action, including monitoring, soil remediation and public health measures. This study further emphasizes the need to address high contamination levels in regions where it is likely to damage the ecology and prevent further environmental degradation and risk to human health.

Funding Statement

Our research was supported the grant from The Science for Peace and Security Programme (SPS) – G6296 "Improving the Monitoring of the State of Agricultural Land Affected by Military Operations."

REFERENCES

Abdullahi A, Lawal M, Salisu A (2021) Heavy metals in contaminated soil: source, accumulation, health risk and remediation process. BAJOPAS 14: 1–12.

Alengebawy A, Abdelkhalek ST, Qureshi SR, Wang M-Q (2021) Heavy metals and pesticides toxicity in agricultural soil and plants: ecological risks and human health implications. Toxics 9: 42.

Baliuk S, Kucher A, Solokha O, Solovei B, Smirnova B, Momot F, Levin Ya (2022) Impact of armed aggression and hostilities on the current state of the soil cover assessment of damage and losses restoration measures. Kharkiv. doi: 10.13140/RG.2.2.15740.41608.

Bonchkovskyi O, Ostapenko P, Shvaiko V, Bonchkovskyi A, Shvaiko V (2023) Remote sensing as a key tool for assessing war-induced damage to soil cover in Ukraine (the case study of Kyinska territorial hromada). Journ Geol Geograph Geoecol 32: 474–487. doi: 10.15421/112342.

Broomandi P, Guney M, Kim JR, Karaca F (2020) Soil contamination in areas impacted by military activities: a critical review. Sustain 12: 9002. doi: 10.3390/su12219002.

Certini G, Scalenghe R, Woods WI (2013) The impact of warfare on the soil environment. Earth-Sci Rev 127: 1–15. doi: 10.1016/j.earscirev.2013.08.009.

Chaika T, Korotkova I (2023) Restoration of soil fertility in Ukraine after hostilities. In: Chaika TO (ed) Protection and restoration of ecological balance and ensuring self-renewal of ecosystems: collective monograph. Poltava: Astraya PE Publishing House, pp 232–281.

Chorna VI, Voroshylova NV, Syrovatko VA (2018) Distribution of cadmium in the soils of the Dnipropetrovsk region and its accumulation in crop production. Ukr J Ecol 8: 910–917. doi: 10.15421/2018_293.

Defarge N, DeVendômois JS, Séralini GE (2018) Toxicity of formulants and heavy metals in glyphosate-based herbicides and other pesticides. Toxicol Rep 5: 156–163. doi: 10.1016/j.toxrep.2017.12.025.

Dehtiarev VV, Konshyn RV, Lytvynov VA (2023) Military operations impact on soil cover degradation processes. In: Soil cover of Ukraine in the conditions of hostilities: State, challenges, activities for soil restoration: Collection of abstracts of the International Scientific and Practical Conference (Kharkiv, December 5, 2023) [Electronic edition]. Kharkiv: NSC "Institute for Soil Science and Agrochemistry Research named after O. N. Sokolovsky".

Drobitko A, Alakbarov A (2023) Soil restoration after mine clearance. Intern J Environ Sci Stud 80: 394–398. doi: 10.1080/00207233.2023.2177416.

Duiunova T, Voznyk M, Koretskyi S, Chernetska O, Shylinhov V (2024) International humanitarian law and ecocide: the war in Ukraine as a case study. Eur J Environ Sci 14: 14–23. doi: 10.14712/23361964.2024.2.

Gamajunova V, Panfilova A, Kovalenko O, Khonenko L, Baklanova T, Sydiakina O (2021) Better management of soil fertility in the southern steppe zone of Ukraine. In: Soils under stress: More work for soil science in Ukraine Cham. Springer, pp 163–171. doi: 10.1007/978-3-030-68394-8_16.

Glauben T, Svanidze M, Götz LJ, Prehn S, Jaghdani TJ, Djuric I, Kuhn L (2022) The war in Ukraine exposes supply tensions on global agricultural markets: Openness to global trade is needed to cope with the crisis. IAMO Policy Brief 44. Retrieved from: https://hdl.handle.net/10419/253702.

Golubtsov O, Sorokina L, Splodytel A, Chumachenko S (2023) Russia's war against Ukraine impact on the state of Ukrainian soils. Analysis results Kyiv CS Center for Environmental Initiatives "Ecodiya".

Greičiūtė K, Juozulynas A, Šurkienė G, Valeikienė V (2007) Research on soil disturbance and pollution with heavy metals in military grounds. Geologija – Vilnius 57: 14–20. Retrieved from: https://etalpykla.vilniustech.lt/handle/123456789/150116.

Hakanson L (1980) An ecological risk index for aquatic pollution control a sedimentological approach. Water Res 14: 975–1001. doi: 10.1016/0043-1354(80)90143-8.

Kharytonov S, Orlovskyi R, Us O, Iashchenko A, Maslova O (2024) Criminal responsibility for ecocide resulting from the military aggression of Russia. Eur J Environ Sci 14: 24–32. doi: 10.14712/23361964.2024.3.

Klos VR, Birke M, Zhovinsky EY, Akinfiev GO, Amayiukeli YuA, Klamens R (2012) Regional geochemical studies of soils of Ukraine in the framework of the international project on geochemical mapping of agricultural and pasture lands in Europe (GEMAS). Prospect Environ Geochem 1: 51–66. Retrieved from: http://nbuv.gov.ua/UJRN/Pteg_2012_1_9.

Kozlyk TI, Drozd BE, Romanchuk LM (2023) Ecological and agrochemical consequences of a missile hit. In: Materials of the International Scientific and Practical Conference "Environmental measurement Realities of the impact of armed aggression on the soil cover of Ukraine" Kyiv, pp 20–23.

Kroik AA (2011) Toxicological aspects of accumulation and distribution of heavy metals in industrial agglomerations' soils. Proceedings of the VI International Scientific Conference. Dnepropetrovsk DNU publishing house, pp 15–18.

Lima D, Bezerra M, Neves E, Moreira F (2011) Impact of ammunition and military explosives on human health and the environment. Rev Environ Health 26: 101–110. doi: 10.1515/reveh.2011.014.

Ma Y, Meilan W, Liu P, Jiang Y, Zhang X (2024) Speciation Characteristics and Risk Assessment of Heavy Metals in Cultivated Soil in Pingshui Village Zhaoping County Hezhou City Guangxi. Appl. Sci 14: 11361. doi: 10.3390/app142311361.

Makhovsky VO, Kriukovska OA (2015) Investigation of hazards and assessment of the consequences of emergencies and accidents in bulk flour storage warehouses of bakery enterprises. In: Collection of scientific papers of Dniprodzerzhynsk State Technical University Technical sciences 1: 288–295.

Malovanyy MS, Petrushka K, Skrzypczak D, Chojnacka K, Warchoł J (2024) Risks of soil pollution with toxic elements during military actions in Lviv. J Ecolog Engin 25. doi: 10.12911/22998993/175136.

Pereira P, Bašić F, Bogunovic I, Barcelo D (2022) Russian-Ukrainian war impacts the total environment. Sci Total Environ 837: 155865. doi: 10.1016/j.scitotenv.2022.155865.

Rashid A, Schutte BJ, Ulery A, Deyholos MK, Sanogo S, Lehnhoff EA, Beck L (2023) Heavy metal contamination in agricultural soil: environmental pollutants affecting crop health. Agron 13: 1521. doi: 10.3390/agronomy13061521.

Solokha M, Demyanyuk O, Symochko L, Mazur S, Vynokurova N, Sementsova K, Mariychuk R (2024) Soil degradation and contamination due to armed conflict in Ukraine. Land 13: 1614. doi: 10.3390/land13101614.

Solokha M, Pereira P, Symochko L, Vynokurova N, Demyanyuk O, Sementsova K, Inacio M, Barcelo D (2023) Russian-Ukrainian war impacts on the environment. Evidence from the field on soil properties and remote sensing. Sci Total Environ 1 902: 166122. doi: 10.1016/j.scitotenv.2023.166122.

Suciu NA, De Vivo R, Rizzati N, Capri E (2022) Cd content in phosphate fertilizer: which potential risk for the environment and human health? Curr Opin in Env Sci Hl 30: 100392. doi: 10.1016/j.coesh.2022.100392.

Sutkowska K, Teper L, Czech T, Hulok T, Olszak M, Zogala J (2020) Quality of Peri-Urban soil developed from Ore-Bearing carbonates: heavy metal levels and source apportionment assessed using pollution indices. Minerals 10: 1140. doi: 10.3390/min10121140.

Sydorenko VL, Azarov SI (2007) Assessment of damage in military units in the event of accident at ammunition depot. Collection of scientific papers of Kharkiv Air Force University 3: 151–156.

Sytar O, Taran N (2022) Effect of heavy metals on soil and crop pollution in Ukraine – a review. J Cent Eur Agric 23: 881–887. doi: 10.5513/JCEA01/23.4.3603.

Tarasenko LO (2013) Heavy metal content in soils of various regions and zones of southern Ukraine and their phytotoxicity. Scientific Bulletin of the Lviv National University of Veterinary Medicine and Biotechnology named after S. Z. Gzhytsky 15: 221–224.

Wirtu YD, Abdela U (2025). Impact of war on the environment: ecocide. Front Environ Sci 13: 1539520. doi: 10.3389/fenvs.2025.1539520.

Xu J, Li Y, Wang S, Long S, Wu Y, Chen Z (2023) Sources, transfers and the fate of heavy metals in soil-wheat systems: The case of lead (Pb)/zinc (Zn) smelting region. J Hazard Mater 441: 129863. doi: 10.1016/j.jhazmat.2022.129863.

Xu ZQ, Ni S, Tuo XG, Zhang CJ (2008) Calculation of heavy metal's toxicity coefficient in the evaluation of Potential Ecological Risk Index. Environ Sci Tech 31: 112–115.

Yakymchuk A, Balanda O, Bzowska-Bakalarz M (2024) Assessment of soil contamination of Ukraine with heavy metals during the war. Sci J Sil Univ Technol 196. doi: 10.29119/1641-3466.2024.196.45.

Zaitsev YuO, Gryshchenko OM, Romanova SA, Zaitseva IO (2022) Military operations impact on the content of total forms of heavy metals in the soils of Sumy and Akhtyrsky districts of Sumy region. Agroecolog J 3: 136–149. doi: 10.33730/2077-4893.32022.266419.

SUNNING CLUSTERS OF ANTS CONTRIBUTE SIGNIFICANTLY, BUT WEAKLY TO SPRING HEATING IN THE NESTS OF THE RED WOOD ANTS, *FORMICA POLYCTENA*

PETER CHANAS[1] AND JAN FROUZ[1,2,*]

[1] Institute for Environmental Studies, Faculty of Science, Charles University, Benátská 2, 128 01 Prague 2, Czech Republic
[2] Institute of Soil Biology and Biogeochemistry, Biology Centre CAS, Na Sádkách 7, 370 05 České Budějovice, Czech Republic
* Corresponding author: jan.frouz@natur.cuni.cz

ABSTRACT

Red wood ants perform sun-basking behavior in the spring. This very conspicuous behaviour consists from densely packed bodies of ants, forming sunning clusters, which expose themselves to sun radiation. This led to rapid increase in ant body temperature. The expectation was that the ants so heated that return to the nest may bring heat from outside, which heats the nest. Although this was postulated a long time ago, the effect of sun-basking behaviour on nest heating has not been tested. Filling this gap is the subject of this study. To do this the presence of sunning clusters on 10 *Formica polyctena* nests was recorded using camera-traps, which recorded presence of sunning clusters on the nest surface daily from March 10 to June 3, 2016 in the south of the Czech Republic. Camera traps also recorded external air temperature. At the same time, internal nest temperatures were measured by thermometers located inside the nests, which continually recorded nest temperature over the same period. Comparison of consecutive days without and with sunning clusters of ants revealed an increase in internal nest temperature occurred when clustering was recorded. This, however, was only recorded for nests in which the temperature did not go above 20 °C. Frequency of daily occurrence of sunning clusters (proportion of days on which clusters were observed) was significantly positively correlated with daily increase in the internal temperature of the nests. This holds even when the increase in the internal temperature of the nests is corrected for increase that occurs at the same external temperature, but in the absence of clustering. This statistical evidence clearly indicates that sun-basking contributes to the heating of nests in spring, but it is very low. This is supported by the fact that nests that differ substantially in the frequency of occurrence of sunning clusters do not differ significantly in internal nest temperature in spring.

Keywords: red wood ants; social behaviour; sun-basking behaviour; sunning clusters; thermoregulation

Introduction

Red wood ants, *Formica rufa* group, are important keystone species in boreal and temperate forests in Eurasia, where they are important predators and ecosystem engineers (Hölldobler and Wilson 1990). Their importance is associated with their building large nest mounds from soil, needles and other organic material, which serve both as a shelter for adults and an incubator for the brood (Wilson 1971; Jones and Oldroyd 2006). One nest can contain up to a million workers and last for decades (Dlusskij 1967; Hölldobler and Wilson 1990; Stockan and Robinson 2016). The structure of their nests, together with various behavioural adaptations, enable wood ants to maintain a stable temperature in their nests above 20 °C during spring and summer, which enables faster development of their brood and a continuous production of sexual offspring and workers (Kneitz 1964; Rosengren et al. 1987; Frouz 2000; Jones and Oldroyd 2006), which contribute to their ecological success. The temperature regulation in the nest starts by a great increase in temperature in March and April and a high temperature is maintained until September when thermoregulation stops, even though workers continue to forage and are active. This is most likely related to the reproduction period of queens (Kipyatkov and Shenderova 1990; Kadochová and Frouz 2014a).

Thermoregulation in red wood ants is a complex process. The structure of the nest provides excellent insulation and is a collector of solar energy (Brandt 1980; Frouz 1996; Frouz 2000; Kasimova et al. 2014). However, during the period of active thermoregulation inner heat sources are crucial. There are three internal heat sources: 1) heat generated by microbial activity of material inside the nest (Coenen-Staβ et al. 1980), 2) metabolic heat produced by the ants (Kneitz 1964; Martin 1980; Horstmann and Schmid 1986; Rosengren et al. 1987; Kadochová and Frouz 2014a) and 3) heat transported by ants in their bodies (Zahn 1958). The latter mechanism is based on the absorption of solar radiation by ants when they are outside the nest. When they return to the nest, this heat is dissipated as they cool down and as a consequence the inner temperature of the nest increases. This may occur during the whole year and be greatly enhanced by the heat transfer of sunning clusters.

Sun basking or formation of dense thick clusters of ants on the surface of nests is frequently reported (Zahn 1958; Rosengren et al. 1987; Frouz 2000) in spring, when an increase in nest temperature occurs. Exposure to solar radiation is widely used by both solitary and social insects to increase their body temperature (Heinrich 1995; Challet et al. 2005). However, sun basking in red wood ants is reported to make the increase in body temperature much more efficient (Kadochová et al. 2017). This is likely to be due to the fact that clustering results in a mass that is much greater than that of single ant and hence a much lower surface to volume ratio, which results in much smaller thermal loses for clusters than individual ants and faster warming of ants in clusters. Zahn (1958) postulated that formation of sunning clusters is a means of transporting heat. However, although this was widely accepted (Rosengren et al. 1987; Frouz 2000; Kadochová

Chanas, P., Frouz, J.: Sunning clusters of ants contribute significantly, but weakly to spring heating in the nests of the red wood ant, *Formica polyctena*
European Journal of Environmental Sciences, Vol. 15, No. 1, pp. 28–33
https://doi.org/10.14712/23361964.2025.4

and Frouz 2014b; Kadochová et al. 2019), to the best of our knowledge, it has never been tested.

The aim of this study is to determine the relationship between occurrence of sunning clusters and increase in red wood ant's nest temperature in spring. The following three hypotheses were tested: 1) During days when the presence of sunning clusters is recorded the internal temperature of the nests increases more than when no clusters were recorded and the daily increase in the internal temperature will be higher on days when clusters occur more frequently. 2) The efficiency of sunning clusters for heating nests will be highest in spring. In early spring the efficiency of clusters may be limited by the fact that not all the ants are active and the number of workers that can participate in clustering is limited, whereas later, when spring internal heat production has started, relative importance of clustering will be less. Finally, 3) it is also expected that forming clusters more often will heat up nests faster during summer. In addition to testing these hypotheses the relative contribution of sunning clusters to spring temperature increase will be estimated.

Materials and Methods

Study site

This study was carried out in the southern part of the Czech Republic at Batkovy near Tabor (724 m a. s. l.) in a forest dominated by Norway spruce (*Picea abies*). Ten nests of *Formica polyctena* were selected that were about 1 m^3 in size and located at the edge of the forest or up to 20 m from the edge. This site was chosen as several previous studies on ant thermoregulation were done here (Frouz 2000; Frouz and Finer 2007).

Data collection

To record the occurrence of clusters of ant workers on the surfaces of nests during spring, 10 infrared digital scouting cameras (UV565 HD) were mounted on trees at a height of about 2 m and each focused on a nest. The cameras took pictures every day from 7:00 a.m. to 8:00 p.m. at 20-minute intervals (40 photographs per day) from 10th March to June 3, 2016. At the same time, cameras recorded external temperature. To record internal nest temperature one digital thermometer attached to a data logger (Testo 174T, Germany) was placed in each nest. Thermometer sensors were placed in the middle of each nest 20 cm below the surface of the mound (near the heat core: Coenen-Staβ et al. 1980; Frouz 2000; Frouz and Finer 2007; Kadochová and Frouz 2014b; Kadochová et al. 2019) in the middle of November 2015 in order to avoid disturbing the structures of the nests at the beginning of the spring when ant activity begins to increase. Temperature was measured every hour. The occurrence of clusters was evaluated manually from camera photographs. For analysis of the incidences of two categories: cluster present and cluster absent were recorded. For sunning cluster to be classified as present, ants have to be densely packed, forming a continuous mass of ants in a way that the surfaces of the nests were not visible and the clusters were at least 100 cm^2, which is about the size of human hand, which is similar to the size of clusters described by other authors.

Data processing

The main parameter evaluated was daily changes in the internal temperature of nests, which was calculated for each nest and date of observation as the difference in the internal temperature measured at 8:00 p.m. minus temperature measured at 7:00 a.m. on the same day.

Because daily changes in the internal temperature can be affected by the external temperature in addition to presence of clusters, a linear regression between external temperature and daily changes in nest temperature, using all 589 daily observations when no clusters were recorded. This linear regression was used to calculate expected daily temperature changes for each day of observation when only influenced by the external temperature. Daily changes in the internal temperature corrected for the effect of external temperature were calculated based on temperature changes minus those predicted for average external temperature on a given day based on the external temperature recorded near each nest.

The difference in internal nest temperature was correlated with daily frequency of the occurrence of sunning clusters, which was based on the number of records of when sunning clusters were present on a given day, divided by total number of observations made daily on each nest (here 40).

To evaluate the effect of sunning clusters on nest temperature during whole period of observation, the average frequency of daily sunning clusters was calculated for each nest and the average calculated for all the days they were recorded. Likewise, average internal temperature was calculated as average of all temperatures recorded in each nest during whole observation period. All data processing and handling was done using MS Excel.

Results

Comparison of the results for consecutive days with and without occurrence of sunning clusters reveals that temperatures were higher on days when cluster were recorded and increases during the day, that is, between 7:00 a.m. and 8:00 p.m. (Fig. 1A, B). This, however, was not the case for nests in summer when the temperature in the nests exceeded 20 °C (Fig. 1C).

The correlation between frequency of cluster occurrence and daily temperature changes (i.e., difference between temperatures at 8:00 p.m. and 7:00 a.m.) (Fig. 2A) over the whole period of observation reveals that the daily internal temperature increased significantly with increasing occurrence of sunning clusters. This holds for

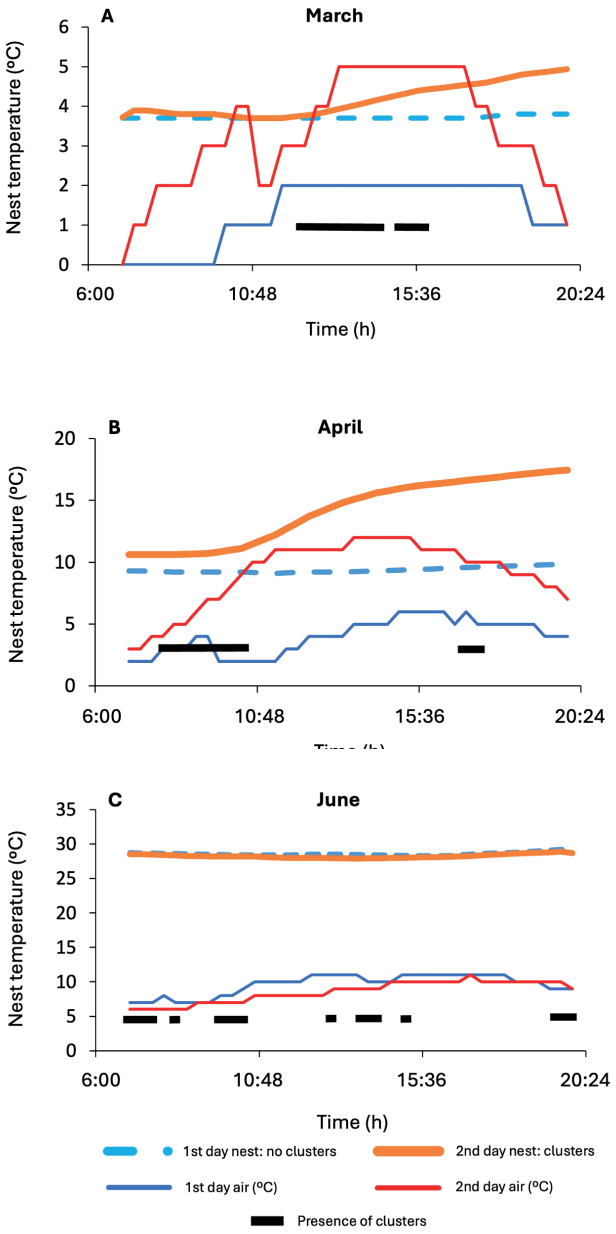

Fig. 1 Comparison of the changes in nest temperature that occurred on two consecutive days in which on the first day there were no sunning clusters and on the second day there were. Horizontal bars indicate presence of clusters on the second day. Line represents air temperature on 1st and 2nd day, which in A) was March, B) April and C) June, respectively.

the whole observation period as well as for observations done on nests with internal nest temperatures below 10 °C and between 10 °C and 20 °C. However, for nests with a temperature over 20 °C there was no significant relationship between occurrence of sunning clusters and daily changes in the internal temperature of nests. Comparison of the daily changes in the internal temperature of nests without and with sunning clusters revealed that temperature increased more in nests without sunning clusters (t-test, $p = 0.0103$).

However, as depicted in Figs 1A and 1B, days on which sunning clusters were recorded may be warmer than on days when they were not recorded. Thus, the recorded temperature increase may not be due to presence of sunning clusters, but that sunning clusters indicate warmer days. To compensate for this the daily increase in the internal temperature of nests was expressed as the average external temperature for all days when sunning clusters were not recorded. This relationship, as expected, indicates that weather conditions affect the increase in nest temperature. To correct for this effect, expected daily temperature changes based on external temperature was calculated and subtracted from the recorded daily changes in temperature These changes in temperature were then correlated with the frequency of occurrence of sunning clusters as above. This also indicates that an increasing frequency in sunning clusters is also associated with a significantly higher daily increase in the internal temperature of nests, based on data recorded over the whole observation period (Fig. 3A). When evaluated separately for data for nests with various internal temperatures, this relationship was significant only for nests with internal temperatures between 10–20 °C. For temperatures below 10 °C this relationship was positive but only marginally significant (Fig. 3B). As above, no effect of sunning clusters on daily temperature changes was recorded for nests with temperatures over 20 °C. In contrast, for the results that were not corrected for the effect of the external temperature there were no statistically significant difference in the temperature in nests on days with and without sunning clusters (Fig. 3D). In both cases the highest effect of sunning clusters (based on the slope of regression) was for nests with an internal temperature between 10 °C and 20 °C (Fig. 2C, Fig. 3C). This also corresponds with the records depicted in Fig. 1.

The effect of sunning clusters on changes in the internal temperature of nests, despite being significant, was very weak. Based on the R^2 values in Figs 2A–C and Figs 3A–C sunning clusters account for less than 10% of the variability in daily changes in temperature (whether corrected for the effect of external temperature or not). The slope of the regression in Fig. 2 and Fig. 4 also indicate that if sunning clusters were present throughout a day the increase in nest temperature would be at most 5 °C. This is quite a lot for one day and the example in Fig. 1B indicates that this may occur on some days, but sunning clusters are not present every day and usually not for a whole day. As the average daily frequencies of sunning clusters for the whole observation period vary for individual nests between 0.02 to 0.1 (Fig. 4), the average effect on daily temperature increase would be less than 0.5 °C. Therefore, it is not surprising that there were no significant differences in the average internal temperatures of nests studied, despite the several fold difference in occurrence of sunning clusters on different nests (Fig. 4).

Discussion

As cited above, many authors who have studied sunning clusters in red wood ants (Zahn 1958; Rosengren et al. 1987; Frouz 2000; Kadochová and Frouz 2014b;

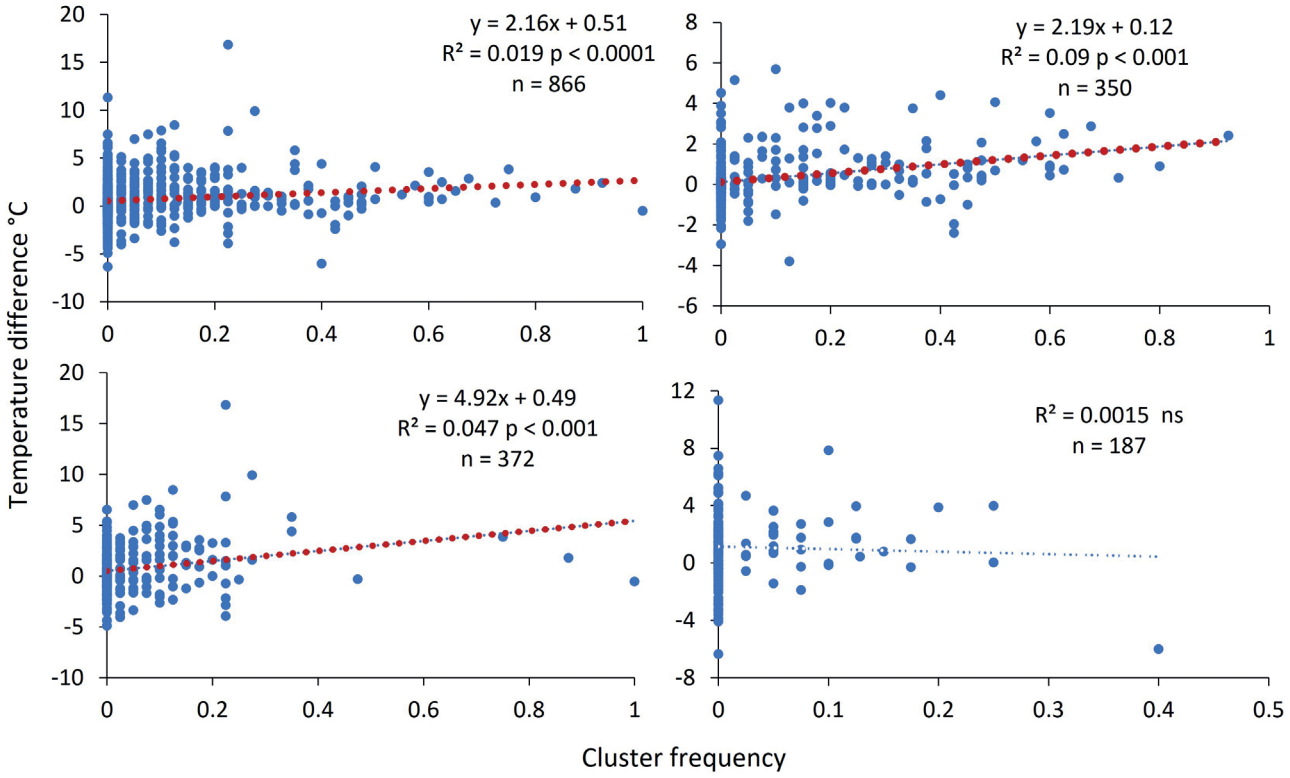

Fig. 2 Relationships between daily differences in internal nest temperature and daily frequency of cluster occurrence A) for all the data, B) for internal nest temperature below 10 °C, C) for internal nest temperature between 10 °C and 20 °C, and D) for internal nest temperature above 20 °C. Text on figures is the equation of the linear regression R^2 and p value and number of observations. Regression line and equation were omitted if correlation was not significant.

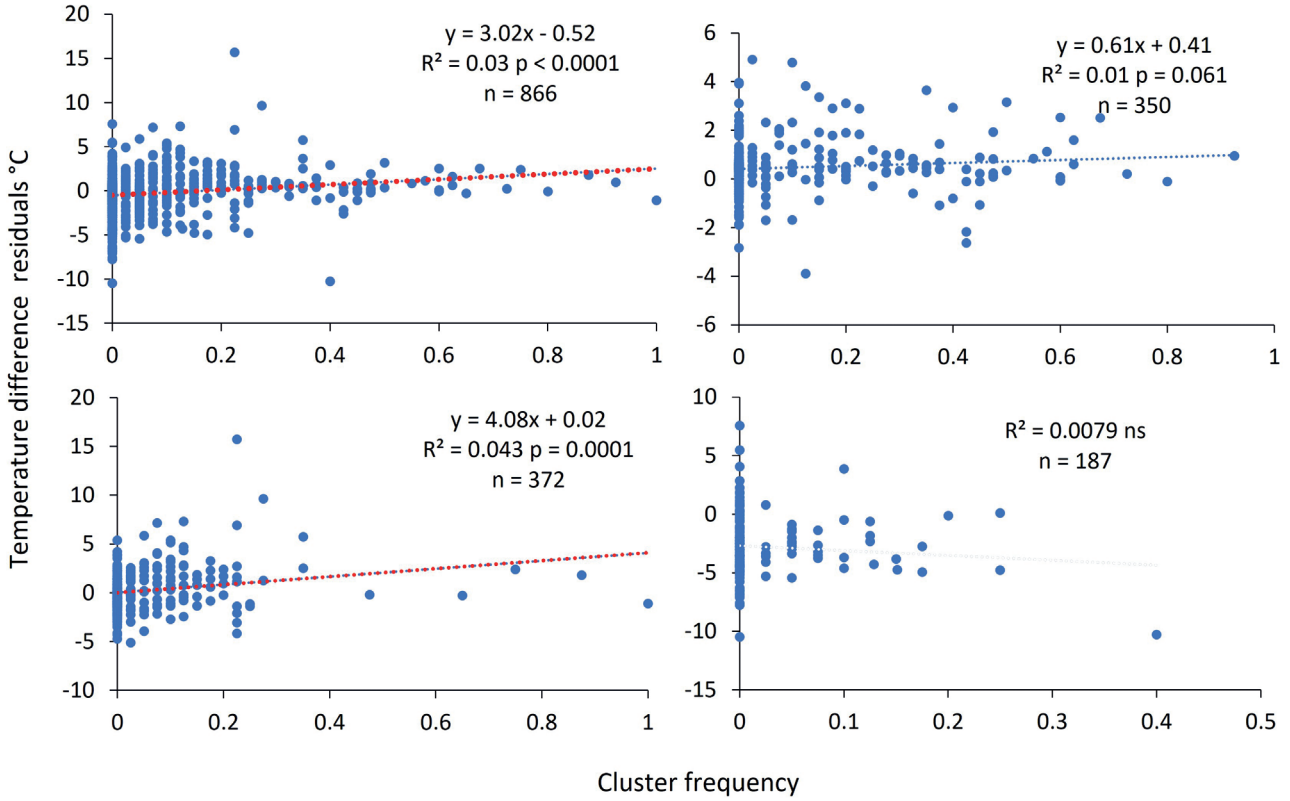

Fig. 3 Relationship between daily differences in internal nest temperature corrected for predicted daily temperature difference, when clusters were not present at the same temperature and daily frequency of cluster occurrence A) for all available data, B) for internal nest temperatures below 10 °C, C) for internal nest temperatures between 10 °C and 20 °C, and D) for internal nest temperatures above 20 °C. Text on figures is the equations of linear regression R^2 and p value and number of observations. Regression line and equation were omitted if correlation was not significant. Red line is used for correlations that are significant at $p < 0.1$.

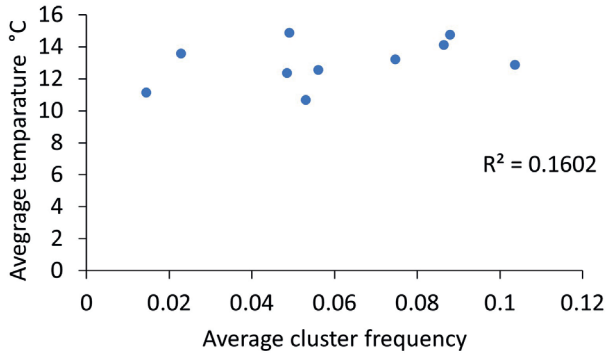

Fig. 4 Relationship between the average temperature of nests over the whole observation period in spring 2016 and average cluster frequency recorded for the same nests. R^2 value indicates non-significant relationship.

Kadochová et al. 2019) suggest that this behaviour helps to transfer heat accumulated in bodies of workers into the nest and in so doing increases the temperature inside nests. The current study revealed that increase in frequency of sunning clusters results in an increase in the internal temperature of nests over course of a day even if corrected for the effect of external temperature (Fig. 3). To the best of our knowledge, this is first quantitative support for the assumption that sunning clusters helps in the heating of nests in spring.

In accordance with hypothesis 2 proposed above, the effect of sunning clusters on the internal temperatures of nests is highest early in spring, when nest temperature is between 10 °C and 20 °C (Fig. 2 and Fig. 3). The expectation was that in early spring, when temperatures in nests are low, the transfer of heat may be limited by the fact that not all the workers are active and most are in hibernation. In addition, solar declination changes during the course of a year (Rueda et al. 2024), which affects solar irradiation that is lower in early spring than in late spring or summer. More detailed measurements, however, would be needed of the heat capacity of clusters and solar radiation to test these assumptions. In contrast, when nest temperature is over 20 °C, internal nest temperature is maintained by the heat produced by ants and decomposition of nest material (Martin 1980; Frouz 1996, 2000; Jílková and Frouz 2014) and the role of sun basking is limited.

However, despite the effect of sunning clusters in increasing the internal temperatures of nests it is relatively weak compared to other factors. That is, contrary to the proposed hypothesis 3, there was no significant relationship between average frequency of sunning clusters and nest temperature over the whole period of observation. This is rather surprising considering the fact that ants in the clusters can become very warm (Kadochová et al. 2019) with the heat capacity of ant bodies two orders of magnitude higher than that of nest material (Frouz 1996). There may be several reasons for this, one factor could be the frequency of clusters is relatively low, with averages over the whole spring of up to 0.1, which means clusters were recorded in 10% of the observations. Relationship between cluster frequency and daily temperature increase indicates that when clusters occur throughout a day the temperature may increase by up to 5 °C. But when clusters are only recorded in 10% of the observations, the daily increase in temperature is only about 0.4 °C. Another important factor is the low thermal conductivity of nest material (Frouz 1996), which means that when ants return to a nest, they may form a hotspot, which may not be recorded as an increase in temperature in the centre of a nest, which has been reported in similar systems (Albdour et al. 2022).

This, however, also may indirectly be the result of higher body temperatures of the ants in nests as ant respiration increases with temperature (Kadochová et al. 2017), which may result in an increase in worker's respiration, which is an important source of heat for maintaining the internal temperature of nests (Frouz 1996, 2000; Jílková and Frouz 2014). In this way sunning clusters may contribute to an increase in the internal temperature of nests in spring by a process that was not considered in the current study. This is indirectly supported by the record that the highest effect of sunning clusters on the temperature in nests occurred when the temperature was between 10 °C and 20 °C and the nest material was already slightly warm and the ants inside the nest remain warm for longer and their respiration may then also contribute to nest heating.

Production of hotspots within nests may also have other positive effects in being attractive to queens, which may start laying eggs (Kipyatkov and Shenderova 1990), which may result in an earlier first generation of offspring (Porter 1988; Roces and Núñez 1989). Formation of these hotspots may also terminate diapause in workers and result in earlier onset of activity in the colonies. The results complement those of other studies that indicate that nest temperature is influenced by many factors that vary throughout a year (Coenen-Staß et al. 1980; Rosengren et al. 1987; Frouz 1996; Frouz and Finer 2007; Kadochová and Frouz 2014b; Kadochová et al. 2019).

Conclusions

This study shows that sunning clusters formed by red wood ants contribute to the spring increase in the internal temperature of their nests. The direct effect of sunning clusters on temperature increase is, however, relatively small. It is likely that sunning clusters contribute to the start in ant colony activity in spring by other indirect mechanisms. These results complement those of other studies indicating that nest temperature is influenced by many factors and varies throughout a year.

Acknowledgements

This work was supported by the Ministry of Education, Youth, and Sports of the Czech Republic – MEYS

(project nos. LM2015075, EF16_013/0001782), and DivLand project provided by Czech technological agency. We would like to thank J. Kukla and V. Jílková for their help with the installation of cameras. Thanks also go to J. Hanzelka for his help with the preparation of raw data from data loggers.

REFERENCES

Albdour SA, Haddad Z, Sharaf OZ, Alazzam A, Abu-Nada E (2022) Micro/nano-encapsulated phase-change materials (ePCMs) for solar photothermal absorption and storage: Fundamentals, recent advances, and future directions. Prog Energy Combust Sci 93: 101037.

Brandt CJ (1980) The thermal diffusivity of the organic material of a mound of *Formica polyctena* in relation to the thermoregulation of the brood (Hymenoptera, Formicidae). Neth J Zool 30: 326–344.

Challet M, Jost C, Grimall A, Lluc J, Theraulaz G (2005) How temperature influences displacements and corpse aggregation behaviors in the ant *Messor sancta*. Insectes Soc 52: 309–315.

Coenen-Staβ D, Schaarschmidt B, Lamprecht I (1980) Temperature distribution and calorimetric determination of heat production in the nest of the wood ants *Formica polyctena* (Hymenoptera, Formicidae). Ecology 61: 238–244.

Dlusskij GM (1967) Ants of the genus *Formica*. Nauka, Moscow. [in Russian].

Frouz J (1996) The role of nest moisture in thermoregulation of ant (*Formica polyctena*, Hymenoptera, Formicidae) nests. Biologia 51: 541–547.

Frouz J (2000) The effect of nest moisture on daily temperature regime in the nests of *Formica polyctena* wood ants. Insectes Soc 47: 229–235.

Frouz J, Finer L (2007) Diurnal and seasonal fluctuations in wood ant (*Formica polyctena*) nest temperature in two geographically distant populations along a south-north gradient. Insectes Soc 54: 251–259.

Heinrich B (1995) Insect thermoregulation. Endeavour 19: 28–33.

Hölldobler B, Wilson EO (1990) The Ants. Belknap Press, Springer, Berlin.

Horstmann K, Schmid H (1986) Temperature regulation in nests of the wood ant, *Formica polyctena* (Hymenoptera: Formicidae). Entomol Gen 11: 229–236.

Jílková V, Frouz J (2014) Contribution of ant and microbial respiration to CO_2 emission from wood ant (*Formica polyctena*) nests. Eur J Soil Biol 60: 44–48.

Jones JC, Oldroyd BP (2006) Nest Thermoregulation in Social Insects. Adv Insect Physiol 33: 153–191.

Kadochová Š, Frouz J (2014a) Thermoregulation strategies in ants in comparison to other social insects, with a focus on red wood ants (*Formica rufa* group). F1000Res 2: 280. doi: 10.12688/f1000research.2-280.v2.

Kadochová Š, Frouz J (2014b) Red wood ants *Formica polyctena* switch off active thermoregulation of the nest in autumn. Insectes Soc 61: 297–306.

Kadochová Š. Frouz J, Roces F (2017) Sun basking in red wood ants *Formica polyctena* (Hymenoptera, Formicidae): Individual behaviour and temperature-dependent respiration rates. PLoS ONE 12: e0170570.

Kadochová Š, Frouz J, Tószögyová A (2019) Factors influencing sun basking in red wood ants (*Formica polyctena*): a field experiment on clustering and phototaxis. J Insect Behav 32: 164–179.

Kasimova RG, Tishin D, Obnosov YuV, Dlussky GM, Baksht FB, Kacimov AR (2014) Ant mound as an optimal shape in constructal design: solar irradiation and circadian brood/fungi-warming sorties. J Theor Biol 355: 21–32.

Kipyatkov VE, Shenderova SS (1990) The endogenous rhythm of queens reproductivity in red wood ants (*Formica rufa* group). Zool Zhurnal 69: 40–52.

Kneitz G (1964) Untersuchungen zum Aufbau und zur Erhaltung des Nestwärmehaushaltes bei *Formica polyctena* Foerst (Hym, Formicidae). Dissertation. University of Würzburg, Germany.

Martin AJ (1980) Vernal thermoregulation in mound nests of *Formica aquilonia* Yarrow, the active heating of brood chambers. Izv Akad Nauk Eston 29: 188–197.

Porter SD (1988) Impact of temperature on colony growth and developmental rates of the ant, *Solenopsis invicta*. J Insect Physiol 34: 1127–1133.

Roces F, Núñez JA (1989) Brood translocation and circadian variation of temperature preference in the ant *Camponotus mus*. Oecologia 81: 33–37.

Rosengren R, Fortelius W, Lindström K, Luther A (1987) Phenology and causation of nest heating and thermoregulation in red wood ants of the *Formica rufa* group studied in coniferous forest habitats in southern Finland. Ann Zool Fenn 24: 147–155.

Rueda JA, Ramírez S, Sánchez MA, Guerrero JdD (2024) Sun declination and distribution of natural beam irradiance on Earth. Atmosphere 15: 1003.

Stockan JA, Robinson EJH (2016) Wood Ant Ecology and Conservation. Cambridge University Press, Cambridge.

Wilson EO (1971) The insect societies. Belknap Press of Harvard University Press, Massachusetts.

Zahn M (1958) Temperatursinn, Wärmehaushalt und Bauweise der Roten Waldameisen (*Formica rufa* L). Zool Beitr 3: 127–194.

SIMULTANEOUS MOBILE PM_{10} MONITORING PROVIDES HIGH DEFINITION SPATIAL AND TIME LOCALIZATION OF HOTSPOTS OF POOR AIR QUALITY IN AN URBAN ENVIRONMENT

KAROLINA WALZELOVA[1], SIMON WALZEL[2,*] AND JAN HOVORKA[1]

[1] Institute for Environment Studies, Faculty of Science, Charles University, Prague, Czech Republic
[2] Department of Biomedical Technology, Faculty of Biomedical Engineering, Czech Technical University in Prague, Czech Republic
* Corresponding author: walzesim@fbmi.cvut.cz

ABSTRACT

Many cities suffer from poor air quality resulting from the accumulation of anthropogenic sources of air pollution, especially aerosol particles with an aerodynamic diameter smaller than 10 μm. The urban sources vary significantly in space and time, requiring temporal and spatial monitoring of air quality. Although becoming more common, mobile monitoring still rarely includes a large urban area. The aim was to carry out and analyze a large spatial and temporal monitoring of the variability in air quality in a large urban area in Prague 7. For this purpose, the area of interest was divided into six smaller sub-areas, where a simultaneous and repeated mobile PM_{10} monitoring was done. In the period from December 2019 to May 2020, a total of 174 walks, with a total length of 664 km, were carried out on 10 days. On most of these days, the average PM_{10} concentrations were below the 24-hour limit value (50 $\mu g \cdot m^{-3}$), except for one day, which was a critical day for the whole of the city of Prague. The temporal variability in PM_{10} varied significantly with meteorological conditions, independent of location. The spatial variability in PM_{10} revealed that lower concentrations were always recorded in green urban areas and high concentrations in two types of hotspots, non-coincidental (regular traffic, residential heating) and coincidental (heavy vehicles, cigarette smoke). The method of collecting and evaluating the data allowed a high spatial and temporal PM_{10} distribution monitoring and can be used to identify anomalies occurring in urban areas and for other pollutants at different locations.

Keywords: anthropogenic pollution source; hotspots identification; mobile monitoring; PM_{10}; urban air quality

Introduction

Due to the high concentration of anthropogenic sources and restricted airflow high concentrations of airborne particles mostly occur in cities, where they negatively affect a large number of people and the surrounding environment (Gómez-Moreno et al. 2019). In many cities, aerosol particles with an aerodynamic diameter of less than 10 μm, $PM_{10,}$ are the main pollutant of concern, with traffic, industrial activity, construction activity, residential heating and resuspension being the main sources (Meng et al. 2019).

Air pollution with PM_{10}, along with $PM_{2.5}$, nitrogen dioxide (NO_2), ozone (O_3) and benzo(a)pyrene (BaP) are of major concern, primarily because of its adverse effects on human health (EEA 2025). Polluted air is associated with an increased incidence of respiratory, cardiovascular and dermatological diseases, higher incidence of hospital admissions and premature deaths (Cohen et al. 2017). According to the World Health Organization (WHO), 4.2 million people died prematurely due to air pollution in 2016, with 400,000 deaths per year occurring in Europe (WHO 2018a). The total number of "years of life lost" worldwide is 123 million per year (Lelieveld 2017). Of all the pollutants listed, PM_{10} is considered to be the most dangerous and therefore is also a key indicator of air quality (Kobza et al. 2018; WHO 2018b).

In considering the health of urban residents, it is necessary to identify locations that regularly have higher concentrations of air pollutants than their surroundings. In air quality terms, these locations are called "hotspots" (Gómez-Moreno et al. 2019). Urban hotspots are usually located close to their sources. If the position of the source of the pollution does not change over time it is considered to be a non-coincidental source. On the other hand, if the source of the pollution moves and is not associated with one place it is considered to be a coincidental source.

With the majority of the world's population living in cities, it is essential to monitor air quality carefully and to have a good understanding of the main sources of pollution and, therefore, the most important sources. The monitoring of urban air quality is typically done at particular locations (for example, in the Czech Republic, air quality is continuously monitored by a network of stations operated by the Czech Hydrometeorological Institute), but this approach has limitations:

1. Monitoring is done at only a few selected locations. As a result, specific and up-to-date information on air quality may be lacking for particular urban areas. This can be a problem for spatial planning or for the implementation of measures to reduce ambient air pollution. Although dispersion models include these areas, the calculated values can be inaccurate and may not characterize the actual pollution. Furthermore, the use of air pollution models for urban environments is often not appropriate due to the vertical structure of cities and a large number of other factors (Braniš et al. 2009).

Walzelova, K., Walzel, S., Hovorka, J.: Simultaneous mobile PM_{10} monitoring provides high definition spatial and time localization of hotspots of poor air quality in an urban environment
European Journal of Environmental Sciences, Vol. 15, No. 1, pp. 34–42
https://doi.org/10.14712/23361964.2025.5

2. In many cities, monitoring stations are usually located in places where the highest concentration levels of pollution are expected (e.g. along busy streets) (Berkowicz et al. 1996). However, measurements in these environments are strongly affected by local conditions, so values obtained in this way cannot be considered representative of a whole city and should be interpreted with caution, especially when comparing the air quality in different cities or when assessing human exposure to pollution (Berkowicz et al. 1996; Van Poppel et al. 2013).
3. In some cases, stations cannot be located at a site of interest because of its often-large size (covering an area in the order of several square meters), accessibility (e.g., regular inspections, technical repairs, filter changes and sample collection for analysis), and safety rules for operating in a public place (e.g., avoiding electric shocks, not obstructing the view of roads).
4. Data recorded at fixed stations are often only representative of the immediate vicinity and pollutant concentrations may be quite different from those recorded further away. Since it is not possible to build a network of stations that would cover the whole area, dispersion modelling of air pollution is used. Although modelling is very useful, it still does not provide very accurate temporal and local data, as it is based on simplified assumptions of pollutant behaviour (Braniš et al. 2009).

To overcome these limitations, it may be desirable to use mobile measurements (Samad and Vogt 2020). This strategy is based on collecting air pollution data by making real-time measurements in the area of interest using portable devices. Devices can be carried by people or installed on cars, bicycles, etc. However, measurements collected using cars are limited to roadways and cars contribute to air pollution.

Repeated mobile measurements in urban environments provide a fairly accurate picture of the spatial and temporal distribution of pollutants (Van Poppel et al. 2013). For example, Berghmans et al. (2009) measured the exposure of cyclists to ultrafine particles (UFP) in an urban environment using a specially equipped bicycle. Many studies have used mobile stations to quantify the exposure of urban passengers using different modes of transport (Panis et al. 2010; Zuurbier et al. 2010; Okokon et al. 2017). Kaur et al. measured their exposure to CO, UFP and $PM_{2.5}$ in urban areas in London (UK) using mobile volunteers to collect the data (Kaur et al. 2005). Maps of mobile measurements that reveal the spatial variability in air pollution at a high resolution have been used to characterize the contributions of local sources to UFP (Hagler et al. 2010) and monitor PM_{10} air pollution in urban environments (Peters et al. 2013). Liu et al. report a cross-border study that compared PM_{10}, $PM_{2.5}$, PM_1, particle number concentration, and black carbon, using mobile measurements to study pollutants from heating systems in winter in the Czech Republic and Germany (Liu et al. 2020). Another similar study was carried out in the Czech Republic in an urban environment to monitor air pollution from residential heating by Hovorka et al. (2015).

Although mobile measurements are becoming more popular and there are already methods for setting up and processing the data (Peters et al. 2013; Van Poppel et al. 2013; Van den Bossche et al. 2015), it is still difficult to do this for large areas (including all types of local urban environments), especially in cities.

This paper presents a simultaneous and repeated mobile monitoring of PM_{10} carried out in an urban area in Prague, the capital of the Czech Republic, which aimed at obtaining a high spatial and time resolution of PM_{10}, its variability and identification of significant local PM_{10} hotspots.

Methods

A simultaneous and repeated mobile monitoring of PM_{10} concentrations was carried out in the city of Prague in district 7 with an area of 7.14 km^2 and more than 47 000 residents (ČSÚ 2021). This area was divided into six smaller sub-areas (Fig. 1) with fixed routes for monitoring of approximately equal length (Tab. 1).

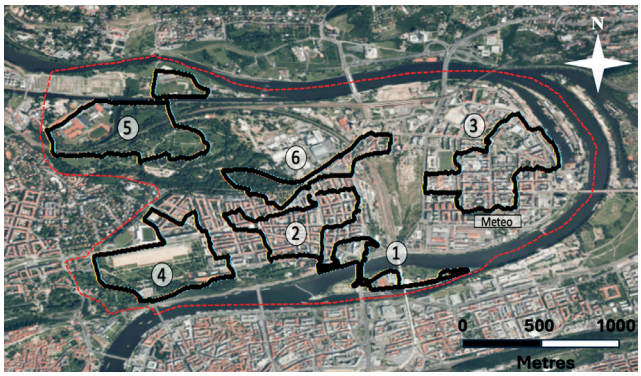

Fig. 1 Map of district 7 in Prague divided into six sub-areas with the routes monitored in black. "Meteo" indicates the location of the WMR 300 meteorological station. The red dashed line marks the borders of Prague 7.

Measurements were made on ten days (weekdays and weekends) between December 2019 and May 2020. Each monitor was assigned a route to measure on a particular day at 08:00, 12:00 and 17:00. The lengths of the routes ranged from 3.4 to 4.5 km.

Equipment

Six DustTrak laser photometers (model 8520, TSI, USA) were used for monitoring PM_{10}. Prior to the start of the monitoring the photometers were calibrated to zero concentrations and airflow measurements done using a factory-calibrated flowmeter. The sampling interval was set to 1 s. To correct for differences between the individual devices, the devices were placed with the sam-

pling heads as close to each other as possible and a joint measurement was made at the Air Quality Laboratory of the Institute for Environmental Studies. Details of the co-location calibration procedure and correction coefficients are provided in the Supplementary Information (Table S1). For the mobile measurements, a photometer was placed in the backpack of each monitor, which sampled air through an omnidirectional sampling head (801565, TSI) that protruded 12–15 cm from the backpack (Fig. 2). Longitude, latitude, altitude, distance from origin and time were recorded by Garmin GPS (models 66s, 64s and eTrex Legend HCx). GPS and DustTrak records were started and stopped simultaneously and paired after each measurement. Meteorological parameters were recorded by Oregon Scientific station (model WMR 300) placed on roofs at a height 24 m above ground (50.101N, 14.451E). Measurements of temperature, air pressure, wind speed and direction, and precipitation were recorded at five-minute intervals.

Table 1 Location and length of the routes in each sub-area.

Route	Sub-area	Length (km)
1	Štvanice Island	3.8
2	Dukelských hrdinů	3.8
3	Holešovice	3.8
4	Letná	3.6
5	Stromovka Forrest Park and Císařský Island	4.5
6	Výstaviště Holešovice	3.4

Protocol

Calibration to zero concentration was done prior to each measurement walk. Recording interval, airflow, current time and memory capacity were checked. The completion of all preparatory steps was recorded in the protocol.

During each measurement walk, each monitor filled out their so-called measurement diaries, which were used to document the location of each measurement. In addition to the date, identification number and time of the start and end of the series of measurements, information about events that could significantly affect the accuracy of PM_{10} concentrations (construction, smokers, a passing train, crossing a dusty intersection) were noted along with subjective observations (traffic exhaust, smoke, strong wind swirling dust) and any technical problems with the devices.

Data processing

The data in the internal memory of the DustTrak devices were downloaded using TrakPro software (TSI, USA) and that from the Garmin GPS (models 66, 64s, and eTrex Legend HCx) using BaseCamp software (Garmin, USA). Data processing and analysis, including statistical processing, were done using Microsoft Excel (Microsoft, USA), ArcMap (Esri, USA), CoPlot (CoHort Software, UK) and MATLAB (2020a, Mathworks, USA).

Fig. 2 Photograph of a DustTrak monitor protruding from the backpack of a member of the monitoring team.

Values less than 1 $\mu g \cdot m^{-3}$ (the detection limit of the DustTrak) were replaced with the detection limit value (1 $\mu g \cdot m^{-3}$) and abnormally high values (above 900 $\mu g \cdot m^{-3}$ and values outside of the PM_{10} rating scale) were removed from the records. The correction coefficients obtained from the co-location calibration procedure were used and urban environment measurements were corrected by multiplying them by 0.32 (Hovorka et al. 2015). This correction was applied because the DustTrak instruments are calibrated for measuring Arizona Road Dust (ISO 12103-1, A1), which differs from typical urban aerosols in particle density, refractive index and size distribution.

Basic statistics were calculated for the PM_{10} data set for each route. The daily and seasonal trend in PM_{10} at each location was tested using the coefficient of divergence (COD). The critical COD value was set at 0.2. Values greater than 0.2 indicate a statistically significant difference between daily measurements (Hovorka et al. 2015). Short-term high PM_{10} concentrations at a location were identified as a hotspot, which were categorized as non-coincidental (traffic, residential heating) and coinci-

dental (cigarette smoke, heavy vehicles) sources. Non-coincidental sources of PM_{10} were defined as those that repeatedly caused an increase in PM_{10} concentrations of at least 1.5 times the median for that particular route and persisted for at least 100 meters. Coincidental sources of PM_{10} were categorized as those that recorded a short-term increase in PM_{10} concentrations and were at least 2 times the median for that route even in units of a few seconds.

Maps with colour-differentiated PM_{10} concentrations

The PM_{10} values recorded by DustTrak combined with the corresponding GPS data and the resulting data file were imported into the ArcMap program of the base map of Prague 7. The points on this map are the PM_{10} concentrations at a given location at a given time and their colour indicates the concentration from dark green (low concentration) through yellow to red (extremely high concentration). This colour scale is the same as the one used for air quality index (AQI) by the US EPA (US EPA 2024), which has been divided into smaller fractions for a more accurate display of data.

Summary 3D graphs with colour-differentiated concentrations of PM_{10}

To compare the profile of PM_{10} concentrations for all routes in a particular sub-area, the PM_{10} values were matched to a sequence of distances unique for each location. A summary 3D graph was then created in CoPlot for each route. The graph shows the trends in PM_{10} at a given time as a function of the distance travelled. The colour-coded values are displayed on a linear scale from 0 to 60 and above in $\mu g \cdot m^{-3}$.

Processing of meteorological data

The meteorological parameters (wind speed and air temperature), recorded at five-minute intervals, were averaged for the days when measurements were recorded and are presented as averages with standard deviations. A wind rose diagram was produced based on the wind speed and direction recorded at the WMR 300 scientific station during the monitoring period. The data were categorized in terms of direction and speed, then the frequency was calculated for each category. The results were then visualized on a polar chart, with the spokes indicating wind direction and their lengths wind speed.

Results

From December 2019 to May 2020, there was a total of 174 monitoring walks over a period of 10 days with a total length of 664 km. Of the ten days, eight were week days and two at weekends, as presented in Table 2. The recorded meteorological parameters (wind speed and air temperature) are presented as averages with standard deviations.

Table 2 Date and day of the week monitored along with the recorded temperatures and wind speeds.

Date	Day of week	Temperature (°C)	Wind speed ($m \cdot s^{-1}$)
09.12.2019	Monday	8.4 ± 1.1	5 ± 1
11.12.2019	Wednesday	0.3 ± 1.9	2 ± 1
20.12.2019	Friday	5.2 ± 3.2	2 ± 1
11.01.2020	Saturday	4.2 ± 1.5	3 ± 1
16.01.2020	Thursday	2.0 ± 2.1	1 ± 1
22.01.2020	Wednesday	0.0 ± 2.9	2 ± 1
06.02.2020	Thursday	0.6 ± 1.5	3 ± 2
20.02.2020	Thursday	4.6 ± 2.0	4 ± 1
22.05.2020	Friday	15.6 ± 3.8	2 ± 1
24.05.2020	Sunday	12.7 ± 2.7	5 ± 2

The average wind speed during the monitoring ranged from 1 to 8 $m \cdot s^{-1}$ and almost half were westerly winds. Southwesterly winds were also common and occurred on one third of the days. The prevailing wind directions at the time of the monitoring are shown graphically in Fig. 3. No precipitation was recorded during the monitoring.

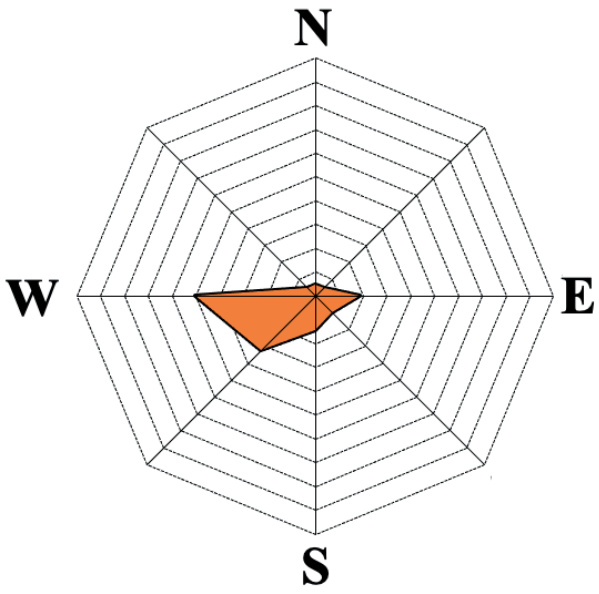

Fig. 3 Windrose for monitoring period.

The effect of seasonal and meteorological conditions on the daily variation in PM_{10}

The 3D graphs with colour-differentiated PM_{10} concentrations in Fig. 4 indicate that highest concentrations

were recorded in winter months on weekdays. The concentrations were highest in December and January (median 20 μg·m^{-3}) than in spring (median 4 μg·m^{-3}). At weekends (Saturday, January 11, 2020, and Sunday, May 24, 2020), the concentrations were very low 2–8 μg·m^{-3}. The 3D graphs with colour-differentiated PM_{10} concentrations for five other locations are listed in the Supplementary information.

The highest PM_{10} concentrations were recorded on January 16, 2020, when they were close to the limit value or above the limit value of 50 μg·m^{-3} in the evening. High values were also recorded at the nearby Czech Hydrometeorological Institute on this day, as shown in Table S2. On average, the values in each sub-area were lower than those recorded by the reference station.

A daily trend in PM_{10} was not recorded, except on the most polluted day, January 16, 2020. A table of average PM_{10} values for all the monitoring walks is listed in Supplementary information (Table S3).

Fig. 5 shows all 6 routes monitored simultaneously on a map with colour-differentiated PM_{10} concentrations. The measurements recorded in the evening of January 17, 2020, show a homogeneous distribution of PM_{10} throughout the area in the city sampled. The average concentrations were around 30 μg·m^{-3} both in park areas and more polluted parts. The best day in terms of air cleanliness was May 22, 2020, when the average for Prague 7 was around 4 μg·m^{-3}.

Significantly lower PM_{10} concentrations were regularly recorded in areas of urban greenery compared to other parts of the city. For example, the median PM_{10} detected in Stromovka Forest Park on December 11, 2019, was 4 μg·m^{-3} lower than the median concentration recorded for the rest of the route in this urban environment, as shown in Fig. 6.

Identification of local hotspots and problem areas

During winter several increases in PM_{10} concentrations were recorded at location No. 1 – Štvanice Island, in the vicinity of a refreshment facility located next to a park for skaters, which acted as a local source of air pollution. For example, on December 11, 2019 (Fig. 7),

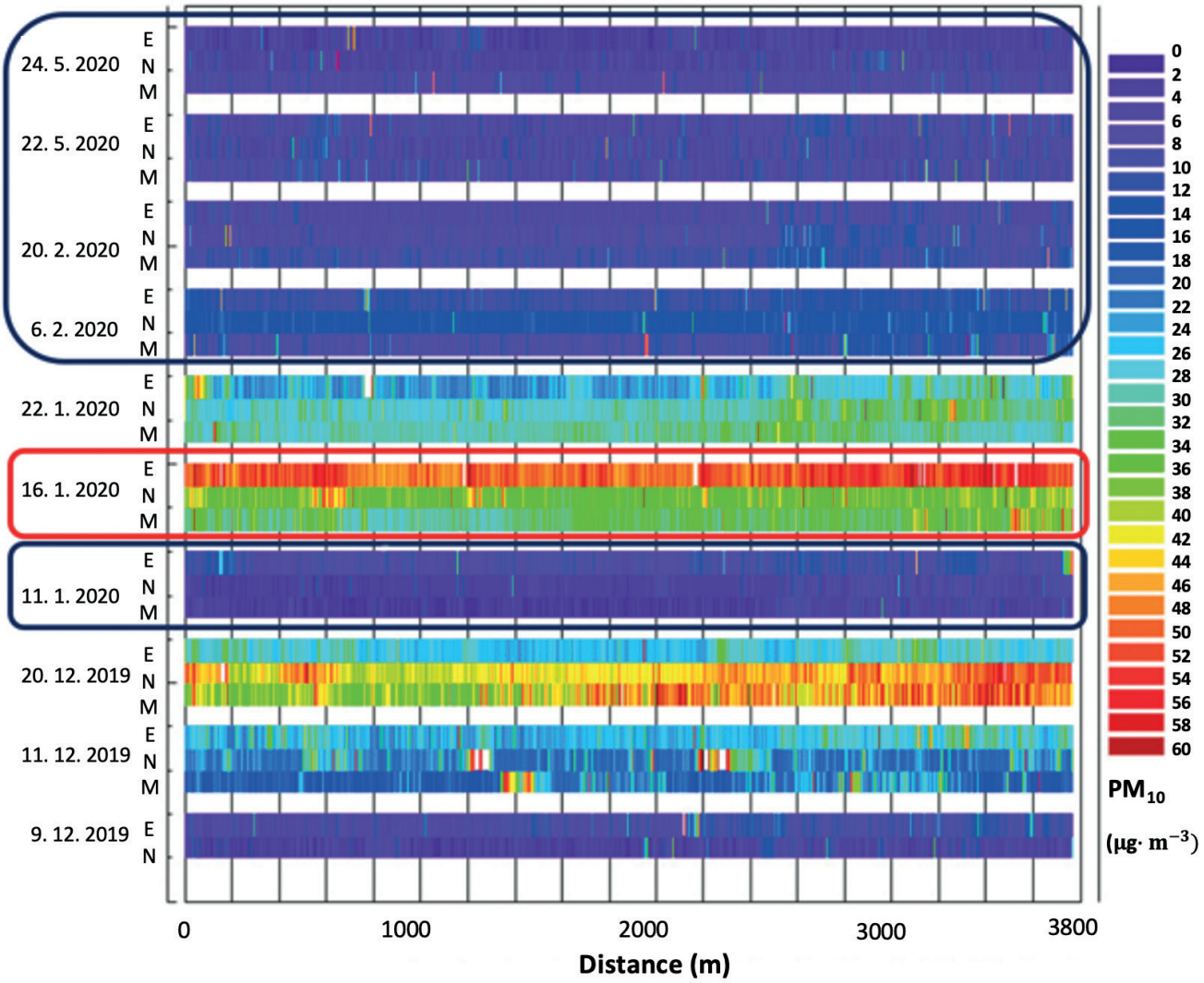

Fig. 4 PM_{10} concentrations on particular days and time of day (M – morning, N – noon, E – evening) depending on the distance travelled during the monitoring walks at location No. 1 – Štvanice Island. Days with very good air quality are indicated along with when the daily limit of 50 μg·m^{-3} for PM_{10} was exceeded on January 16, 2020.

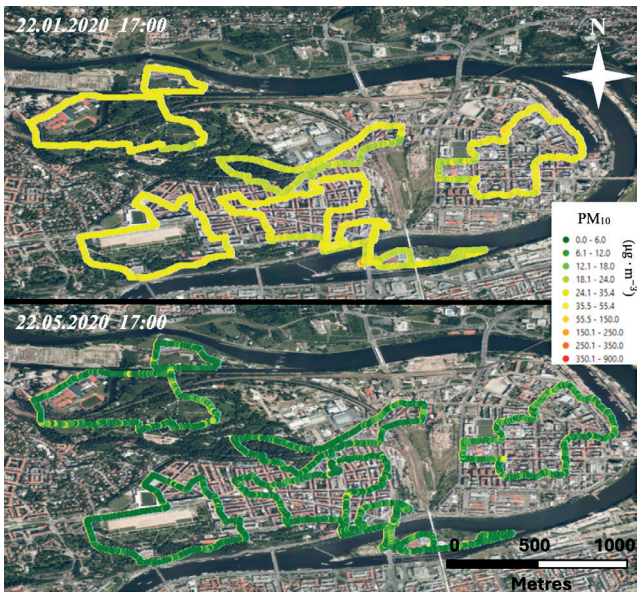

Fig. 5 Aerial photographs showing the level of PM_{10} concentrations recorded along the same monitoring routes in Prague 7 on January 22, 2020, at 17:00 (top) and on May 22, 2020, at 17:00 (bottom).

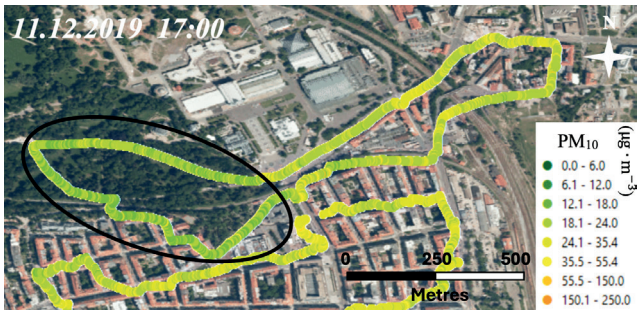

Fig. 6 Aerial photograph showing the effect of urban greenery (area ringed by a black ellipse) on PM_{10} concentrations recorded along a monitoring route.

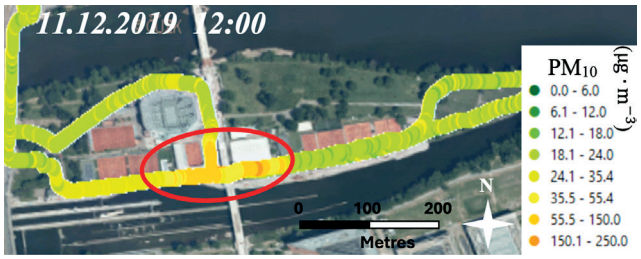

Fig. 7 Aerial photograph showing the 2.8-fold increase in PM_{10} concentrations at location No. 1 – Štvanice Island near a refreshment facility located next to a park for skaters (area ringed by a red ellipse).

the average PM_{10} concentrations were 58 $\mu g \cdot m^{-3}$, which was 2.8 times higher than the median concentration for the whole route and the highest value was 180 $\mu g \cdot m^{-3}$.

A hotspot was identified at the southern end of Hlávkův bridge. High concentrations of PM_{10} were repeatedly recorded there than at the northern end of the bridge. For example, on January 22, 2020, the concentrations were up to 1.4 times higher at the southern end than at the northern end of the bridge (median PM_{10} at the southern end 29 $\mu g \cdot m^{-3}$ and on the northern end 23 $\mu g \cdot m^{-3}$).

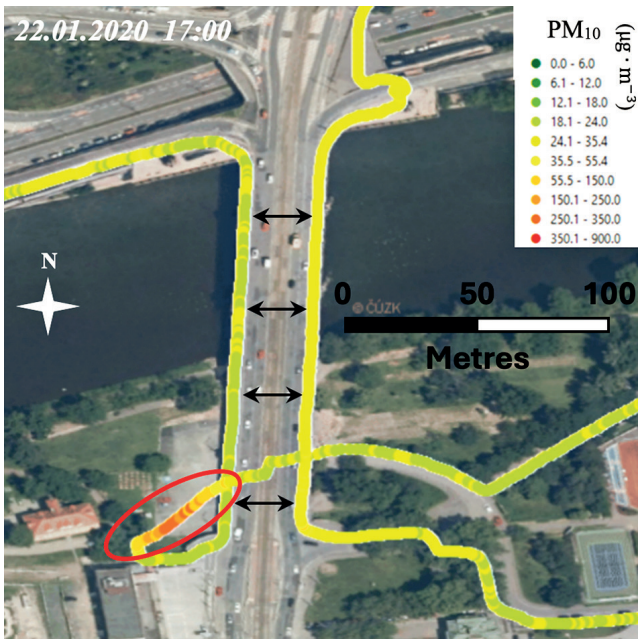

Fig. 8 Aerial photograph of Hlávkův bridge showing the higher concentrations of PM_{10} recorded at the southern end than at the northern end, which is due to the greater level of traffic there (area ringed by a red ellipse) than at the northern end.

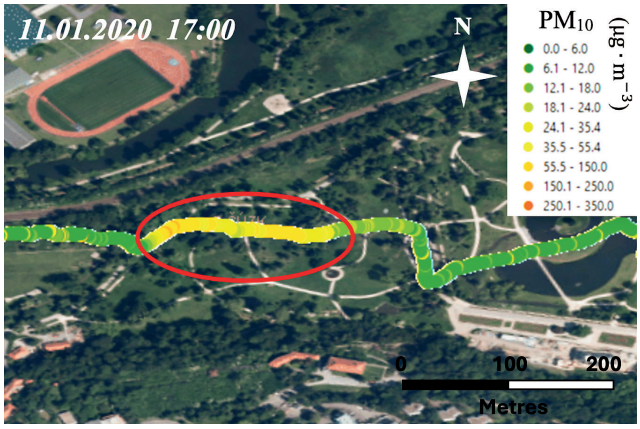

Fig. 9 Aerial photograph showing the location (area ringed by a red ellipse) of the increase in PM_{10} concentrations due to cigarette smokers.

This increase in PM_{10} concentrations was also due to the passage of heavy vehicles and the area affected is ringed by a red ellipse in Fig. 8. The highest value recorded was 300 $\mu g \cdot m^{-3}$.

Fig. 9 Map showings the increased PM_{10} concentrations recorded when walking behind smokers. At such locations, PM_{10} concentrations due to cigarette smoke averaged 70 $\mu g \cdot m^{-3}$, with the highest concentrations detected 150 $\mu g \cdot m^{-3}$.

Discussion

The main finding of this study is a detailed spatial and temporal map of PM_{10} concentrations in an urban area in Prague 7 based on a unique collection of data recorded simultaneously by many mobile monitors.

On most of the days, PM_{10} concentrations in Prague 7 were below the 24-hour limit value (50 $\mu g \cdot m^{-3}$) set by the Czech Act No. 201/2012 on the protection of human health. Concentrations above the limit were only recorded on January 16, 2020, which was a critical day for the whole of Prague. This was due to little wind and below average rainfall in that month (ČHMÚ 2020).

The spatial variability in PM_{10} indicate that the concentrations in Prague 7 depend more on the current meteorological conditions than the localities, as the former has a greater influence on the air movement over the area.

In terms of the size of the area of interest, this is a "neighborhood scale" environmental problem (Chow et al. 2002). In order to achieve a more accurate study, the area was divided into six sub-areas where mobile measurements of PM_{10} concentrations were recorded by walking along pre-selected routes, which is suitable for investigating differences at the "microscale" (Chow et al. 2002) or "street level" (Van Poppel et al. 2013). Routes were selected as representative of all types of urban environments including both main roads and less frequented roads, residential areas, public parks and riverside areas and islands in the Vltava River. Particular attention was paid to school facilities, public sports grounds and homes for the elderly, as these are frequented by children, the elderly and physically active people who are then most sensitive to air pollution from a health point of view.

DustTrak devices (model 8520, TSI) were selected because of the following characteristics: their ability to detect mass concentrations of aerosols outdoors in both clean and heavily polluted environments, stability, ease of use, battery operation, intuitive operation, and they can be pre-programmed to record particular parameters. DustTrak devices have been used for similar measurements (Kaur et al. 2007; Peters et al. 2013; Hovorka et al. 2015; Liu et al. 2020). The use of longer sampling heads and putting them in backpacks enabled samples to be collected at the same height as the normal breathing zone of an adult (approximately 150 cm above the ground). To avoid interfering with the sampling zone, team members were instructed not to wear large scarves or have loose long hair and not to smoke during the measurements.

Analysis of the temporal variability in PM_{10} concentrations revealed they were lower in spring (median 4 $\mu g \cdot m^{-3}$) than in winter (median 20 $\mu g \cdot m^{-3}$) and on weekends than on weekdays. However, remarkably low concentrations of PM_{10} were recorded on January 11, 2020 (median 4 $\mu g \cdot m^{-3}$). This was probably because it was a weekend, which compared to the other measurement days in December and January and less likely to be polluted by sources such as traffic, etc. In addition, meteorological conditions may have influenced air quality, as it rained during the night of January 10–11, 2020, which may have washed pollutants out of the air and the moist ground significantly reduced dust and aerosol resuspension the following day.

Very low concentrations of PM_{10} were recorded in February (median 6 $\mu g \cdot m^{-3}$ on February 20, 2020 and 11 $\mu g \cdot m^{-3}$ on February 6, 2020). Although the ČHMÚ states that air pollution is usually most severe in February, the graphical yearbook for 2020 reports that the lowest monthly average concentration of PM_{10} was recorded in this month. This is due to the presence of uncharacteristically favourable meteorological conditions in terms of wind above-average temperatures and above-average precipitation, which significantly decreased the concentration of air pollutants (ČHMÚ 2020).

The concentrations recorded on Saturday, January 11, 2020 (median 4 $\mu g \cdot m^{-3}$) and Sunday, May 24, 2020 (median 3 $\mu g \cdot m^{-3}$) are among the lowest and are likely to be due to the so-called weekend effect in which there is a reduction in emissions of pollutants at weekends and an increase on weekdays. This trend is characteristic of most large cities and occurs in all seasons (Paschalidou and Kassomenos 2004; Elansky et al. 2020). Lower levels of PM_{10} recorded at weekends than on weekdays are also reported by Titos et al. (2014). The reduction of primary emissions at weekends is due to a reduction in human activities (mainly traffic and industry) and is usually even more pronounced on Sundays than on Saturdays (Adame et al. 2014). There were generally no changes in PM_{10} concentrations during the day, but vertical mixing in response to diurnal cycles strongly influenced by sunlight could affect these changes during the day (Sillman 2003).

The maximum concentrations of PM_{10} varied from place to place, as they were directly influenced by specific sources of pollution in the vicinity of the roads. In urban greenery, PM_{10} concentrations were always several units of $\mu g \cdot m^{-3}$ lower than in city streets. On average, an 18% reduction in PM_{10} concentrations was recorded in urban greenery compared to elsewhere. Thus, greenery can be used as a passive tool for cleaning the air of unwanted pollutants (Gallagher et al. 2015). It is reported that mature trees in urban environments at two sites in England reduced PM_{10} concentrations by 7–26% (McDonald et al. 2007).

Based on the measurements, there are several local hotspots with high PM_{10} concentrations in Prague 7. In all cases they were associated with human activities (traffic, construction work, cigarette smoke or heating). The non-coincidental hotspots included the local heating site on Štvanice Island on route No. 1, the railway crossing in Bubenská street on route No. 6, the construction at Výstaviště in Holešovice on route No. 6 or the southern end of Hlávkův Bridge on route No. 1. As can be seen from the detailed aerial photograph of the island of Štvanice (Fig. 7), there is not only a large tennis court there, but also a skating park, beach volleyball courts and a playground for children. Therefore, the repeatedly recorded high PM_{10} values due to local heating sources in this area are of even more serious concern. In addition, high PM_{10} values, due to construction work, were also recorded at Výstaviště near Jankovského Primary School.

Coincidental sources of PM_{10} were mainly heavy vehicle traffic (e.g., Císařský Island on route No. 5 or Hlávkův Bridge on route No. 1) and cigarette smoke (e.g., Stromovka Forest Park on route No. 5 and Vltavská metro station on route No. 1).

Measures to improve urban air quality should include preventing the emission of dust from construction and demolition sites and of aerosol particles from traffic and local heating, bearing in mind the greater toxic effect of aerosol particles that originate from high-temperature processes. These particles usually include carcinogenic polycyclic aromatic hydrocarbons (Leoni et al. 2016) that are toxic (Topinka et al. 2015) and genotoxic (Topinka et al. 2010) for humans. Therefore, it is advisable to prevent old vehicles from entering the city and to monitor emissions from local heating systems. In order to protect the health of the population, the ban on smoking at public transport stops should also be enforced.

Limitations

This study has several limitations. Although the records spanned a period of six months, they were only collected on ten days. Due to time and financial constraints, it was not possible to continuously measure every day over the course of, say, a year. The monitored days were dependent on the weather and were those, on which there was no rain or snowfall in the area studied and ideally on previous days as well, which wash the pollutants out of the air and thus prevent their detection. Mobile measurements are generally not continuous (e.g. compared to stationary measurements), but episodic. This means that the period of time over which the measurements were recorded was decided prior to the start of the measurements, which are then used to make assumptions about longer time periods. Pollutant concentrations are highly dependent on when they were recorded, however, emission and imission processes in the atmosphere can change rapidly and although it is possible that mobile measurements are good at recording spatial variability, they do not record temporal variability as effectively (Van Poppel et al. 2013).

Conclusion

Simultaneous and repeated mobile monitoring of PM_{10} concentrations was used to describe the spatial and temporal distribution of PM_{10} in Prague 7 and to identify locations with high concentrations of pollution, defined as local hotspots.

In terms of the spatial distribution, PM_{10} concentrations measured over the same time period did not differ significantly between routes, as PM_{10} concentrations depended more on current meteorological conditions than on the location of routes. However, the routes differed in their maxima, the values of which depended on whether the anthropogenic pollution sources were traffic, residential heating or construction.

Concentrations of PM_{10} in Prague 7 were generally below the 24-hour limit value except on one day, which was a critical day for the whole of Prague. Temporal variability revealed lower concentrations at weekends and in spring, as expected, due to reduced human activity and favourable meteorological conditions, respectively.

The results of this study could be used as a basis for decision making on how air quality can be improved and the method used for further studies on the spatial or temporal distribution of several different pollutants.

REFERENCES

Adame J, Hernández-Ceballos M, Sorribas M, Lozano A, De la Morena B (2014) Weekend-weekday effect assessment for O_3, NOx, CO and PM_{10} in Andalusia, Spain (2003–2008). Aer Air Qual Res 14: 1862–1874.

Berghmans P, Bleux N, Panis L, Mishra V, Torfs R, Van Poppel M (2009) Exposure assessment of a cyclist to PM_{10} and ultrafine particles. Sci Total Environ 407: 1286–1298.

Berkowicz R, Palmgren F, Hertel O, Vignati E (1996) Using measurements of air pollution in streets for evaluation of urban air quality – Meterological analysis and model calculations. Sci Total Environ 189: 259–265.

Braniš M, Hůnová I (2009) Atmosféra a klima: aktuální otázky znečištění ovzduší. Praha, Karolinum.

Chow J, Engelbrecht J, Watson J, Wilson W, Frank N, Zhu T (2002) Designing monitoring networks to represent outdoor human exposure. Chemosphere 49: 961–978.

Cohen A, Brauer M, Burnett R, Anderson H, Frostad J, Estep K, Forouzanfar M (2017) Estimates and 25-year trends of the global burden of disease attributable to ambient air pollution: an analysis of data from the Global Burden of Diseases Study 2015. The Lancet 389: 1907–1918.

ČHMÚ (2020) Český hydrometeorologický ústav: Grafická ročenka 2020 [6. 11. 2024]. CHMI.https://www.chmi.cz/files/portal/docs/uoco/isko/grafroc/20groc/gr20cz/Obsah_CZ.html

ČSÚ (2021) Český statistický úřad: Statistický bulletin – Hl. m. Praha – 1. až 3. čtvrtletí 2021 CSU. https://csu.gov.cz/produkty/statisticky-bulletin-hl-m-praha-1-az-3-ctvrtleti-2021.

EEA (2025) European Environment Agency: Air Quality Status report 2025 [9. 4. 2025] EEA Europa. https://www.eea.europa.eu/en/analysis/publications/air-quality-status-report-2025.

Elansky N, Shilkin A, Ponomarev N, Semutnikova E, Zakharova P (2020) Weekly patterns and weekend effects of air pollution in the Moscow megacity. Atmos Environ 224: 117303.

Gallagher J, Baldauf R, Fuller C, Kumar P, Gill L, McNabola A (2015) Passive methods for improving air quality in the built environment: A review of porous and solid barriers. Atmos Environ 120: 61–70.

Gómez-Moreno F, Artíñano B, Ramiro E, Barreiro M, Nuñez L, Coz E, Borge R et al. (2019) Urban vegetation and particle air pollution: Experimental campaigns in a traffic hotspot. Environ Pollut 247: 195–205.

Hagler G, Thoma E, Baldauf R (2010) High-resolution mobile monitoring of carbon monoxide and ultrafine particle concentrations in a near-road environment. J Air Waste Manag Assoc 60: 328–336.

Hovorka J, Pokorná P, Hopke P, Křůmal K, Mikuška P, Píšová M (2015) Wood combustion, a dominant source of winter aerosol in residential district in proximity to a large automobile factory in Central Europe. Atmos Environ 113: 98–107.

Kaur S, Nieuwenhuijsen M, Colvile R (2005) Personal exposure of street canyon intersection users to $PM_{2.5}$, ultrafine particle counts and carbon monoxide in Central London, UK. Atmos Environ 39: 3629–3641.

Kaur S, Nieuwenhuijsen M, Colvile R (2007) Fine particulate matter and carbon monoxide exposure concentrations in urban street transport microenvironments. Atmos Environ 41: 4781–4810.

Kobza J, Geremek M, Dul L (2018) Characteristics of air quality and sources affecting high levels of PM_{10} and $PM_{2.5}$ in Poland, Upper Silesia urban area. Environ Monit Assess 190.

Lelieveld J (2017) Clean air in the Anthropocene. Faraday Discuss 200: 693–703.

Leoni C, Hovorka J, Dočekalová V, Cajthaml T, Marvanová S (2016) Source impact determination using airborne and ground measurements of industrial plumes. Environ Sci Technol 50: 9881–9888.

Liu X, Schnelle-Kreis J, Zhang X, Bendl J, Khedr M, Jakobi G, Zimmermann R (2020) Integration of air pollution data collected by mobile measurement to derive a preliminary spatiotemporal air pollution profile from two neighboring German-Czech border villages. Sci Total Environ 722.

McDonald A, Bealey W, Fowler D, Dragosits U, Skiba U, Smith R, Nemitz E et al (2007) Quantifying the effect of urban tree planting on concentrations and depositions of PM_{10} in two UK conurbations. Atmos Environ 41: 8455–8467.

Meng X, Wu Y, Pan Z, Wang H, Yin G, Zhao H (2019) Seasonal characteristics and particle-size distributions of particulate air pollutants in Urumqi. Int J Environ Res Public Health 16.

Okokon E, Yli-Tuomi T, Turunen A, Taimisto P, Pennanen A, Vouitsis I, Lanki T (2017) Particulates and noise exposure during bicycle, bus and car commuting: A study in three European cities. Environ Res 154: 181–189.

Panis L, de Geus B, Vandenbulcke G, Willems H, Degraeuwe B, Bleux N, Meeusen R (2010) Exposure to particulate matter in traffic: A comparison of cyclists and car passengers. Atmos Environ 44: 2263–2270.

Paschalidou A, Kassomenos P (2004) Comparison of air pollutant concentrations between weekdays and weekends in Athens, Greece for various meteorological conditions. Environ Technol 25: 1241–1255.

Peters J, Theunis J, Van Poppel M, Berghmans P (2013) Monitoring PM_{10} and ultrafine particles in urban environments using mobile measurements. Aerosol Air Qual Res 13: 509–522.

Samad A, Vogt U (2020) Investigation of urban air quality by performing mobile measurements using a bicycle (MOBAIR). Urban Climate 33.

Sillman S (2003) Tropospheric ozone and photochemical smog [Chapter 11]. Sherwood Lollar B, editor. Treatise on geochemistry. Environ Geochem 9.

Titos G, Lyamani H, Pandolfi M, Alastuey A, Alados-Arboledas L (2014) Identification of fine (PM_1) and coarse (PM_{10-1}) sources of particulate matter in an urban environment. Atmos Environ 89: 593–602.

Topinka J, Hovorka J, Milcová A, Schmuczerová J, Kroužek J, Rossner Jr. P, Šrám RJ (2010) Acellular assay to assess genotoxicity of size segregated aerosols. Part I: DNA adducts. Toxicol Lett 198: 304–311.

Topinka J, Rossner Jr. P, Milcova A, Schmuczerova J, Pencikova K, Rossnerova A, Ambroz A, Stolcpartova J, Bendl J, Hovorka J, Machala M (2015) Day-to-day variability of toxic events induced by organic compounds bound to size segregated atmospheric aerosol. Environ Pollut 202: 135–145.

US EPA (2024) United States Environmental Protection Agency: Technical Assistance Document for the Reporting of Daily Air Quality – the Air Quality Index (AQI). AirNow.govhttps://document.airnow.gov/technical-assistance-document-for-the-reporting-of-daily-air-quailty.pdf.

Van den Bossche J, Peters J, Verwaeren J, Botteldooren D, Theunis J, De Baets B (2015) Mobile monitoring for mapping spatial variation in urban air quality: Development and validation of a methodology based on an extensive dataset. Atmos Environ 105: 148–161.

Van Poppel M, Peters J, Bleux N (2013) Methodology for setup and data processing of mobile air quality measurements to assess the spatial variability of concentrations in urban environments. Environ Pollut 183: 224–233.

WHO (2018a) World Health Organization: Ambient (outdoor) air pollution. WHO. https://www.who.int/news-room/fact-sheets/detail/ambient-(outdoor)-air-quality-and-health.

WHO (2018b) World Health Organization: Ambient air pollution: Pollutants.

Zuurbier M, Hoek G, Oldenwening M, Lenters V, Meliefste K, van den Hazel P, Brunekreef B (2010) Commuters' exposure to particulate matter air pollution is affected by mode of transport, fuel type, and route. Environ Health Perspec 118: 783–789.

DETERMINATION OF THE SUITABILITY OF AGILENT BIOANALYZER 2100 FOR INVESTIGATIONS INTO WILDLIFE CRIMES: CASE STUDIES

KRISTÝNA HEBENSTREITOVÁ[1,*], LENKA VAŇKOVÁ[1,2] AND DANIEL VANĚK[1,2,3,4]

[1] Institute for Environmental Studies, Charles University, Benátská 2, 128 01 Prague, Czech Republic
[2] Forensic DNA Service, Budínova 2, 180 81 Prague, Czech Republic
[3] Bulovka University Hospital, Budínova 2, 180 00 Prague, Czech Republic
[4] 2nd Faculty of Medicine, Charles University, Prague, Czech Republic
* Corresponding author: hebenstk@natur.cuni.cz

ABSTRACT

This article examines the use of chip electrophoresis in wildlife crime investigations through three mock case studies. Specifically, we analysed DNA extracted from the tanned hide of *Panthera pardus*, a species protected under the Convention on International Trade in Endangered Species of Wild Fauna and Flora (CITES), at various stages of the tanning process (Case study #1). Tanned hides present a unique challenge due to the detrimental effects of tanning on DNA integrity, resulting in highly degraded DNA extracts. Therefore, assessing DNA integrity before performing standard DNA analyses is critical to conserving laboratory resources. One of the conventional methods for evaluating DNA integrity involves determining the degradation index using quantitative polymerase chain reaction (qPCR). This study explored whether chip electrophoresis, a faster and simpler alternative to qPCR, could provide comparable assessments of DNA integrity. In addition, its applicability for use in established assays, such as the Triplex assay, which is used for rapidly classifying unknown biological material (Case study #2) and species identification based on mitochondrial DNA lenght polymorphism (Case study #3). The findings indicate that while chip electrophoresis is effective in established assays, it is unsuitable for assessing the quality of DNA extracted from tanned hides.

Keywords: chip electrophoresis; DNA degradation; DNA quality control; lab-on-chip; wildlife forensics

Introduction

In recent years, forensic science has undergone a major change as it now uses modern technologies to increase the precision and efficiency of investigative processes.

In the early stages of an investigation, obtaining DNA analysis results quickly is critical for ensuring their relevance and utility in guiding the investigative process (Mapes et al. 2015). This is particularly significant in cases of wildlife crime, where the process of gathering evidence is often complex and challenging (Henger et al. 2023), especially as the DNA analysis can take several days to complete.

Forensic wildlife DNA analysis typically focuses on three key areas: species identification, individual identification, and determining relationships between individuals. The analysis typically involves several steps: collecting and preserving biological samples, extracting and amplifying DNA, sequencing or fragment analysis, and comparing it to reference databases for species or individual identifications. Despite its importance, there are significant challenges, including sample degradation, limited reference data, resource constraints and the need for the expertise of specialists (Kumar et al. 2017). These limitations need to be addressed if the accuracy of wildlife forensic DNA analysis is to be improved.

Devices that provide immediate information on a forensic sample are particularly valuable in facilitating rapid and effective analyses. "Lab-on-a-chip" (LOC) technology is a promising solution as it simplifies the analysis and reduces the time and resources required. A LOC is a device that integrates a laboratory technique within a small chip. Consequently, LOC devices provide swift analyses, require minimal quantities of analyte and are portable (Bruijns et al. 2016).

These new technologies are helping to overcome some of the difficulties in analysing a forensic sample, such as the low resolution of agar electrophoresis in multiplexed protocols or expansivity in the routinary use of capillary electrophoresis (CE). CE generally provides a better resolution than standard agarose gel electrophoresis, but is costly for routine use (Gupta et al. 2010).

The main focus of this article is to explore if it is possible to incorporate the Agilent Bioanalyzer 2100 in the workflow of established assays. We tested the Bioanalyzer in three different mock case studies: #1) Assessment of DNA quality in extracts from samples of a *Panthera pardus* hide in different stages of tanning; #2) Rapid classification of unknown biological material using Triplex assay; and #3) Species identification based on the length polymorphism of the mitochondrial DNA control region (CR-mtDNA).

Each of these studies involves a different method commonly used in forensic analyses (qPCR, Sanger sequencing, Fragment analysis). This article aims to determine whether the Agilent Bioanalyzer 2100 can be used for these analyses and provide similar results.

The first study aimed to assess the quality of the DNA extracted from the tanned hide of *Panthera pardus*. It is often challenging to obtain amplifiable DNA from

Hebenstreitová, K., Vaňková, L., Vaněk, D.: Determination of the suitability of agilent bioanalyzer 2100 for investigations into wildlife crimes: case studies
European Journal of Environmental Sciences, Vol. 15, No. 1, pp. 43–52
https://doi.org/10.14712/23361964.2025.6

tanned hides and furs as it is often degraded (Vuissoz et al. 2007; Hebenstreitova et al. 2024). This is further compounded by the presence of various chemicals and materials used during the tanning process, many of which are PCR inhibitors and also hinder the amplifiability of DNA extracted from tanned hides (Hebenstreitova et al. 2024). However, this is typical of biological samples collected in cases of wildlife crime (Hedmark and Ellegren 2005; Prakash Goyal 2016; Khan et al. 2018; Khedkar et al. 2019; Rajani et al. 2020). Numerous analyses used in wildlife forensic genetics, such as DNA typing or species identification using Sanger sequencing, depend on a certain quantity of amplifiable DNA (Zou et al. 2015). Given that these analyses are both costly and time-consuming, a tool providing a quick assessment of the quality of DNA before these analyses would be advantageous. The conventional approach for assessing DNA quality relies on determining the degradation index (DI) based on quantitative polymerase chain reaction (qPCR). However, the continuous search for faster and more accessible methodologies prompts the exploration of alternative techniques.

The Agilent Bioanalyzer 2100's sensitivity allows the determination of the level of DNA degradation purely on extracted DNA, thus overcoming possible bias due to the effect of inhibitors that affect qPCR.

The Triplex assay is used for the rapid identification of mammalian, nonmammalian and plant DNA in samples of unknown origin (Saskova et al. 2017). The Triplex assay protocol involves a PCR amplification targeting the rbcL gene in plants (RuBisCO), the COI gene in animals (cytochrome oxidase I), and the artificial internal positive control in a single reaction. Visualization of the PCR products via gel electrophoresis then provides information on the presence of animal or plant DNA in the sample. This step can be followed by Sanger sequencing and species identification. The visualization of PCR products can be done using chip electrophoresis instead of agarose gel electrophoresis. Similarly, chip electrophoresis can be used for the identification of species based on the length of the mitochondrial control region (CR-mtDNA) instead of capillary electrophoresis, which speeds up the laboratory process. This method is beneficial when dealing with a mixture of several species in one sample, but can also be used for species assignment in single-source samples (Pun et al. 2009; Vankova and Vanek 2022). However, important forensic validation is needed for the routine use of the Agilent Bioanalyzer 2100.

Materials and Methods

Case study #1

In this study, the hide of *Panthera pardus* that died in Jihlava ZOO was used for tanning. The tanning process was carried out by a professional, using three different commercially available tanning agents: Lutan FN (L, aluminum sulfate), Novaltan AL (N, aluminum triformate) and a chrome-based agent (C, chromium sulfate), all sourced from Bauer Handels, Switzerland. The process (Fig. 1) begins with pre-tanning procedures, which involve trimming the underside of the hide to produce smooth leather (fleshing) and removing impurities, degreasing and breaking down globular proteins (soaking). A two-stage tanning process follows, preceded by acidification (pickling) to enhance the penetration of tanning agents and further thinning. The finishing steps ensure the leather is lubricated (fat liquoring), soft and dry, which improves its durability and resistance (Pachnerová Brabcová et al. 2024).

The hide was labelled at the different stages of the tanning process, as detailed in Fig. 1. Comprehensive details of each tanning stage are described by Hebenstreitova et al. (2024).

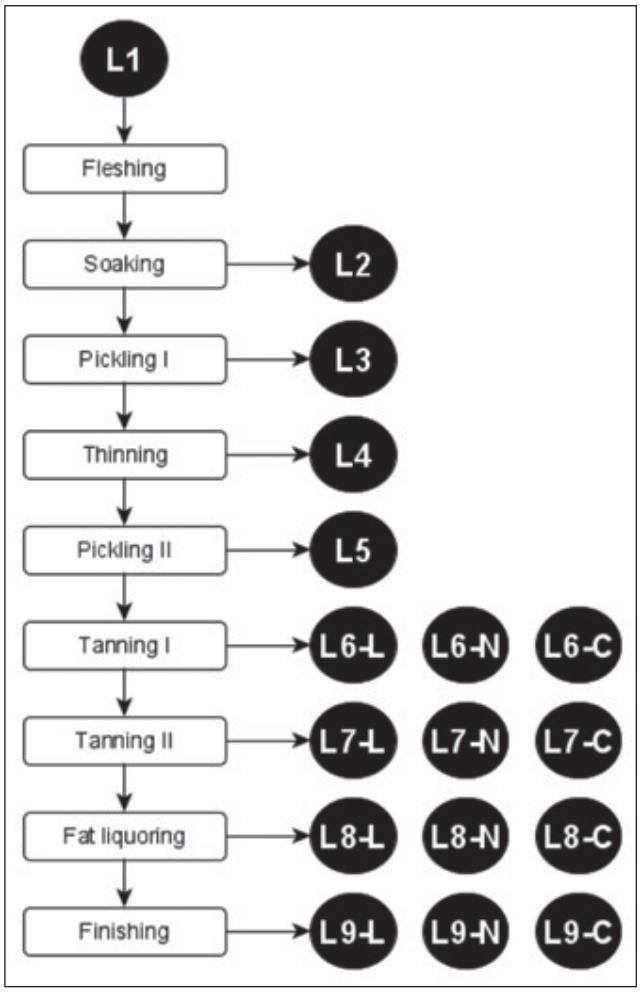

Fig. 1 The tanning process consisted of nine steps (indicated by rectangles), with samples collected at specific stages (dark circles). The first sample (L1) was collected before the tanning process began. After the fifth step, the process differed depending on which of the three tanning agents was used, as indicated in the sample labels: 'L' for Lutan, 'N' for Novaltan, and 'C' for chromium sulphate (as published by Pachnerová Brabcová et al. 2024).

An optimized protocol for extracting genomic DNA (gDNA) from tanned hides was used, which utilized the commercially available Quick-DNA Miniprep Plus Kit (Zymo Research, USA). A detailed description of this

protocol was previously published by Hebenstreitova et al. (2024).

Before analysis using the Agilent Bioanalyzer 2100, all of the DNA extracts were quantified by a Qubit 4 fluorometer (Thermo Fisher Scientific, USA). DNA isolates exceeding 500 pg/µl gDNA were diluted to a final DNA concentration of 250 pg/µl gDNA, which is compatible with the quantitative range of the high-sensitivity DNA kit (Agilent Technologies, USA).

Case study #2

For this study, DNA was extracted from the muscle tissue of *Bos taurus* using the Quick DNA Miniprep kit (Zymo Research) and from the leaves of *Hibiscus* sp. using Quick DNA Plant/Seed Miniprep kit (Zymo Research) according to the manufacturer instructions. The Triplex assay was done according to a previously published protocol (Saskova et al. 2017) with minor changes to the PCR reaction. Five µl of gDNA was amplified (concentration range from 2–4 ng/µl) in a final volume of 25 µl containing 2.5 µl of 10x PCR Buffer II (Thermo Fisher Scientific), 2 µl of 25 mM $MgCl_2$ (Thermo Fisher Scientific), 0.5 µl of 10 mM dNTPs, 1 U of AmpliTaq Gold DNA polymerase (Thermo Fisher Scientific), 1 µl of each 10 µl primer and DNase/RNase-Free Water were added to the final volume. The DNAs of *Bos taurus* and *Hibiscus* sp. were used as template DNA.

Before analysis on the Agilent Bioanalyzer 2100, all of the PCR products were quantified using a Qubit 4 fluorometer (Thermo Fisher Scientific, USA). Products exceeding 500 pg/µl gDNA were appropriately diluted to achieve a final DNA concentration of 250 pg/µl gDNA, which ensures compatibility with the quantitative range of the high-sensitivity DNA kit (Agilent Technologies, USA).

Case study #3

For this study, DNA was extracted from various tissues (blood, faeces, muscle tissue and hair) from seven different species of mammal (*P. leo*, *P. tigris*, *P. pardus*, *B. taurus*, *S. scrofa domesticus*, *O. cuniculus* and *G. gallus*) using the Quick-DNA Miniprep Plus Kit (Zymo Research) according to the manufacturer's instructions. All of these tissue samples were provided by various Zoos in the Czech Republic.

The hypervariable domain of the mitochondrial control region (CR-mtDNA) was amplified using previously published primers and protocols (Pun et al. 2009; Vankova and Vanek 2024). The only variation was that unlabelled primers were used in this case.

Before analysis using the Agilent Bioanalyzer 2100, all of the PCR products were quantified using a Qubit 4 fluorometer (Thermo Fisher Scientific, USA). Products exceeding 500 pg/µl gDNA were appropriately diluted to achieve a final DNA concentration of 250 pg/µl gDNA, which is compatible with the quantitative range of the high-sensitivity DNA kit (Agilent Technologies, USA).

Agilent Bioanalyzer 2100

This analyser was used to visualize and determine the quality of the DNA. It is a microfluidics-based electrophoresis instrument that allows for separation and quantitation of DNA down to pg/µl sensitivity. It is well-established and commonly used for DNA library quality control in next-generation sequencing (Agilent Bioanalyzer System 2018).

The samples were analysed using a high-sensitivity DNA kit according to the protocol provided by the manufacturer. The Agilent High Sensitivity DNA Kit is designed for determining the size and quantity of fragmented DNA in DNA sequencing libraries and DNA samples derived from ChIP. This tool has a 45-minute runtime and a size range of 35 to 10 380 bp and can accommodate 11 samples per chip. It provides a size resolution of ±10% for 50–600 bp and ±20% for 600–7000 bp, with a sample volume requirement of 1 µl. This kit, which remains stable for four months, includes 10 chips (110 samples total) and has a size accuracy of ±10%, size precision with a 5% coefficient of variation (CV), quantitative accuracy of 20%, and quantitative precision of 15% CV for 50–2000 bp and 10% CV for 2000–7000 bp, within a quantitative range of 5–500 pg/µl. The maximum buffer concentration allowed is 10 mM Tris and 1mM EDTA (Panaro et al. 2000; Agilent Technologies 2009). The assay validation followed the ANSI/ASB standard for the internal validation of forensic DNA analysis, as partly described by Webster et al. (2023).

Sensitivity: The analytical sensitivity corresponds to the quantitative range indicated by the manufacturer, which is 5–500 pg of DNA.

Robustness: Robustness was tested using an Agilent Bioanalyzer 2100 in three different assays: quality control of tanned hide DNA extracts, Triplex assay and CR-mtDNA typing, as described above.

Repeatability: Amplicons resulting from the CR-mtDNA and Triplex assays were used to test the repeatability.

Reproducibility: This was tested by running two assays independently.

Specificity: This approach is universal and is used for nucleic acid separation.

Quality control: Negative and positive controls were run in all of the above experiments.

Results

Case study #1

In this study, 17 electropherogram plots were obtained. In samples taken during the preparatory stages of leather-making (L1–L5), fragments of > 1000 bp were recorded (Fig. 2). From the onset of the leather-making process, there is a noticeable shift towards shorter fragments, with fragments ≥ 1000 bp virtually absent (Figs 3–5). In addition, the DNA in leather samples treated with chromium sulphate was the most degraded, as no

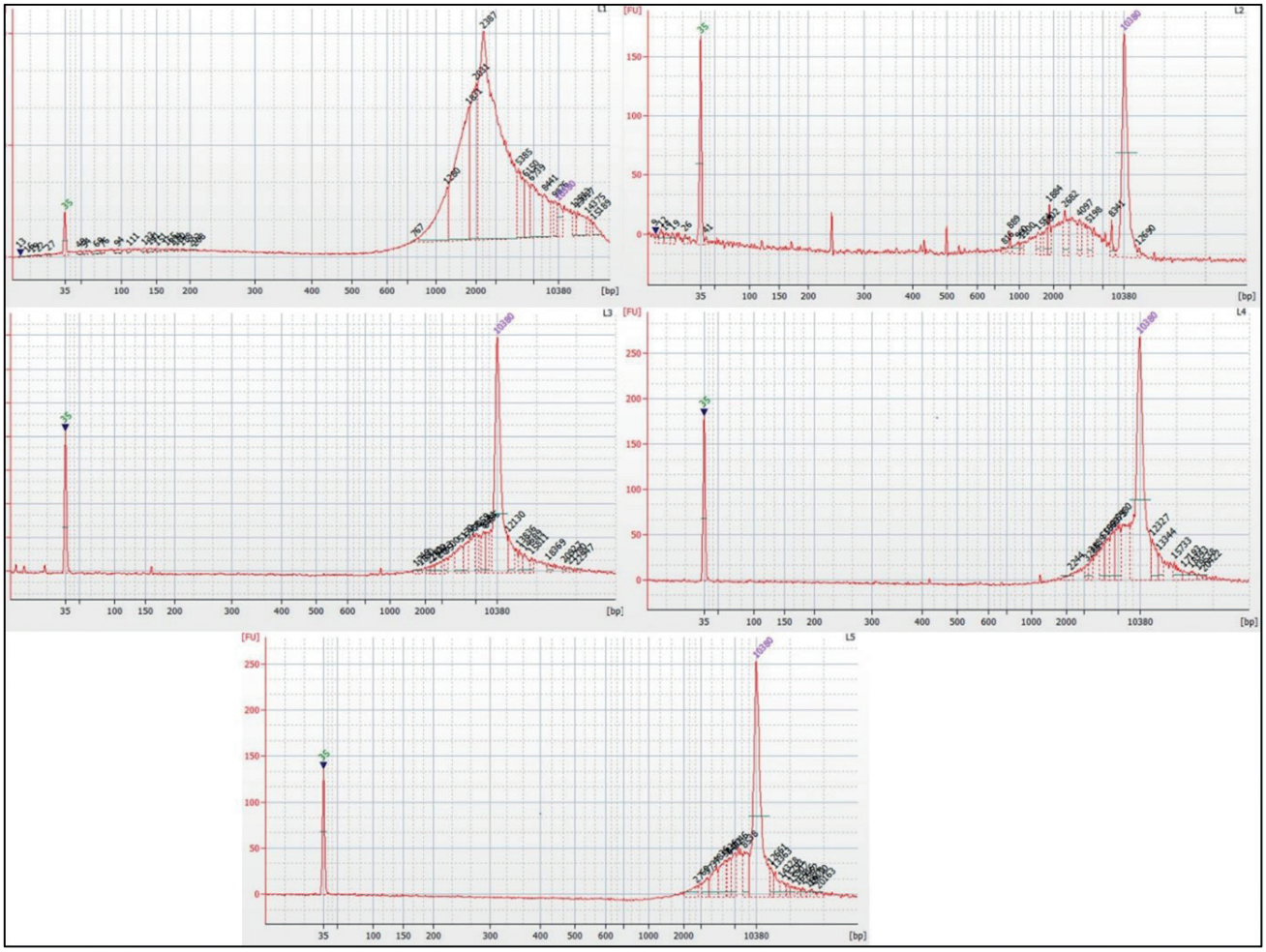

Fig. 2 Electropherograms recorded for samples L1 to L5, respectively, using the Agilent Bioanalyzer 2100. The values on the y-axis are units of fluorescence (FU) and on the x-axis fragment lengths in base pairs (bp). The size range is defined by two distinct peaks: the position of the lower is for 35 bp and the upper for 10,380 bp.

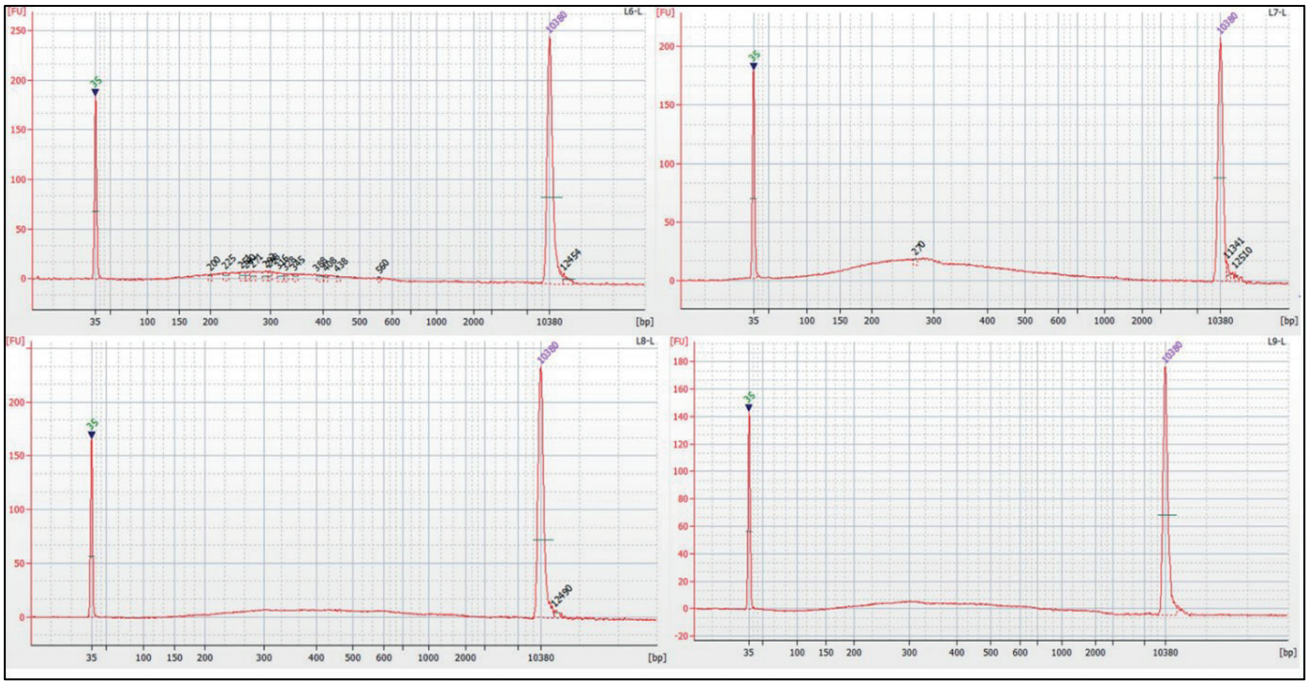

Fig. 3 Electropherograms recorded for the Lutan FN-tanned samples L6 to L9, respectively, quantified using the Agilent Bioanalyzer 2100. The values on the y-axis are units of fluorescence (FU) and x-axis fragment lengths in base pairs (bp). The size range is defined by the positions of two distinct peaks: the first at 35 bp and the second at 10,380 bp.

DNA fragments were detected from stage L6 onwards (Fig. 5). A lower level of DNA fragmentation was recorded in leather from L6 onwards treated with Lutan (Fig. 3) and Novaltan (Fig. 4).

For samples L1 to L5, there are fragments larger than this method's lower and upper range (35 bp to 10,380 bp) (Fig. 2). However, the concentration of fragments beyond the detection range cannot be determined. In sample L1, the largest are fragments ranging from 15,000 bp to 9,000 bp. For samples L2 to L5, the number of large fragments decreases, although they are still present, with the distribution of all the recorded fragments being roughly comparable (Fig. 2).

For the samples L6 to L9, it was not possible to determine the distribution of individual fragments (Figs 3–5). Sample L6 contained fragments ranging in size from

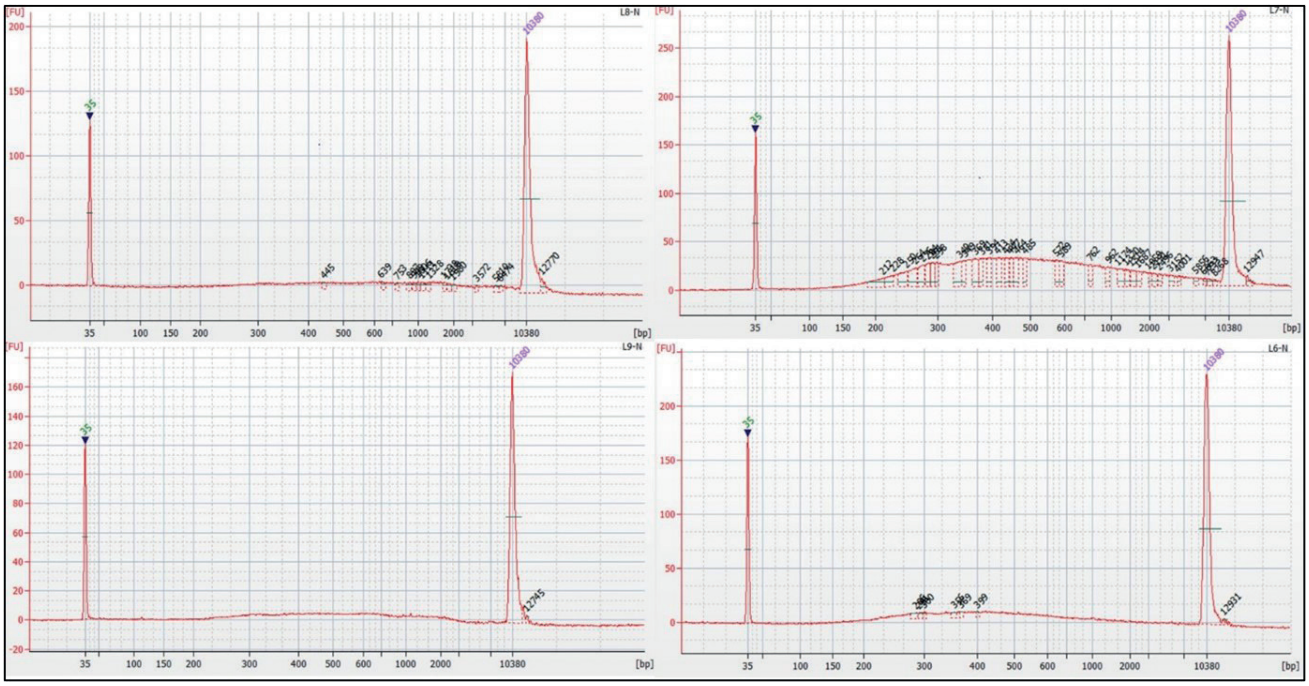

Fig. 4 Electropherograms recorded for the Novaltan AL-tanned samples, L6 to L9, respectively, quantified using the Agilent Bioanalyzer 2100. The values on the y-axis are units of fluorescence (FU) and the x-axis fragment lengths in base pairs (bp). The size range is defined by two distinct peaks: the first is for 35 bp and the second for 10,380 bp.

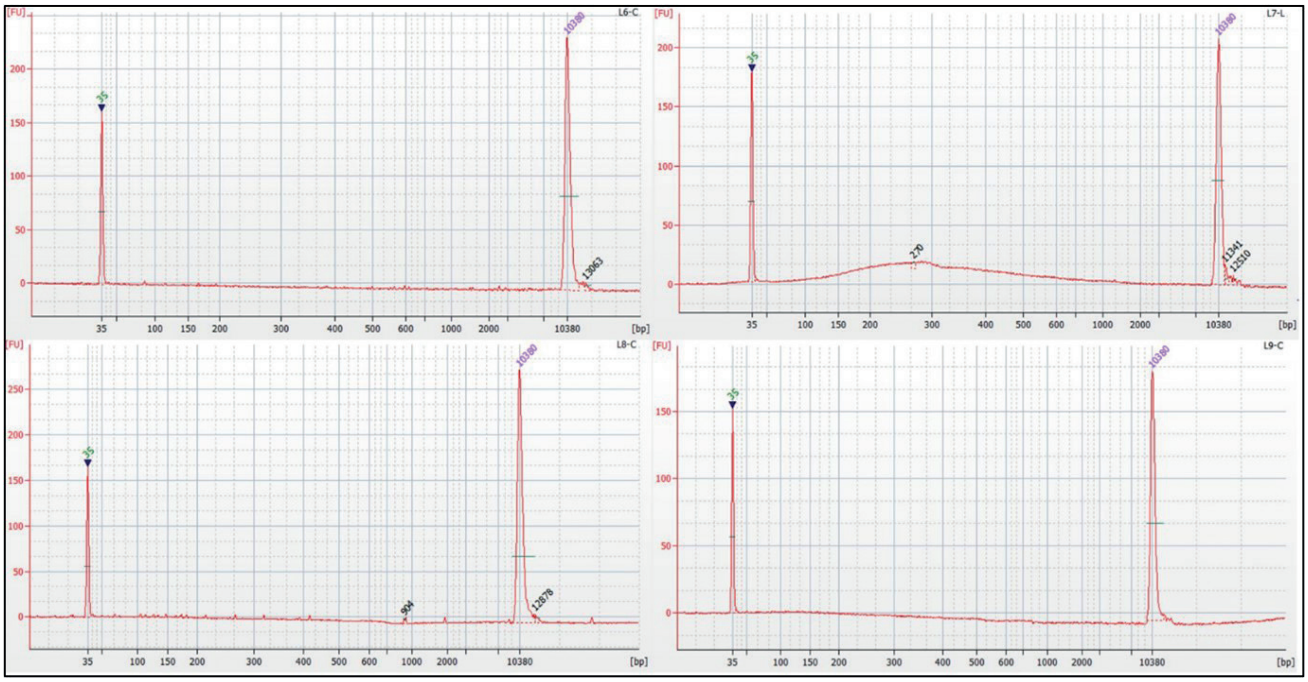

Fig. 5 Electropherograms recorded for the chromium sulphate-tanned samples, L6 to L9, respectively, quantified using the Agilent Bioanalyzer 2100. The values on the y-axis are units of fluorescence (FU) and x-axis fragment lengths in base pairs (bp). The size range is defined by the positions of the two distinct peaks: the first is for 35 bp and the second 10,380 bp.

approximately 200 bp to 500 bp (Fig. 3). Sample L6-N contained fragments ranging in size from 300 bp to 400 bp (Fig. 4). The presence of larger fragments of approximately 445 to 7,000 bp, was unexpectedly recorded in sample L8-N (Fig. 4), but is consistent with the DNA quantification reported using other methods (Hebenstreitova et al. 2024).

Case study #2

For this study, three electropherograms were recorded and are similar to those reported by Saskova et al. 2017 (Fig. 6). In the sample containing the DNA of *Bos taurus* (Fig. 5B), a distinct peak at approximately 525 bp was recorded, indicating the presence of animal DNA in that sample. In the sample containing *Hibiscus* sp. DNA

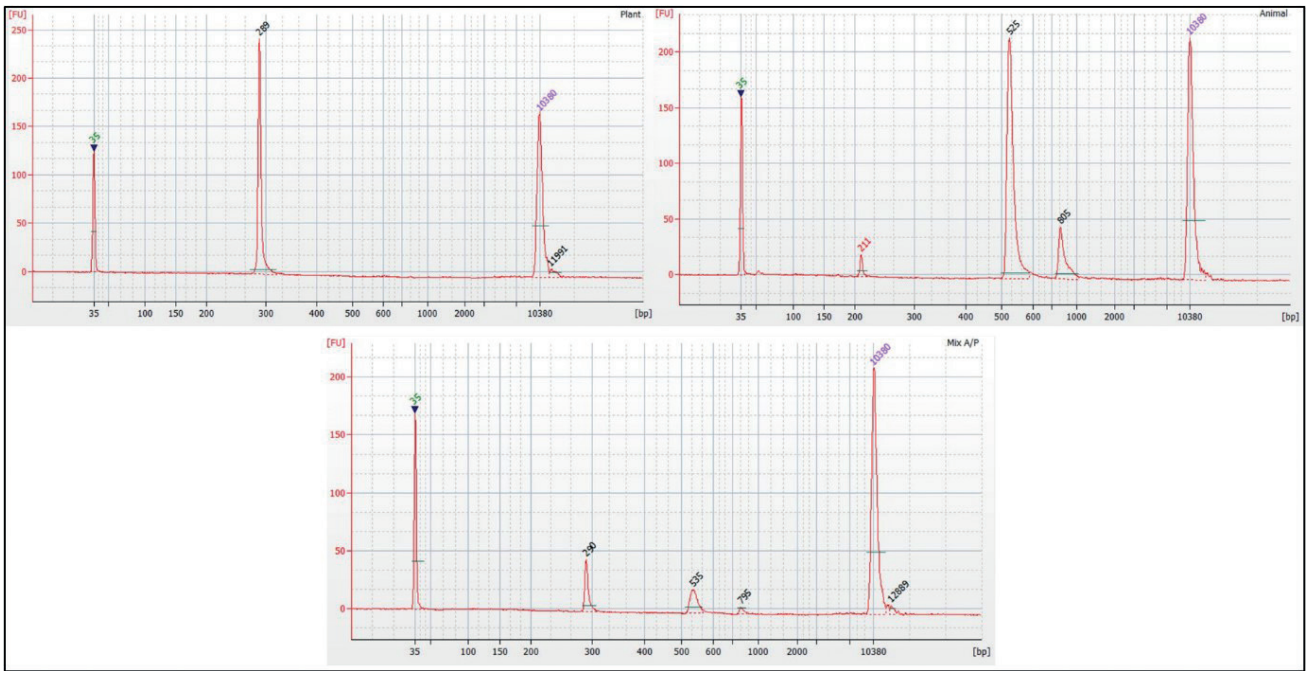

Fig. 6 Electropherograms recorded for the Triplex assay samples visualized using the Agilent Bioanalyzer 2100. (A) The sample containing *Hibiscus* sp. DNA is indicated by the peak at 289 bp. (B) Sample containing *Bos taurus* DNA is indicated by the peak at 525 bp. (C) Sample containing a mixture of plant and animal DNA (*Hibiscus* sp. and *Bos taurus*) is indicated by the peaks at 290 bp and 535 bp. The values on the y-axis are units of fluorescence (FU) and the x-axis fragment length in base pairs (bp). The size range is defined by two distinct peaks: the first at 35 bp and the second at 10,380 bp.

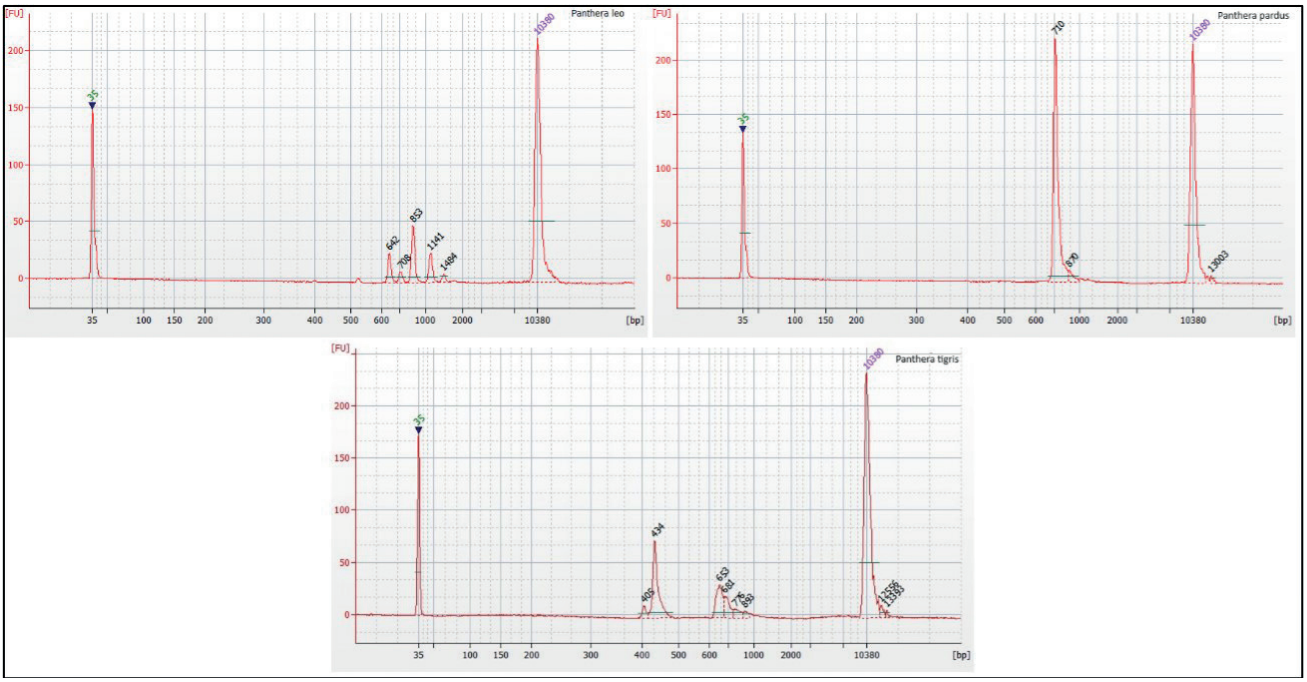

Fig. 7 Electropherograms recorded for the CR-mtDNA assay samples from *P. leo*, *P. pardus*, and *P. tigris*, respectively, visualized using the Agilent Bioanalyzer 2100. The values on the y-axis are units of fluorescence (FU) and the x-axis fragment lengths in base pairs (bp). The size range is defined by the positions of two distinct peaks: the first at 35 bp and second at 10,380 bp.

(Fig. 5A), there was a distinct peak at approximately 289 bp, indicating the presence of plant DNA. In the sample containing a mixture of animal and plant DNA (Fig 5C), two peaks were recorded at 535 bp and 290 bp, respectively, indicating the presence of animal and plant DNA. The amplification of the internal positive control (IPC) is marked by the peak at approximately 805 bp and 795 bp.

Case study #3

For this study 7 electropherogram plots were obtained (Fig. 7 and Fig. 8), which indicate that the length of the amplified control region of mtDNA in in different animals (*P. leo*, *P. tigris*, *P. pardus*, *B. taurus*, *S. scrofa domesticus*, *O. cuniculus* and *G. gallus*) is variable.

Discussion

The Agilent Bioanalyzer 2100 is a very useful tool for molecular biology and genetics, with advantages over traditional methods for determining the size and quantity of DNA, such as, agarose gel electrophoresis, spectrophotometry and fluorometry. Unlike agarose gel electrophoresis, which has limited resolution and requires larger sample volumes, the Bioanalyzer provides high-resolution separation of DNA fragments with increased sensitivity (Vitale 2000; Lu et al. 2002). Compared with PAGE, the Bioanalyzer eliminates the need for labour-intensive gel casting and staining (Agilent Technologies 2009). The Bioanalyzer's quantitative range (5–500 pg of DNA) enables the detection and separation of the minute amounts of DNA a characteristic of forensic samples, which make it highly sensitive.

The Bioanalyzer's microfluidic chip-based technology minimizes the size of the samples needed and in so doing preserves the valuable evidence. Furthermore, its automated nature reduces analysis-to-analysis variability and minimizes the risk of contamination, ensuring high assay reproducibility and repeatability.

In this study, the suitability of the Bioanalyzer for wildlife forensic genetics was explored. The results indicate that while the Bioanalyzer may not be particularly suitable for quantifying nonamplified DNA, it can be used for assessing the quality of DNA extracts. Another method of assessing DNA quality is to determine the degradation index using qPCR (Vernarecci et al. 2015) or a visual assessment using gel electrophoresis (Bhoyar et al. 2024). The main limitations of using qPCR to determine degradation is the need for the optimization of reaction conditions, the presence of PCR inhibitors and tendency to overstate the concentration of short DNA fragments (Smith and Osborn 2009; Gill et al. 2022). Agarose gel electrophoresis can provide insight into the level of DNA degradation by comparing the pattern of fragment migration of degraded and non-degraded DNA, which results in a typical smear pattern (Mohamed et al. 2020; Bhoyar et al. 2024).

The Agilent Bioanalyzer 2100 is used in forensic, archaeological, and ancient DNA studies, particularly for quality control and analysis of DNA samples (Senst et al. 2024). In forensic studies, it is used for evaluating the quality of degraded postmortem DNA samples, assessing total DNA and adapter dimer concentrations essential for next-generation sequencing (NGS) library preparation and quantifying mitochondrial DNA in order to refine inputs for cycle sequencing (Lozano-Peral et al.

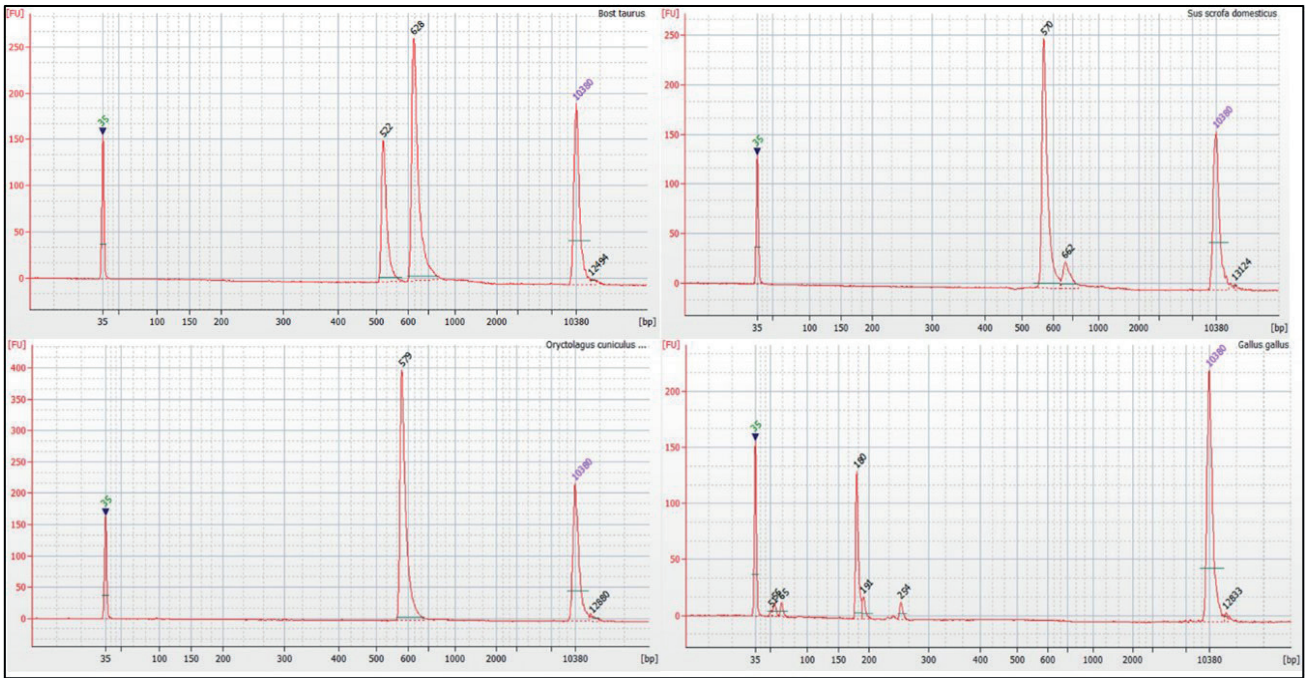

Fig. 8 Electropherograms recorded for the CR-mtDNA-assay samples from *B. taurus*, *S. scrofa domesticus*, *O. cuniculu*, and *G. gallus*, respectively, visualized using the Agilent Bioanalyzer 2100. The units on the y-axis are units of fluorescence (FU) and the x-axis fragment lengths in base pairs (bp). The size range is defined by two distinct peaks: the first at 35 bp and the second at 10,380 bp.

2021; Office of Chief Medical Examiner, n.d.; Senst et al. 2024). Archaeological and ancient DNA research has also benefited from its use, for instance, in the analysis DNA integrity under thermal stress and for improving extraction techniques for ancient samples under ultra-clean conditions (Matsvay et al. 2019). The examples demonstrate the instrument's versatility in ensuring analytical precision and advancing research in different scientific domains.

Using the "bioanalyzer" to evaluate the degradation of DNA extracts from tanned *Panthera pardus* hides at various stages of tanning proved useful for rapidly assessing the quality of the DNA extracted. This assessment is crucial, as it aids in determining whether a sample is of sufficient quality for costly and time-consuming methods such as DNA sequencing or typing, with a minimal use of the sample (1 µl/sample). The Bioanalyzer provided insights into the sizes and distribution of DNA fragments within an extract, and these results are consistent with previous findings, i.e., that electropherograms indicate that the leather-making process increases DNA fragmentation (Figs 2–5) (Hebenstreitova et al. 2024).

In addition to analysing nonamplified DNA, the Bioanalyzer can be utilized in assays involving PCR. The application of this approach for classifying unknown biological material via a Triplex assay and species identification via CR-mtDNA analysis was determined. The details of both these assays was previously published by Saskova et al. (2017). The resulting electropherograms were consistent with expectations based on previous findings, indicating that the Bioanalyzer can be integrated into PCR-based assays, however, neither classical agarose gel electrophoresis nor chip electrophoresis has the resolution of CE (Weiss et al. 1995; Gupta et al. 2010).

In species identification based on the analysis of the CR-mtDNA region, the results correspond with those previously published by Vankova and Vanek (2024), Saskova et al. (2017) and Pun et al. (2009) (Fig. 7 and Fig. 8), confirming the suitability of chip electrophoresis for species identification. The only variation from previously published results was recorded for the *Bos taurus* sample. According to Pun et al. (2009), there should be only one peak (537–544 bp); however, there are two distinct peaks. This could be attributed to nuclear-mitochondrial segments (NUMTs) (Zhang and Hewitt 1996; Song et al. 2008).

In addition to the aforementioned assays, the Agilent Bioanalyzer 2100 can theoretically be utilized in various assays, even beyond its intended scope of application. For example, it can be used in the analysis of polymorphic markers for identification purposes, such as variable number tandem repeats (VNTRs) or short tandem repeats (STRs) (Aboud et al. 2015); tissue or body fluid identification using mRNA analysis (Lin et al. 2015; Sauer et al. 2017); and field-based identification of illegal drugs (Lloyd et al. 2011). Another possible use is to include the Bioanalyzer in the species barcoding for the quality control of the mtDNA amplification prior to Sanger sequencing (Zakharov et al. 2011; Blekhman et al. 2020; Baur et al. 2022). The current exploratory application of the Agilent Bioanalyzer 2100 demonstrated that although it is unlikely to replace the established methods, this instrument can contribute to forensic investigations and research in specific cases. However, if the instrument is to be deployed in forensic analysis, further testing and validation for forensic use is required. These findings are consistent with those reported by other researchers (Gorzkiewicz et al. 2010).

Conclusion

In conclusion, this method can be used for carrying out various assays in wildlife forensic investigations or research. While it is not particularly suitable for the quantification of DNA in extracts from tanned skins, as the results for stage 6 and onwards in the tanning process are only of limited value, it can be particularly useful in the quick assessment of the quality of DNA extract before costly and time-consuming methods such as DNA sequencing or DNA typing. However, this method is suitable for rapid sample classification and identification of species.

Funding: This research was funded by the project "An effective use of forensic methods in wildlife crime investigation" (Ministry of Interior, Czech Republic, VJ01010026).

Data availability statement: Data supporting this study's findings are deposited on Zenodo.org with the accession link: https://doi.org/10.5281/zenodo.13777822.

REFERENCES

Aboud MJ, Gassmann M, Mccord BR (2015) Ultrafast STR Separations on Short-Channel microfluidic systems for forensic screening and genotyping. J Forensic Sci 60: 1164–1170. doi: 10.1111/1556-4029.12723.

Agilent Bioanalyzer System (2018) Applications for DNA, RNA, and Protein Analysis, pp 1–67.

Agilent Technologies (2009) Applications for DNA, RNA, Protein and Cell Analysis: Agilent 2100 Bioanalyzer System Application Compendium.

Baur B, Müller P, Steinmann P, Landert P, Gilgado JD, Rusterholz HP (2022) Invading non-native populations replace native ones of the endangered freshwater snail *Theodoxus fluviatilis* in the river Rhine. Eur J Environ Sci 12: 5–15. doi: 10.14712/23361964.2022.1.

Bhoyar L, Mehar P, Chavali K (2024) An overview of DNA degradation and its implications in forensic caseworks. Egypt J Forensic Sci. doi: 10.1186/s41935-024-00389-y.

Blekhman A, Goryacheva I, Schepetov D, Zakharov I (2020) Variability of the mitochondrial CO1 gene in native and invasive populations of *Harmonia axyridis* Pall. comparative analysis. PLoS One 15. doi: 10.1371/journal.pone.0231009.

Bruijns B, van Asten A, Tiggelaar R, Gardeniers H (2016) Microfluidic devices for forensic DNA analysis: A review. Biosensors (Basel). doi: 10.3390/bios6030041.

Gill P, Bleka Ø, Fonneløp AE (2022) Limitations of qPCR to estimate DNA quantity: An RFU method to facilitate inter-laboratory comparisons for activity level, and general applicability. Forensic Sci Int Genet 61: 102777. doi: 10.1016/j.fsigen.2022.102777.

Gorzkiewicz M, Duleba A, Rychlicka E, Wozniak M, Grzybowski T, Sliwka K (2010) Evaluation of the agilent 2100 bioanalyzer as a tool for DNA analysis in forensic genetics. Probl. Forensic Sci LXXXI.

Gupta V, Dorsey G, Hubbard AE, Rosenthal PJ, Greenhouse B (2010) Gel versus capillary electrophoresis genotyping for categorizing treatment outcomes in two anti-malarial trials in Uganda. Malar J 9. doi: 10.1186/1475-2875-9-19.

Hebenstreitova K, Salaba O, Trubac J, Kufnerova J, Vanek D (2024) The influence of tanning chemical agents on DNA degradation: a robust procedure for the analysis of tanned animal hide – A pilot study. Life (Basel) 14: 147. doi: 10.3390/life14010147.

Hedmark E, Ellegren H (2005) Microsatellite genotyping of DNA isolated from claws left on tanned carnivore hides. Int J Legal Med 119: 370–373. doi: 10.1007/s00414-005-0521-4.

Henger CS, Straughan DJ, Xu CCY, Nightingale BR, Kretser HE, Burnham-Curtis MK, McAloose D, Seimon TA (2023) A new multiplex qPCR assay to detect and differentiate big cat species in the illegal wildlife trade. Sci Rep 13. doi: 10.1038/S41598-023-36776-Z.

Khan FM, William K, Aruge S, Janjua S, Shah SA (2018) Illegal product manufacturing and exportation from Pakistan: Revealing the factuality of highly processed wildlife skin samples via DNA mini-barcoding. Nucleos Nucleot Nucl 37: 179–185. doi: 10.1080/15257770.2018.1450507.

Khedkar G, Khedkar C, Prakash B, Khedkar A, Haymer D (2019) DNA barcode based identification of a suspected tiger skin: A case to resolve mimicry. Forensic Sci Int Rep 1: 100027. doi: 10.1016/j.fsir.2019.100027.

Kumar N, Yadav VK, Rana AK (2017) Wildlife Forensic: current techniques and their limitations. J Forensic Sci Criminol 5. doi: 10.15744/2348-9804.5.402.

Lin MH, Jones DF, Fleming R (2015) Transcriptomic analysis of degraded forensic body fluids. Forensic Sci Int Genet 17: 35–42. doi: 10.1016/j.fsigen.2015.03.005.

Lloyd A, Blanes L, Beavis A, Roux C, Doble P (2011) A rapid method for the in-field analysis of amphetamines employing the agilent bioanalyzer. Anal Methods 3: 1535–1539. doi: 10.1039/c1ay05078h.

Lozano-Peral D, Rubio L, Santos I, Gaitán MJ, Viguera E, Martín-de-las-Heras S (2021) DNA degradation in human teeth exposed to thermal stress. Sci Rep 11: 12118. doi: 10.1038/s41598-021-91505-8.

Lu C-Y, Tso D-J, Yang T, Jong Y-J, Wei Y-H (2002) Detection of DNA mutations associated with mitochondrial diseases by Agilent 2100 bioanalyzer. Clin Chim Acta.

Mapes AA, Kloosterman AD, de Poot CJ (2015) DNA in the Criminal Justice System: The DNA success story in perspective. J Forensic Sci 60: 851–856. doi: 10.1111/1556-4029.12779.

Matsvay AD, Alborova IE, Pimkina EV, Markelov ML, Khafizov K, Mustafin KK (2019) Experimental approaches for ancient DNA extraction and sample preparation for next generation sequencing in ultra-clean conditions. Conserv Genet Resour 11: 345–353. doi: 10.1007/s12686-018-1016-1.

Mohamed M, El Sherbeny M, Farag D (2020) A comparative study of two gel-based techniques to detect the relationship between post-mortem interval and nuclear DNA degradation in different tissues in albino rats. Egypt Dent J 66: 175–186. doi: 10.21608/edj.2020.77533.

Office of Chief Medical Examiner, n.d. Protocols for forensic mitochondrial DNA analysis. New York City: Office of Chief Medical Examiner.

Pachnerová Brabcová K, Pravdíková N, Čápová K, Frouzová J, Hebenstreitová K, Jandová K, Kukla J, Rajmonová E, Salaba O, Světlík I, Šmok D, Trubač J, Kufnerová J (2024) Effect of leather tanning process on stable isotopes and radiocarbon in tissues of Persian leopard: preliminary results. Forensic Sci Int Rep 10: 100398. doi: 10.1016/j.fsir.2024.100398.

Panaro NJ, Yuen PK, Sakazume T, Fortina P, Kricka LJ, Wilding P (2000) Evaluation of DNA fragment sizing and quantification by the Agilent 2100 Bioanalyzer. Clin Chem 46.

Prakash Goyal S (2016) Genetic based species identification and tracking of the geographic origin of a fully tanned animal skin in wildlife forensics. Foresic Res Criminol Int J 2: 128–134. doi: 10.15406/frcij.2016.02.00058.

Pun KM, Albrecht C, Castella V, Fumagalli L (2009) Species identification in mammals from mixed biological samples based on mitochondrial DNA control region length polymorphism. Electrophoresis 30: 1008–1014. doi: 10.1002/ELPS.200800365.

Rajani CV, Patki HS, Simanta P, Surjith K, Deepa PM, Pradeep M (2020) Histomorphological differentiation of the skin of leopard (*Panthera pardus*), leopard cat (*Prionailurus bengalensis*), Bengal tiger (*Panthera tigris*), and golden jackal (*Canis aureus*). Vet World 13: 827–832. doi: 10.14202/vetworld.2020.827-832.

Saskova L, Votrubova J, Vanek D (2017) Rapid classification of unknown biological material using a novel triplex assay. Forensic Sci Int Genet Suppl Ser 6: e132–e134. doi: 10.1016/j.fsigss.2017.09.030.

Sauer E, Extra A, Cachée P, Courts C (2017) Identification of organ tissue types and skin from forensic samples by microRNA expression analysis. Forensic Sci Int Genet 28: 99–110. doi: 10.1016/j.fsigen.2017.02.002.

Senst A, Bonsiepe H, Kron S, Schulz I (2024) Application of the Agilent 2100 Bioanalyzer instrument as quality control for next-generation sequencing. J Forensic Sci 69: 2192–2196. doi: 10.1111/1556-4029.15601.

Smith CJ, Osborn AM (2009) Advantages and limitations of quantitative PCR (Q-PCR)-based approaches in microbial ecology. FEMS Microbiol Ecol 67: 6–20. doi: 10.1111/j.1574-6941.2008.00629.x

Song H, Buhay JE, Whiting MF, Crandall KA (2008) Many species in one: DNA barcoding overestimates the number of species when nuclear mitochondrial pseudogenes are coamplified. Proc Natl Acad Sci USA 105: 13486–13491. doi: 10.1073/pnas.0803076105.

Vankova L, Vanek D (2022) DNA-based identification of big cats and traditional Chinese medicine artifacts in the Czech Republic. Forensic Sci Int Genet Suppl Ser 8: 122–124. doi: 10.1016/j.fsigss.2022.10.005.

Vankova L, Vanek D (2024) Capillary-Electrophoresis-Based species barcoding of big cats: CR-mtDNA-Length Polymorphism. Life (Basel) 14: 497. doi: 10.3390/life14040497.

Vernarecci S, Ottaviani E, Agostino A, Mei E, Calandro L, Montagna P (2015) Quantifiler® Trio Kit and forensic samples management: A matter of degradation. Forensic Sci Int Genet 16: 77–85. doi: 10.1016/j.fsigen.2014.12.005.

Vitale D (2000) Comparing the Agilent 2100 Bioanalyzer performance to traditional DNA analysis techniques Application Note.

Vuissoz A, Worobey M, Odegaard N, Bunce M, Machado CA, Lynnerup N, Peacock EE, Gilbert MTP (2007) The survival of PCR-amplifiable DNA in cow leather. J Archaeol Sci 34: 823–829. doi: 10.1016/j.jas.2006.09.002.

Webster LMI, Prigge T-L, Frankham GJ (2023) A guide for the validation of DNA based species identification in forensic casework. doi: 10.1016/j.fsiae.2023.100080.

Weiss GH, Garner M, Yarmola E, Boček P, Chrambach A (1995) A comparison of resolution of DNA fragments between agarose gel and capillary zone electrophoresis in agarose solutions. Electrophoresis 16: 1345–1353. doi: 10.1002/elps.11501601222.

Zakharov IA, Goryacheva II, Suvorov A (2011) Mitochondrial DNA polymorphism in invasive and native populations of *Harmonia axyridis*. Eur J Environ Sci 1: 15–18. doi: 10.14712/23361964.2015.59.

Zhang D-X, Hewitt GM (1996) Nuclear integrations: challenges for mitochondrial DNA markers. Trends Ecol Evol 11: 247–251. doi: 10.1016/0169-5347(96)10031-8.

Zou Z-T, Uphyrkina OV, Fomenko P, Luo S-J (2015) The development and application of a multiplex short tandem repeat (STR) system for identifying subspecies, individuals and sex in tigers. Integr Zool 10: 376–388. doi: 10.1111/1749-4877.12136.